T2R2 東京科学大学 リサーチリポジトリ
Science Tokyo Research Repository

# 論文 / 著書情報
# Article / Book Information

| | |
|---|---|
| 題目(和文) | 将来の三次元積層型電界効果トランジスタに向けた低基板温度及び低粒子フラックススパッタリングによるMoS2膜質向上 |
| Title(English) | Improvement of MoS2 Film Quality using Low-Particle-Flux Sputtering at Low-Substrate Temperature for Future 3D-Stacked Field-Effect Transistors |
| 著者(和文) | 今井慎也 |
| Author(English) | Shinya Imai |
| 出典(和文) | 学位:博士(工学),<br>学位授与機関:東京科学大学,<br>報告番号:甲第274号,<br>授与年月日:2025年3月26日,<br>学位の種別:課程博士,<br>審査員:若林 整,宮本 恭幸,渡辺 正裕,大見 俊一郎,角嶋 邦之,近藤 博基 |
| Citation(English) | Degree:Doctor (Engineering),<br>Conferring organization: Institute of Science Tokyo,<br>Report number:甲第274号,<br>Conferred date:2025/3/26,<br>Degree Type:Course doctor,<br>Examiner:,,,,, |
| 学位種別(和文) | 博士論文 |
| Type(English) | Doctoral Thesis |

Powered by T2R2 (Science Tokyo Research Repository)

# Improvement of $MoS_2$ Film Quality using Low-Particle-Flux Sputtering at Low-Substrate Temperature for Future 3D-Stacked Field-Effect Transistors

by

**Shinya Imai**

Bachelor of Electrical and Electronics Engineering at
Tokyo Institute of Technology, March 2020

Master of Electrical and Electronics Engineering at
Tokyo Institute of Technology, March 2022

Submitted to the
Department of Electrical and Electronics Engineering,
School of Engineering
for the degree of

Doctor of Philosophy
in Engineering

at the
February, 26th, 2025

@2025 Institute of Science Tokyo
All rights reserved.

Abstract of Doctoral Thesis, February 26th, 2025

# Improvement of $MoS_2$ Film Quality using Low-Particle-Flux Sputtering at Low-Substrate Temperature for Future 3D-Stacked Field-Effect Transistors

Supervisor: Hitoshi Wakabayashi
Department of Electrical and Electronics Engineering
School of Engineering
Shinya Imai

This thesis extensively investigates the improvement of molybdenum disulfide ($MoS_2$) film quality at low temperatures for future three-dimensional stacked field-effect transistors. $MoS_2$ films are known to exhibit high electron mobility even in an atomic layer thickness, making them a promising alternative to silicon channels in next-generation 3D-stacked FETs. Conventional methods for forming $MoS_2$ films include exfoliation and chemical vapor deposition (CVD) conducted at high temperatures of 800°C or more. While these methods are effective for obtaining high-quality films, they are limited by their inability to effectively reduce defect densities and their incompatibility with the strict thermal budget requirements for stacked transistors. To overcome these challenges, the author adopted sputtering, a deposition method that can produce large-area, uniform films at significantly lower temperatures below 500°C. However, sputtered $MoS_2$ films exhibit problems such as small grain sizes and high sulfur defect densities, limiting their potential for practical applications. To address these issues, sulfur-vapor annealing (S-annealing) at 700°C has been proposed in previous studies to compensate for sulfur vacancies and improve film quality. This study seeks to deepen the understanding of the effects of S-annealing on $MoS_2$ films by sputtering, identify strategies to improve film quality even before S-annealing and explore the feasibility of producing high-quality films at even lower temperatures.

The author set three critical target parameters for $MoS_2$ film quality. First, the film formation temperature was set to 700°C or less for front-end-of-line (FEOL) processes and 400°C or less for back-end-of-line (BEOL) processes to meet industrial requirements. Second, the crystal size was set to 7.9 nm or more for the channel dimensions of future semiconductor devices. Third, the target mobility is set at 185 $cm^2/Vs$ with a corresponding sulfur defect density ($V_s$) below 0.14%. These parameters serve as a guideline for balancing material performance with manufacturing feasibility. The crystal growth mechanism during sputtering is analyzed, which examines how the surface migration length of sputtered particles contributes to the grain size increase. Three key factors that enlarge this surface migration length of particles were identified: increasing the substrate temperature ($T_{sub.}$), increasing the flux temperature ($T_{flux}$), and reducing the particle flux to the substrate. Additionally, simulations of the behavior of sputtered particles traveling from the

target to the substrate revealed that high RF power, a short target-to-substrate distance, and low Ar pressure are practical approaches to increase the sulfur flux to the substrate, thereby reducing the sulfur defect density. These suggest that process parameters must be carefully tuned to optimize the deposition conditions for high-quality films.

First, it was observed that enlarging $T_{\mathrm{sub.}}$ enhances the surface migration of sputtered particles, leading to larger grains. However, excessively high $T_{\mathrm{sub.}}$ caused an increase in sulfur defect density, likely due to sulfur evaporation under prolonged exposure to elevated temperatures. S-annealing effectively compensated for these deficiencies, restoring film quality and reducing defect densities. The optimal substrate temperature was identified as 300°C, where films showed the lowest sulfur defect density after annealing. This temperature represents an ideal trade-off between enabling sufficient surface migration and avoiding excessive sulfur loss during deposition.

Next, to further improve crystal size, the author investigated the effects of RF power modulation, which controls both $T_{\mathrm{flux}}$ and particle flux. Intermediate RF power provided the best balance, producing films with sufficient $T_{\mathrm{flux}}$ and low particle flux, which promoted more significant grain formation.

Additionally, a grid was introduced into the sputtering system to reduce particle flux further while maintaining adequate flux energy. This approach significantly improved the crystal size with a lower deposition rate, and the nucleation density decreases with a low particle flux. Finally, the performance of the sputtering method was benchmarked against other deposition techniques. It was demonstrated that sputtering achieves superior results in terms of crystallite size with low-temperature deposition. Crystal size reached a maximum size of 26 nm and an average size of 9.1 nm, exceeding the target of 7.9 nm. Films deposited at 300°C met the thermal budget requirements for FEOL and BEOL processes while showing significant improvements in grain size. However, the standard deviation was 7.9 nm, suggesting the need for selective removal of the microcrystalline regions of the second layer and deposition with even lower particle flux. Furthermore, the sulfur defect density remained at 1.65%, which calculated the mobility of $\sim$26.5 $\mathrm{cm^2/Vs}$, indicating that further optimization is required to achieve the target mobility. Additional studies on sulfur flux supply during sputtering are recommended to bridge this gap and further enhance material performance.

In conclusion, this thesis comprehensively analyzes the factors influencing the quality of sputtered $MoS_2$ films. The results demonstrate that optimizing particle temperature on the substrate surface and reducing particle flux during sputtering significantly enhances crystal size, while additional sulfur supply can effectively mitigate sulfur defects. These findings contribute to developing high-quality $MoS_2$ films suitable for next-generation logic semiconductors and offer valuable insights for industrial applications. This work establishes a foundation for further exploration of sputtering techniques and their potential integration into advanced semiconductor manufacturing processes.

# Acknowledgements

My research at the Tokyo Institute of Technology (Institute of Science Tokyo) has been supported by many individuals for whom I am deeply grateful. I want to express my sincerest appreciation to Professor Hitoshi Wakabayashi for his invaluable support and guidance throughout my doctoral studies. I am also profoundly thankful to Professor Hiroki Kondo from Kyushu University, Professor Yasuyuki Miyamoto, Associate Professor Masahiro Watanabe, Associate Professor Shunichiro Ohmi, and Associate Professor Kuniyuki Kakushima from the Institute of Science Tokyo. Thank you for serving as the examiner of my doctoral thesis and for your insightful feedback. Furthermore, I extend my heartfelt gratitude to Assistant Professor Takamasa Kawanago, Assistant Professor Iriya Muneta, Assistant Professor Takuya Hoshi, Specially Appointed Professor Shigetaka Tomiya, Specially Appointed Professor Tetsuya Tatsumi, Associate Professor Kuniyuki Kakushima, and Professor Kazuo Tsutsui, Dr. Atsushi Hori for their invaluable guidance on the fundamental aspects of my research. Additionally, I wish to express my deep appreciation to Dr. Masaya Hamada, Dr. Takuya Hamada, Dr. Takanori Shirokura, Mr. Taiga Horiguchi, Mr. Tomomu Yamazaki, Mr. Ryo Ono, Mr. Shinichi Tatematsu, and Mr. Ryosuke Kajikawa, who were formerly members of the Wakabayashi Laboratory for their generous support and cooperation. I am equally grateful to all the current members of the Wakabayashi Laboratory, especially Mr. Wang Peilong, Ms. Lu Yaobin, Mr. Naoki Matsunaga, Mr. Keita Kurohara, Mr. Shungo Okamura, Mr. Wang Zhenhao, Mr. Kaede Teraoka, Mr. Soma Ito, Mr. Jang Jaehyo, Mr. Wang Ruihan, Mr. Shunsuke Nozawa, and Mr. Taiga Fuse, whose collaboration and encouragement were instrumental in completing this research. In addition, I would like to thank Mr. Tenko Yamashita for hosting me for the summer internship at IBM Research in New York State, United States, from May 20th to August 9th, 2024.

This work was partly supported by the Open Facility Center at the Institute of Science Tokyo, the Collaborative Research Chair/Division Program funded by Sony Group Corp., the MEXT Initiative to Establish Next-generation Novel Integrated Circuits Centers (XNICS) (Grant Number JPJ011438), and JSPS KAKENHI (Grant Numbers 20H05880 and 22K04181). Measurements of ion energy distribution were conducted using the Semion Retarding Field Energy Analyzer (RFEA) system from Impedans Ltd., with the support of MATSUBO Corporation. Finally, I extend my deepest gratitude to everyone who has contributed to my research journey.

Thank you.

# Contents

**Acknowledgements** **i**

**List of Figures** **v**

**List of Tables** **xiii**

**Chapter 1 Research background and motivation** **1**

1.1 Logic transistor scaling and next-generation transistors . . . . . . . . . . 1
1.2 Requirements for next-generation semiconductor channel materials . . . 5
1.3 Transition metal di-chalcogenide (TMDC) and molybdenum disulfide ($MoS_2$) 8
1.4 $MoS_2$ film formation methods . . . . . . . . . . . . . . . . . . . . . . . 10
1.5 Purpose of this study . . . . . . . . . . . . . . . . . . . . . . . . . . . . 13
1.6 Structure of doctoral thesis . . . . . . . . . . . . . . . . . . . . . . . . 14

**Chapter 2 Target values for improvement of $MoS_2$ film quality** **15**

2.1 Thermal budget requirement for $MoS_2$ film . . . . . . . . . . . . . . . . 15
2.2 Crystal size requirement . . . . . . . . . . . . . . . . . . . . . . . . . . 20
2.3 Requirement of mobility in the single crystal $MoS_2$ channel . . . . . . . 23
2.4 Summary . . . . . . . . . . . . . . . . . . . . . . . . . . . . . . . . . . 27

**Chapter 3 Approach of $MoS_2$ sputtering with large crystal size and low sulfur defect density** **28**

3.1 Mechanism of crystal growth on the substrate surface during sputtering 29
3.2 Discussion on the particle reaching the substrate surface for low sulfur vacancy density in $MoS_2$ film . . . . . . . . . . . . . . . . . . . . . . . . 32
3.2.1 Particle Species Reaching the Substrate in $MoS_2$ Sputtering . . . 32
3.2.2 Thermalization of sputtered particles and investigation of particle behavior . . . . . . . . . . . . . . . . . . . . . . . . . . . . . . . 33
3.2.3 Step 1: Sputtering . . . . . . . . . . . . . . . . . . . . . . . . . 35
3.2.4 Step 2: Transport . . . . . . . . . . . . . . . . . . . . . . . . . . 37
3.2.5 Consideration of the sticking coefficient on the number of particles on the substrate surface . . . . . . . . . . . . . . . . . . . . . . . 39
3.3 Summary . . . . . . . . . . . . . . . . . . . . . . . . . . . . . . . . . . 41

**Chapter 4 Dependence of $MoS_2$ film quality varying substrate temper-**

**ature during sputtering** **42**
4.1 Background . . . . . . . . . . . . . . . . . . . . . . . . . . . . . . . . 42
4.2 Experimental methods . . . . . . . . . . . . . . . . . . . . . . . . . . . 45
4.3 Results and discussion . . . . . . . . . . . . . . . . . . . . . . . . . . 46
4.3.1 Comparing the $MoS_2$ film quality after sputtering and S-annealing 46
4.3.2 Discussion of S-annealing effect for $MoS_2$ film deposited by sputtering . . . . . . . . . . . . . . . . . . . . . . . . . . . . . . . . 52
4.3.3 $MoS_2$ film quality after sputtering and S-annealing depending on substrate temperature ($T_{sub.}$) . . . . . . . . . . . . . . . . . . . . 54
4.3.4 Study on the S-annealing effect of $MoS_2$ films at different substrate temperatures during sputtering ($T_{sub.}$) . . . . . . . . . . . . . . 60
4.4 Summary . . . . . . . . . . . . . . . . . . . . . . . . . . . . . . . . . 61

**Chapter 5 Crystal size enlargement of $MoS_2$ film with control of flux temperature and particle flux during sputtering** **63**
5.1 Background . . . . . . . . . . . . . . . . . . . . . . . . . . . . . . . . 63
5.2 Experimental methods . . . . . . . . . . . . . . . . . . . . . . . . . . . 63
5.2.1 $MoS_2$ film formation by sputtering and S-annealing . . . . . . . . 63
5.2.2 Ion energy distribution during sputtering . . . . . . . . . . . . . 65
5.3 Results and discussion . . . . . . . . . . . . . . . . . . . . . . . . . . 66
5.3.1 $MoS_2$ film formation by sputtering and sulfur-vapor annealing . . 66
5.3.2 Ion energy distribution during sputtering . . . . . . . . . . . . . 73
5.3.3 Surface migration model during sputtering . . . . . . . . . . . . 75
5.4 Summary . . . . . . . . . . . . . . . . . . . . . . . . . . . . . . . . . 76

**Chapter 6 Crystal size enlargement of $MoS_2$ film by low-particle-flux sputtering** **77**
6.1 Background . . . . . . . . . . . . . . . . . . . . . . . . . . . . . . . . 77
6.2 Experimental methods . . . . . . . . . . . . . . . . . . . . . . . . . . . 78
6.3 Results and discussion . . . . . . . . . . . . . . . . . . . . . . . . . . 81
6.4 Summary . . . . . . . . . . . . . . . . . . . . . . . . . . . . . . . . . 93

**Chapter 7 Conclusions** **94**
7.1 Conclusions of this thesis . . . . . . . . . . . . . . . . . . . . . . . . 94
7.2 Future directions . . . . . . . . . . . . . . . . . . . . . . . . . . . . . 98
7.2.1 Optimizing the sputtering Ar pressure . . . . . . . . . . . . . . . 98
7.2.2 Removal of small $MoS_2$ crystal using area selective etching . . . 100
7.2.3 Area selective deposition for single crystal $MoS_2$ . . . . . . . . . 100
7.2.4 Approach for further improvement of high-quality $MoS_2$ films . . 100

**Publications and presentations** **104**

**References** **107**

**Appendix A Benchmark of $MoS_2$ film properties in recent researches** **120**

**Appendix B Control of $MoS_2$ film quality by accelerating the ionized particles to the substrate using molybdenum-grid electrodes** **121**

B.1 Background . . . . . . . . . . . . . . . . . . . . . . . . . . . . . . . . 121

B.2 Experimental methods . . . . . . . . . . . . . . . . . . . . . . . . . . . 121

B.3 Results and discussion . . . . . . . . . . . . . . . . . . . . . . . . . . . 123

# List of Figures


1.1 (a) Image of data center and schematic of (b) Internet of Things (IoT) [1, 2]. . . . . . . . . . 2
1.2 Forecast of energy usage in information and communication technologies (ICT). By 2030, data centers are likely to constitute 8% of global electricity demand, and ICT could use 20% of it [3]. . . . . . . . . . 3
1.3 MOSFET device structure for electrical-field-scaling [4]. . . . . . . . . . 3
1.4 Transition and future forecast of Technology node, gate length, and metal pitch [5]. . . . . . . . . . 4
1.5 Trends of (a) speed ($CV/I$) and energy ($CV^2$), (d) on-current ($I_{\text{on}}$) and off-current ($I_{\text{off}}$), (c) supply voltage ($V_{\text{dd}}$) and equivalent capacitance thickness (CET), and (d) power density of high-performance (HP) transistors in the past and future. Technology node is also shown in (a) and (c). It is assumed that gate width $W = 10L_{\text{g}}$ in planar transistors, fin number reduced from 3 (2012) to 1 (2024), GAA stacked sheet number increased from 3 (2025) to 4 (2031), CFET was introduced in 2028, and stacked tier number increased from 2 (2031) to 6 (2037), and FO = 1. $I_{\text{on}}$ and $I_{\text{off}}$ are normalized to effective width ($W_{\text{eff}}$), while layout footprint is used to calculate power density [5]. . . . . . . . . . 5
1.6 Transistor scaling and next generation structures for high-performance logic transistor [6–10]. . . . . . . . . . 6
1.7 Relationship between power density and ON resistance for various device architectures [11]. . . . . . . . . . 7
1.8 Schematic diagram of transition metal dichalcogenide (TMDC). Black dots indicate transition metal elements, and yellow dots indicate chalcogen elements. Layers are bonding together by van der Waals forces [12]. . . . . 8
1.9 Benchmark of mobility on traditional and 2D semiconductors depending on channel thickness ($t_{\text{ch}}$) [13]. (b) Band edge positions and band gaps of various TMDC films [14]. . . . . . . . . . 9
1.10 (a) Mobility benchmark depending on $MoS_2$ and Silicon channel thickness. (b) Benchmark subthreshold swing depending on gate length ($L_{\text{g}}$) in $MoS_2$-FET compared from Si-FinFET [15]. . . . . . . . . . 10

1.11 (a) Schematic diagram of gate all around (GAA) nano-sheet (NS) field electric transistor (FET) using $MoS_2$ film [16]. (b) Schematic of p/n 3D-stacked FETs using $MoS_2$ film [17]. . . . . . . . . . . . . . . . . . . . . 10
1.12 Schematic illustrations of standard 2D film fabrication methods. (a) Micromechanical exfoliation of 2D material [18]. (b) CVD for $MoS_2$ film fabrication [17]. . . . . . . . . . . . . . . . . . . . . . . . . . . . . . . . . 11
1.13 (a) Schematic image of RF magnetron sputtering (b) TEM image of thin $MoS_2$ film formed by RF magnetron sputtering [19]. . . . . . . . . . . . 12
1.14 Schematic of sulfur vapor annealing (S-annealing) [20]. . . . . . . . . . 12
1.15 (a) Hall-effect measurement results of carrier density and electron mobility for approximately 4-nm-thick $MoS_2$ film as function of temperature [20] and (b) $I_d$-$V_{gs}$ characteristics of metal isolation semiconductor FET (MISFET) with $MoS_2$ film formed by sputtering and S-annealing [21]. . . . . . . . 13
1.16 Structure of this thesis. . . . . . . . . . . . . . . . . . . . . . . . . . 14

2.1 Process flow of $MoS_2$-nanosheet (NS) field electric transistor (FET) [16]. 16
2.2 (a) Cross-sectional transmission electron microscope (TEM) images of stacked $MoS_2$/Sacrificial layer structure and (b) Schematic of $MoS_2$ NS-FET [16]. 17
2.3 Model of oxygen diffusion reaction in $MoS_2$ film on (a) $SiO_2$ and (b) $Si_3N_4$ substrate during high-temperature annealing with Ar gas [22]. . . . . . . 17
2.4 X-ray photoelectron spectroscopy (XPS) results of O 1$s$ orbits in $MoS_2$ film on (a) $SiO_2$ and (b) $Si_3N_4$ after Ar annealing at 700°C from Figure 2.3 [22]. 18
2.5 Process of $MoS_2$ film deposition and device fabrication during back end of line (BEOL) integration in Si-complementary metal-oxide-semiconductor (CMOS) circuits [23]. . . . . . . . . . . . . . . . . . . . . . . . . . . 18
2.6 Static random-access memory (SRAM) circuit utilizing Si transistors in front end of line (FEOL) and $MoS_2$ transistors in back end of line (BEOL) [23]. 19
2.7 Schematic of three-dimensional stacked integrated circuits (IC) using two-dimensional channel transistors [24]. . . . . . . . . . . . . . . . . . . . . 19
2.8 Schematics of future FET structure using $MoS_2$ film [25, 26]. $L_g$, $L_c$, and $L_{sp}$ are gate length, contact length, and spacer length between gate and source/drain electrodes, respectively. CGP is contacted gate pitch. . . 21
2.9 Prediction trends of gate length ($L_g$) and nanosheet (NS) width ($W$) from 2023 to 2034 [27]. . . . . . . . . . . . . . . . . . . . . . . . . . . . . 22
2.10 (a) Cross-sectional TEM image of Si-gate all around (GAA)-nanosheet(NS)-FET [28]. (b) Cross-sectional TEM image of Si channel region in (a). Si channel thickness ($T_{Si}$) is 3 nm. (c) Mobility of Si-GAA-NS-FET depending on carrier density ($N_s$). Gate length ($L_g$) is 18 nm, and silicon channel thickness ($T_{Si}$) is 6 nm [28]. (d) Dependence of normalized mobility of Si-GAA-NS-FET on $T_{Si}$ [28]. Mobility at 3 nm-$T_{Si}$ is 185 $cm^2$/Vs. . . . 24

2.11 (a) Schematic illustration of 1 monolayer (ML)-$MoS_2$ film with 3% sulfur defect density [29]. (b) Electron mobility dependence on sulfur defect density ($V_s$), calculated from (a) [29]. . . . . 25
2.12 (a) Dielectric constant and $A_{1g}$ Raman shift at 714 $cm^{-1}$ of $Li_2ZnTi_3O_8$(LZT)-xwt.%$Nb_2O_5$ (x = 0, 1, 2, 3, 4) ceramics sintered at 1075°C for 4 hours [30]. (b) Raman peak shift depending on amount of sulfur defects ($V_s$) [31]. (c) Influence of short channel effect (SCE) at high dielectric constant of $MoS_2$ film in gate length direction. At low dielectric constant, SCE can be suppressed. . . . . 26

3.1 Surface reaction model and mechanism of nucleation and crystal growth during physical vapor deposition on substrate. Layer-by-layer $MoS_2$ film formation is assumed to proceed through nucleation and crystal growth. 30
3.2 Approach for achieving long surface migration length of particles on substrate by controlling particle temperature ($T_{\text{particle}}$) and particle flux during sputtering deposition on substrate. . . . . 31
3.3 Schematic of particle species reaching substrate during $MoS_2$ sputtering, including gas scattering and thermalization of sputtered particles in sputtering system [32]. . . . . 32
3.4 Model diagram of thermalization distance of sputtered particles and number of particles reaching substrate. (a) Case where thermalization distance is shorter than target-to-substrate (T-S) distance. Sputtered particles are thermalized before reaching substrate, reducing number of particles reaching substrate. (b) Case where thermalization distance is longer than T-S distance. Particles are not thermalized and reach substrate with directionality toward substrate. . . . . 34
3.5 Principle of RF magnetron sputtering for $MoS_2$ film and potential distribution inside sputtering equipment. . . . . 35
3.6 (a) Energy distribution function of sputtered Mo atoms. (b) Average energy of sputtered atoms from target surface. Ar incident ion energy ($E^{+}_{Ar}$) is varied from 50 to 150 eV. . . . . 36
3.7 Nuclear-stopping and electronic-stopping power of sputtered atoms as function of energy calculated using SRIM. . . . . 38
3.8 Average transport distance of sputtered atoms as function of energy near target surface. . . . . 38
3.9 Average thermalization distance of sputtered particles as function of incident $Ar^{+}$ energy. Ar temperature was set to 300°C, and Ar pressure was set to (a) 0.5 Pa and (b) 0.4 Pa, respectively. . . . . 39

4.1 Approach to enhance surface migration length by high substrate temperature ($T_{\text{sub.}}$). . . . . 43

4.2 XPS peaks of bulk $MoS_2$ with ultra-high-vacuum annealing [33]. . . . . 43
4.3 Changes in substrate temperature over time during sputtering ($t_{\mathrm{sputter}}$) and natural cooling ($t_{\mathrm{cool}}$) of $MoS_2$ film. At high substrate temperatures during natural cooling ($t_{\mathrm{cool}}$), sulfur defects ($V_{\mathrm{s}}$) are more easily formed in $MoS_2$ film. . . . . 44
4.4 Schematic of (a) sputtering and (b) sulfur-vapor annealing (S-annealing) systems. . . . . 45
4.5 XPS spectra corresponding to (b) Mo $3d$ and (c) S $2p$ orbitals of $MoS_2$ films after sputtering and S-annealing. 2.5-nm $MoS_2$ films were deposited at 300°C using RF power of 40 W. Dotted and solid lines represent measured and fitted spectra, respectively. . . . . 46
4.6 Raman spectra of $MoS_2$ films after sputtering and S-annealing. 2.5-nm-$MoS_2$ films were deposited at 300°C using RF power of 40 W. . . . . 47
4.7 XRD patterns of as-sputtered and S-annealed $MoS_2$ films, which were sputtered at 40 W under Ar pressure of 0.55 Pa at 300°C. Signal intensities were normalized by intensity of silicon (004) peak. . . . . 48
4.8 (a) Structure of the $MoS_2$ sample for automated crystal orientation and phase mapping in transmission electron microscopy (ACOM-TEM). TD, RD, and ND correspond to transverse, rolling, and normal directions. (b) Pole figure maps for $MoS_2$ (100) and (110) planes. . . . . 49
4.9 Cross-sectional STEM images in (a) HAADF and (b) ABF modes for sputtered $MoS_2$ film obtained with RF power of 40 W at 300°C following sulfur annealing. . . . . 50
4.10 (a) Schematic of TEM observation structure for $MoS_2$ film. (b) STEM image of 1 monolayer (ML)-$MoS_2$ film after S-annealing. . . . . 51
4.11 STEM images of 1 monolayer (ML)-$MoS_2$ films after (a) sputtering and (b) S-annealing. 1ML-$MoS_2$ film was sputtered directly onto TEM grid that consisted of 20-nm-$SiO_x$ membrane. $MoS_2$ microcrystallites are observed in white circles. . . . . 52
4.12 Variation of edge formation energy in $MoS_2$ film as function of chemical potential of sulfur ($\mu_S$) for triangular nanoflakes with different edge configurations [34]. . . . . 53
4.13 Model of S-annealing effect in $MoS_2$ film. I, II, III, and IV are Zigzag-Mo, Antenna-Mo, Zigzag-S, and Antenna-S edge structures in $MoS_2$ film. . 53
4.14 FWHM values in a wafer for $E^1_{2\mathrm{g}}$ and $A_{1\mathrm{g}}$ modes from the Raman spectra for as-sputtered and S-annealed $MoS_2$ films as function of substrate temperature during sputtering ($T_{\mathrm{flux}}$). . . . . 54
4.15 Relationship between FWHM values for $E^1_{2\mathrm{g}}$ and $A_{1\mathrm{g}}$ modes of as-sputtered and S-annealed $MoS_2$ films from Figure 4.14. The average values of two-point data for each condition in Figure 4.14 are plotted. . . . . 55

4.16 (a) $MoS_2$ Raman peak intensities and (b) Raman peak shift depending on amount of S defects ($V_s$) [31]. . . . . . . . . . . . . . . . . . . . . . . . . 56
4.17 Dependence of $A_{1g}$-$E^1_{2g}$ shift values after sputtering and S-annealing on sputtered substrate temperature ($T_{sub.}$). Diamond data are those values for 1–6 monolayers (ML) exfoliated $MoS_2$ films [35]. . . . . . . . . . . . . . 57
4.18 XPS spectra of molybdenum $3d$ in as-sputtered $MoS_2$ films obtained with substrate temperatures of (a) 300 and (b) 500°C for RF power of 40 W under Ar gas pressure of 0.55 Pa. . . . . . . . . . . . . . . . . . . . . . . . 59
4.19 XPS spectra of sulfur $2p$ in as-sputtered $MoS_2$ films obtained with substrate temperatures of (a) 300 and (b) 500°C for RF power of 40 W under Ar gas pressure of 0.55 Pa. . . . . . . . . . . . . . . . . . . . . . . . . . . . . 59
4.20 (a) planner TEM image of amorphous $MoS_2$ [36]. (b) Raman peak results notarized by Si peak intensity of $MoS_2$ film after sputtering at sputtering substrate temperatures ($T_{sub.}$) of 200, 300, and 500°C. amorphous peaks. The peak of amorphous $MoS_2$ is located at 230-240 $cm^{-1}$ [36–38]. . . . 61
4.21 Comparison of reaction models in S-annealing at sputtering substrate temperatures of 200, 300, and 500°C. . . . . . . . . . . . . . . . . . . . . . . 61

5.1 Approach of long surface migration length of particles on substrate by high flux temperature ($T_{flux}$) with increase in RF power. . . . . . . . . . . . 64
5.2 Schematic of (a) sputtering and (b) sulfur-vapor annealing (S-annealing) systems [39]. . . . . . . . . . . . . . . . . . . . . . . . . . . . . . . . 65
5.3 Deposition rate on RF power of $MoS_2$ films after S-annealing. All samples were deposited by sputtering at 300°C using Ar pressure of 0.5 Pa. . . 65
5.4 Experimental setup for ion energy distribution (IED) with retarding field energy analyzer (RFEA) systems during RF magnetron sputtering with $MoS_2$ target. Left inset is cross-sectional structure of RFEA. . . . . . . 66
5.5 Cross-sectional TEM images of $MoS_2$ films (a)–(c) after sputtering and (d)–(f) after S-annealing [39]. . . . . . . . . . . . . . . . . . . . . . . . . . 67
5.6 FWHM values of $E^1_{2g}$ and $A_{1g}$ modes at three points on $MoS_2$ films after sputtering and S-annealing, plotted as function of RF power. . . . . . . 68
5.7 Raman peak shift values of $A_{1g}$-$E^1_{2g}$ at three points on $MoS_2$ films after sputtering and S-annealing, plotted as function of RF power. Diamond data are those values for 1–6 monolayers (ML) exfoliated $MoS_2$ films [35]. 68
5.8 (a) Model of $MoS_2$ film formation considered with formations of sulfur defects and amorphous/microcrystalline regions during sputtering. (b) Schematic of S-annealing effects and its limitation for $MoS_2$ film by sputtering. . . 70
5.9 (a) Cross-sectional TEM image of $MoS_2$ film formed by sputtering and S-annealing. (b) Mo $3d$ and (c) S $2p$ depth profiles of XPS [40]. Black arrow indicates direction of lower layer. . . . . . . . . . . . . . . . . . . . . . 71

5.10 AFM images of $MoS_2$ films (a) after sputtering with RF power of 50 W and (b) after S-annealing. Root mean square values of roughness are 0.20 and 0.08 nm, respectively. . . . . . . . . . . . . . . . . . . . . . . . . . . . 71
5.11 (a) Schematic of in-plane X-ray diffraction. (b) Relationship between crystallite size and grain size in $MoS_2$ film. . . . . . . . . . . . . . . . . . . . 72
5.12 (a) XRD patterns and (b) calculated grain size of $MoS_2$ films after sputtering and S-annealing, plotted as function of RF power [39]. . . . . . . . 72
5.13 (a) Positive and (b) negative ion energy distributions (IEDs) using REFA systems during $MoS_2$ sputtering. RF power was varied from 50 to 150 W. 74
5.14 (a) Ion flux, (b) average energy and (c) ion energy flux of positive and negative ions reaching the substrate surface as function of RF power. (a) and (b) are measured from RFEA systems, and (c) is calculated from product of (a) and (b). . . . . . . . . . . . . . . . . . . . . . . . . . . . . . . . 74
5.15 Schematic of surface migration models of sputtered particles on the substrates during $MoS_2$ film deposition by sputtering. . . . . . . . . . . . . 75

6.1 Diagram showing particle flux and nucleation density on the substrate surface. Assumptions for at (a) high and (b) low particle flux, respectively. 78
6.2 Schematic of $MoS_2$ low-particle-flux sputtering systems using molybdenum grid, of which the projected aperture (PA) ratio was varied as 100, 60 and 27%. . . . . . . . . . . . . . . . . . . . . . . . . . . . . . . . . . . . . 80
6.3 Dependence of $MoS_2$ deposition rate on PA ratio of molybdenum grid. All thicknesses of $MoS_2$ films are less than 5 nm without perpendicular growth. . . . . . . . . . . . . . . . . . . . . . . . . . . . . . . . . . . . 80
6.4 Schematic of TEM observation structure for $MoS_2$ film. . . . . . . . . . 81
6.5 (a) Raman spectra of $MoS_2$ films prepared with different deposition rates. (b) FWHM values of the $A_{1g}$ and $E^1_{2g}$ peaks in five spectra for each wafer [41]. 82
6.6 Deposition rate dependence of $A_{1g}$-$E^1_{2g}$ shift. Diamond data are those values for 1–6 monolayers (ML) exfoliated $MoS_2$ films [35]. . . . . . . . . . . . 83
6.7 Layer number dependence of $A_{1g}$-$E^1_{2g}$ shift of $MoS_2$ film with and without grid. Diamond data are those values for 1–6 monolayers (ML) exfoliated $MoS_2$ films [35]. . . . . . . . . . . . . . . . . . . . . . . . . . . . . . 84
6.8 (a) Wide- and (b) narrow-range in-plane XRD patterns of $MoS_2$ films sputtered with different PA ratios [41]. . . . . . . . . . . . . . . . . . . . . 86
6.9 Calculated crystallite of $MoS_2$ films as function of deposition rate [41]. 87
6.10 (a) Plan-view HAADF-STEM images of 1 monolayer (ML)-$MoS_2$ film prepared with $MoS_2$ deposition rate of 0.19 nm/min. 1ML-$MoS_2$ film was sputtered directly onto TEM grid that consisted of 20-nm-$SiO_x$ membrane. Inset in the upper right of (a) is fast Fourier transform (FFT) image of the red framed area. (b) Enlarged view of (a). . . . . . . . . . . . . . . . . 88

6.11 ACOM-TEM grain orientation maps for 1-ML-$MoS_2$ films deposited at deposition rates of (a) 0.97 and (b) 0.19 nm/min, respectively. . . . . . . 89
6.12 (a) Grain size histogram of $MoS_2$ films, as calculated from the results in Figure 6.11. (b) Fitting results using log-normal distribution function for (a). . . . . . . 90
6.13 Enlarged grain grain orientation map for 1-ML-$MoS_2$ films deposited at deposition rates of 0.19 nm/min. . . . . . . 91
6.14 (a) $A_{1g}$-$E^1_{2g}$ shift value of $MoS_2$ film with largest grain size deposited in this study. $\Delta(A_{1g}$-$E^1_{2g})$ is equal to the difference between $(A_{1g}$-$E^1_{2g})$ shift values of the $MoS_2$ film and that with $V_s$ of 0%. (b) Dependence of $\Delta(A_{1g}$-$E^1_{2g})$ Raman shift values on sulfur defect density ($V_s$) in $MoS_2$ film [42]. . . . 92
6.15 (a) Atomic positions of monolayer $MoS_2$ with no sulfur vacancies and with 3% sulfur vacancies. Sulfur and molybdenum atoms are magnified to represent their distribution. The band structure obtained using DFT is shown, respectively [29]. (b) Previous research of calculated carrier mobility depending on sulfur defect density [29]. . . . . . . 92

7.1 Average grain or crystallite size depending on formation temperature of $MoS_2$ film. . . . . . . 96
7.2 Benchmark: Dependence of grain or crystallite size on formation temperature of the $MoS_2$ film. . . . . . . 97
7.3 $A_{1g}$-$E^1_{2g}$ Raman shift dependence on Ar pressure. . . . . . . 98
7.4 Model of damage formation in graphene nanosheet caused by recoil argon during low-pressure sputtering [43]. . . . . . . 99
7.5 Schematic of improving $MoS_2$ film quality by optimizing Ar pressure during sputtering. . . . . . . 99
7.6 Schematics of atomic layer etching (ALE) for $MoS_2$ microcrystalline using $Cl_2$ gas [44]. . . . . . . 100
7.7 Previous research on selective area deposition (SAD). ( i ) Selective nucleation growth of $MoS_2$ from Au electrode edges [45]. (ii) van der Waals epitaxial growth of $MoS_2$ from sapphire substrate with selected areas [46]. 101
7.9 Approaches to achieving higher-quality $MoS_2$ films by extending the surface migration length of sputtered particles and supplying additional sulfur flux during sputtering. . . . . . . 102
7.8 Summary of crystal size as function of the $A_{1g}$-$E^1_{2g}$ Raman shift in the $MoS_2$ film deposited by sputtering in this study. A small $A_{1g}$-$E^1_{2g}$ Raman shift indicates a low sulfur defect density. . . . . . . 103

B.1 (a) Mechanism of $MgF_2$ sputtering using Mesh electrodes and potential distribution during retarding voltage application. (b) Absorption coefficient from photoluminescence (PL) measurement varying mesh retarding voltage. In blue circles, absorption coefficient decreased, and $MgF_2$ film quality was improved [47]. . . . . . . . . . . . . . . . . . . . . . . . . . . . . . . . . 122
B.2 RF magentron sputter using Mo-mesh electrodes. . . . . . . . . . . . . . . 123
B.3 Raman peak shift values of $MoS_2$ film deposited by sputtering applied with different $2^{nd}$ mesh electrode. . . . . . . . . . . . . . . . . . . . . . . . . . 124
B.4 Model of potential distribution in sputtering apparatus applying negative voltage to $2^{nd}$ mesh electrode. $1^{st}$ mesh voltage was set to 0 V. . . . . . 124

# List of Tables


1.1 Relationships between device and circuit parameters and scaling factor [4]. 4

1.2 Benchmark of $MoS_2$ devices fabricated by various methods. . . . . . . . 13

3.1 Mean free path $\lambda$ for thermalized particles at 0.4 Pa and 0.5 Pa in Ar gas. 34

3.2 Activation energy for desorption of Mo and S atoms from various sources. 41

4.1 S/Mo ratio in bulk $MoS_2$ under different vacuum annealing temperatures [33]. 44

5.1 RF power dependence of self-bias ($V_{DC}$) of sputtering target surface. . . 73

6.1 Assumption of number of particles and flux behavior with and without Mo-grids. . . . . . . . . . . . . . . . . . . . . . . . . . . . . . . . . . . . . 79

6.2 Comparison of average grain sizes and standard deviations with and without grid. . . . . . . . . . . . . . . . . . . . . . . . . . . . . . . . . . . . . . 89

6.3 Comparison of grain size and mobility for various formation methods. . 93

A.1 Benchmark of large-area $MoS_2$ films. SC: Single crystal, PC: Polycrystal. 120

B.1 Conditions of applying the mesh electrodes. . . . . . . . . . . . . . . . . 122

# Chapter 1

# Research background and motivation

## 1.1 Logic transistor scaling and next-generation transistors

The explosive growth of data and the processing required to convert it into useful information have created an unprecedented demand for energy-efficient computing. Low-power and high-speed computing is also crucial for edge AI processing for the Internet of Things (IoT), as shown in Figures 1.1 and 1.2 [1, 2].

To meet the demand for modern semiconductor devices, scaling down transistor dimensions has a significantly positive impact on key performance metrics, as described by R. Dennard in 1974, illustrated in Figure 1.3 [4]. The scaling factors for various device or circuit parameters are summarized in Table 1.1. In this device scaling, the voltage, current, and delay time are reduced by $1/k$, while the power dissipation per circuit is reduced by $1/k^2$. The transistor scaling is progressing, and high-performance computing is being miniaturized according to Moore's Law [5, 48–54]. With miniaturization, the technology node of transistors improves year by year. Gate length, metal wiring pitch, speed, power consumption, supply voltage, etc., are miniaturized and reduced, as shown in Figures 1.4 and 1.5. However, since around 2020, it has been considered that performance improvement by simple transistor scaling has reached saturation.

(a)

(b)

**Figure 1.1**: (a) Image of data center and schematic of (b) Internet of Things (IoT) [1,2].

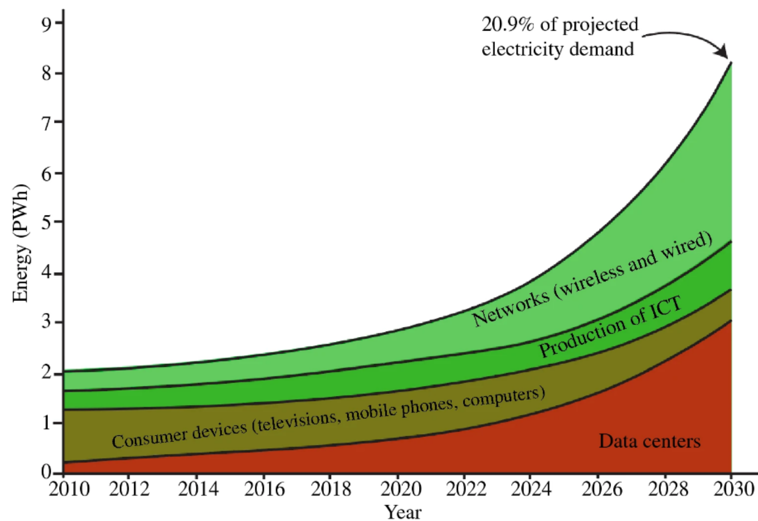


**Figure 1.2**: Forecast of energy usage in information and communication technologies (ICT). By 2030, data centers are likely to constitute 8% of global electricity demand, and ICT could use 20% of it [3].

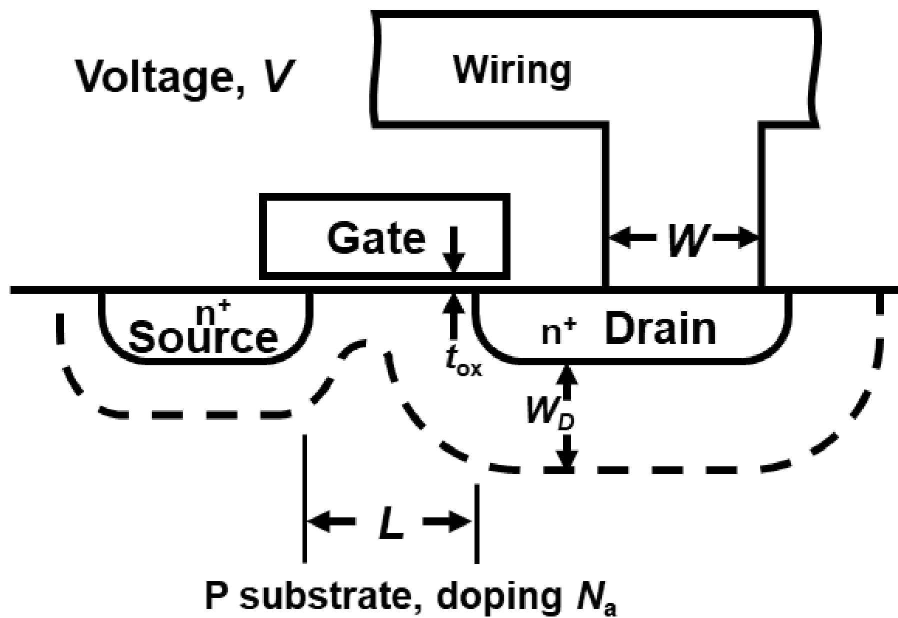


**Figure 1.3**: MOSFET device structure for electrical-field-scaling [4].

**Table 1.1**: Relationships between device and circuit parameters and scaling factor [4].

| Device or circuit parameter | Scaling factor |
|---|---|
| Device dimension $L, W, t_{ox}$ | $1/k$ |
| Doping concentration $N_a$ | $k$ |
| Voltage $V$ | $1/k$ |
| Electric field | 1 |
| Current $I$ | $1/k$ |
| Capacitance $\epsilon$A/t | $1/k$ |
| Circuit delay time $VC/I$ | $1/k$ |
| Power dissipation/circuit $VI$ | $1/k^2$ |
| Power density $VI/A$ | 1 |

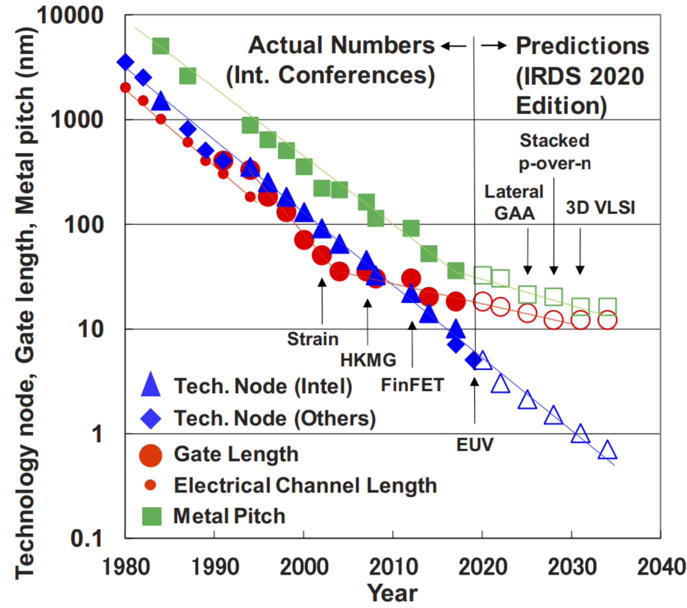


**Figure 1.4**: Transition and future forecast of Technology node, gate length, and metal pitch [5].

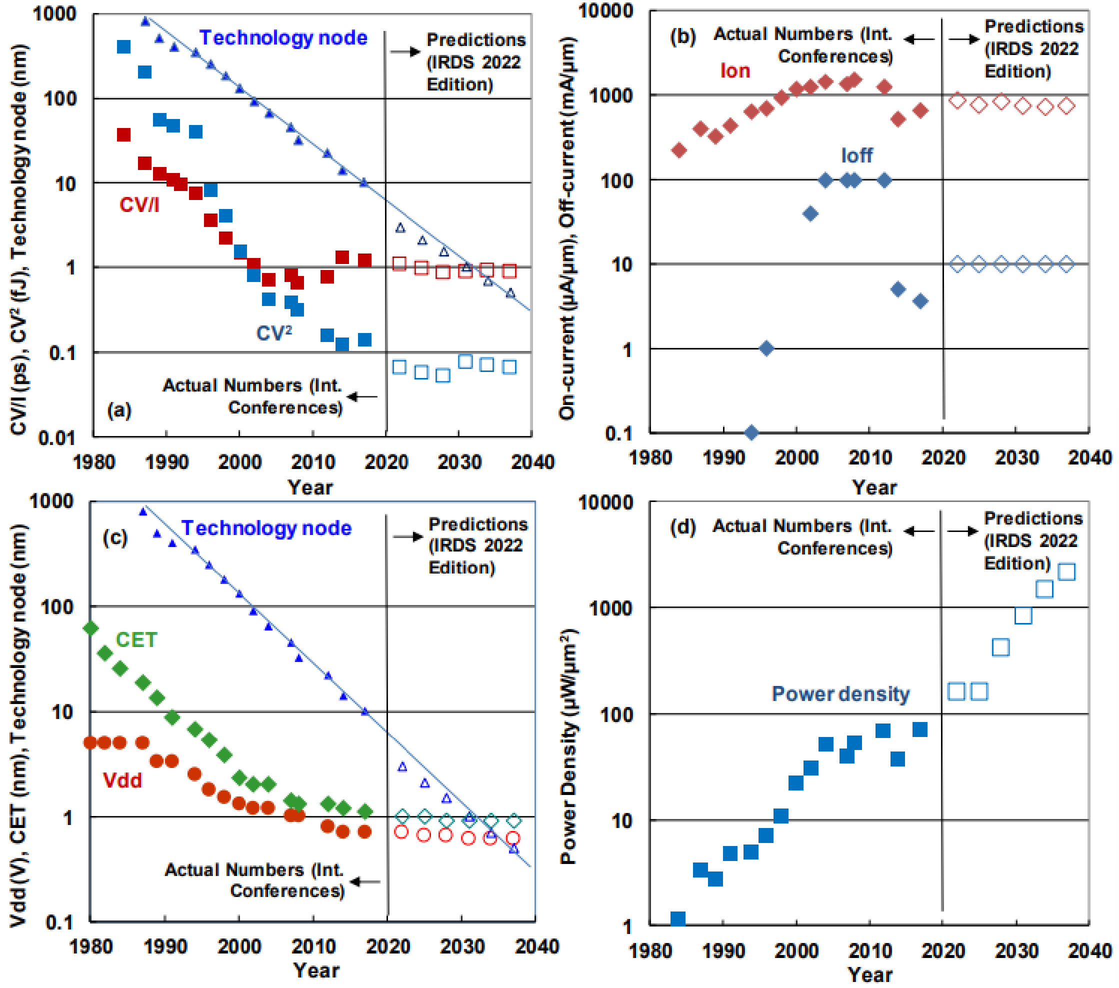


**Figure 1.5**: Trends of (a) speed ($CV/I$) and energy ($CV^2$), (d) on-current ($I_{\text{on}}$) and off-current ($I_{\text{off}}$), (c) supply voltage ($V_{\text{dd}}$) and equivalent capacitance thickness (CET), and (d) power density of high-performance (HP) transistors in the past and future. Technology node is also shown in (a) and (c). It is assumed that gate width $W = 10L_g$ in planar transistors, fin number reduced from 3 (2012) to 1 (2024), GAA stacked sheet number increased from 3 (2025) to 4 (2031), CFET was introduced in 2028, and stacked tier number increased from 2 (2031) to 6 (2037), and FO = 1. $I_{\text{on}}$ and $I_{\text{off}}$ are normalized to effective width ($W_{\text{eff}}$), while layout footprint is used to calculate power density [5].

## 1.2 Requirements for next-generation semiconductor channel materials

The short channel effect caused by the channel length scaling causes off-current and increases power consumption. As shown in Figure 1.6, the transistor structure is changing to improve this. The technology node shows the transistor specifications, and the Fin

structure has reached the 3nm technology node [6]. It has been changed to a gate-all-around nanosheet (GAA-NA) structure and is scheduled to move to a stacked n/p structure [7–10]. These structural changes will increase the effective channel width, suppress the short channel effect, and improve the transistor per footprint.

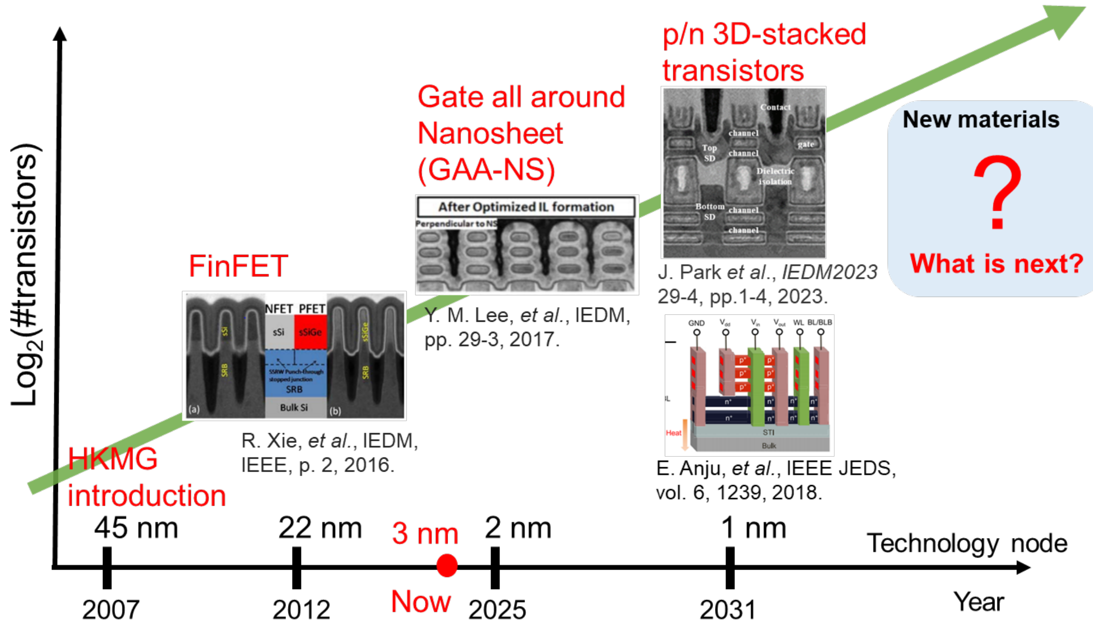


**Figure 1.6**: Transistor scaling and next generation structures for high-performance logic transistor [6–10].

Furthermore, to achieve even higher performance, the delay time and the power consumption of transistors are shown in the following equations:

- Delay time:

$$\tau = C \cdot \frac{V_{\text{dd}}}{I_{\text{on}}}, \tag{1.2.1}$$

where $C$ is the capacitance, $V_{\text{dd}}$ is the supply voltage, and $I_{\text{on}}$ is the on-current.

Moreover, active and standby power densities, which is a critical factor for circuit performance, can be expressed as:

- Active Power:

$$\frac{VI}{A} = \frac{V_{\text{dd}} \cdot I_{\text{on}}\,[\text{A}/\mu\text{m}]}{L_g\,[\mu\text{m}]}, \tag{1.2.2}$$

where $L_g$ is the gate length.

- Standby Power:

$$P_{\text{standby}} = I_{\text{leak}} \cdot V_{\text{dd}}. \tag{1.2.3}$$

where $I_{\text{leak}}$ is the leak current.

To achieve the short delay time from Equation. 1.2.1, reducing the ($V_{\text{dd}}$) and enhancing the $I_{\text{on}}$ are desirable. Low power consumption from the above equations, reducing the supply voltage ($V_{\text{dd}}$) is essential to achieve low delay and low power consumption, which requires high-mobility channel materials and a slight subthreshold slope (SS). Additionally, as illustrated in Figure 1.3, reducing $V_{\text{dd}}$ alongside optimized device geometry (for example, shorter gate lengths and increased fin aspect ratios) can enhance ON resistance while decreasing power density.

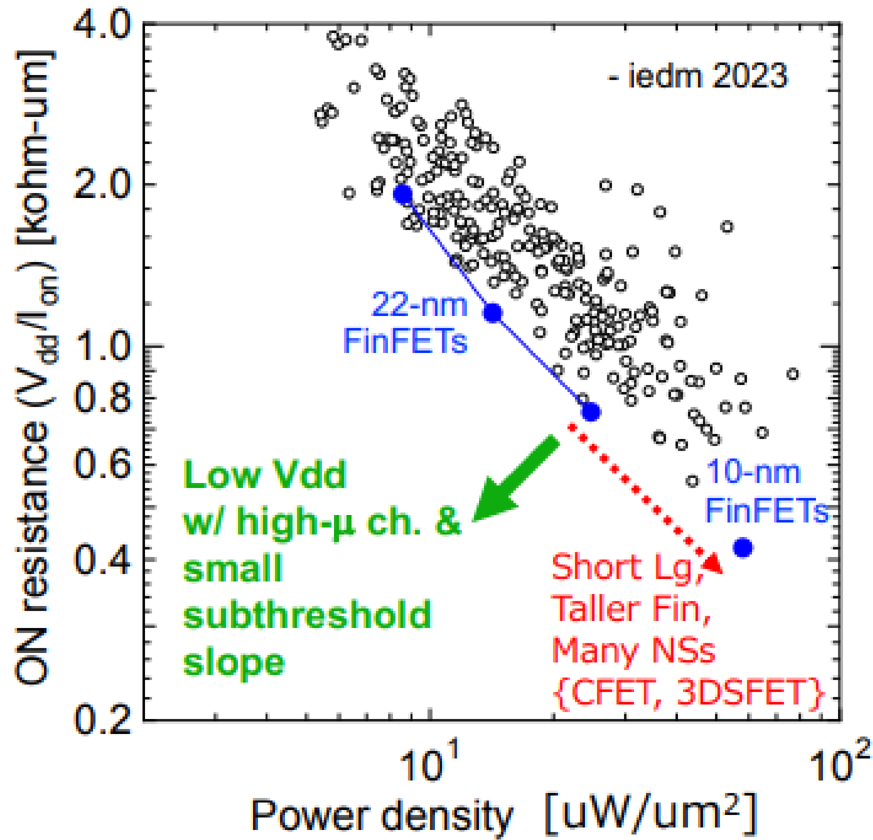


**Figure 1.7**: Relationship between power density and ON resistance for various device architectures [11].

## 1.3 Transition metal di-chalcogenide (TMDC) and molybdenum disulfide ($MoS_2$)

Silicon (Si) has been used as a channel material for cutting-edge logic semiconductors. However, the mobility of Si drops sharply in atomic layer thin films with a thickness of 3 nm or less. Therefore, materials that do not drop in mobility even in atomic layer thin films are being searched for, one of which is transition metal dichalcogenides (TMDCs). TMDCs are one of the two-dimensional materials similar to graphene, represented by $MX_2$, and have a structure in which a transition metal element M (Mo, W, Zr, etc.) is sandwiched between two chalcogen elements X (S, Se, Te, etc.) as shown in Figure 1.8. Van der Waals forces bond the layers, so there are no dangling bonds. As shown in Figures 1.9 (a) and (b), high mobility with various band gaps can be obtained even with a thickness of 3 nm or less in TMDC films.

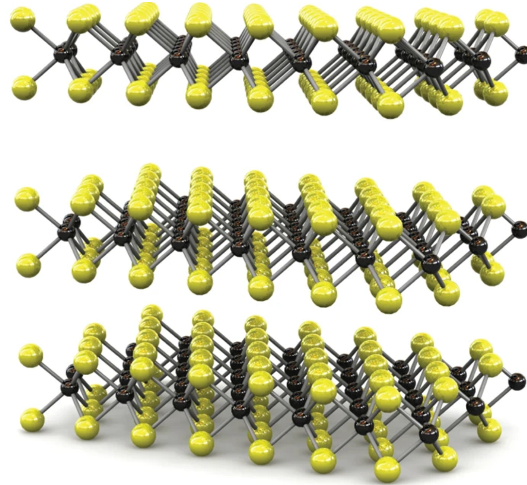

**Figure 1.8**: Schematic diagram of transition metal dichalcogenide (TMDC). Black dots indicate transition metal elements, and yellow dots indicate chalcogen elements. Layers are bonding together by van der Waals forces [12].

Among TMDC materials, molybdenum disulfide ($MoS_2$) is so stable that it is abundant in nature and exhibits semiconducting properties. Therefore, many research institutes have reported the demonstration of transistors and applications to devices such as nanosheet FETs, sensors, and optoelectronic devices are expected [12, 55–59]. $MoS_2$ has an interlayer distance of 0.65 nm and exhibits mobility of 190-400 $cm^2/Vs$ [12, 60], as shown in Figure 1.10 (a). In addition, it is reported that lower subthreshold swing (SS) can be achieved with low $L_g$ (< 10 nm), than with Si [15], as shown in Figure 1.10 (b). Furthermore, in the bulk state, it is an indirect transition semiconductor with a band gap

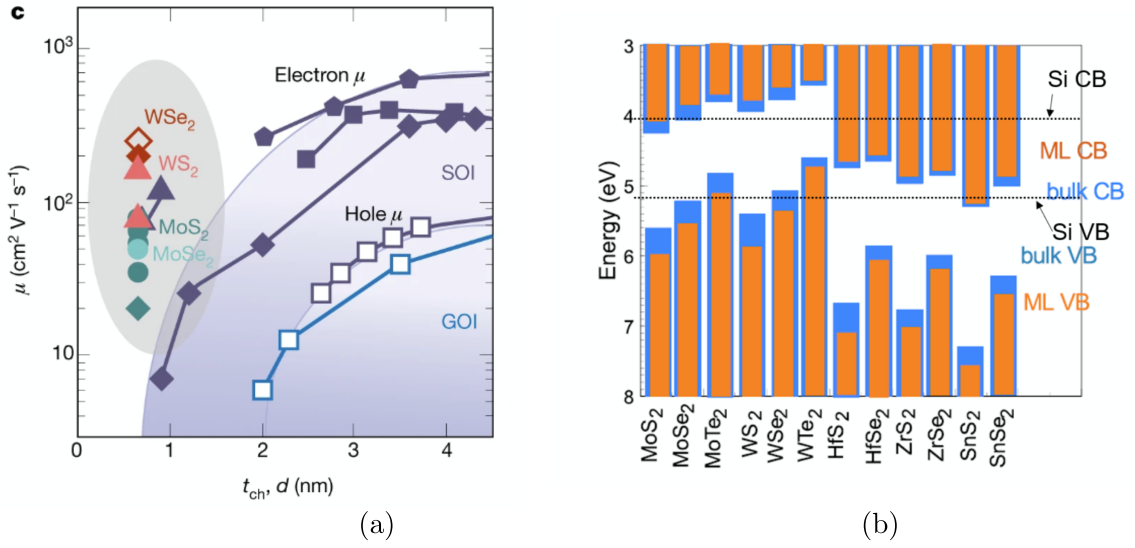


(a) (b)

**Figure 1.9**: Benchmark of mobility on traditional and 2D semiconductors depending on channel thickness ($t_{ch}$) [13]. (b) Band edge positions and band gaps of various TMDC films [14].

of approximately 1.2 eV, while in the single layer, it exhibits the properties of a direct transition semiconductor with a band gap of approximately 1.9 eV [61, 62].

Moreover, recent research has also been progressing towards future logic devices. Figure 1.11 (a) shows a gate all around (GAA) nanosheet (NS) field electric transistor (FET) using $MoS_2$ film [16]. The GAA structure of the high-k ($HfO_2$)/metal gate (Ti) for the $MoS_2$ channel is confirmed. Figure 1.11 (b) also shows a proposed p/n stacked transistor structure with $MoS_2$ film as n-type semiconductor and $WSe_2$ film as p-type semiconductor, which is expected that $MoS_2$ film will be used for logic channels in the future [17].

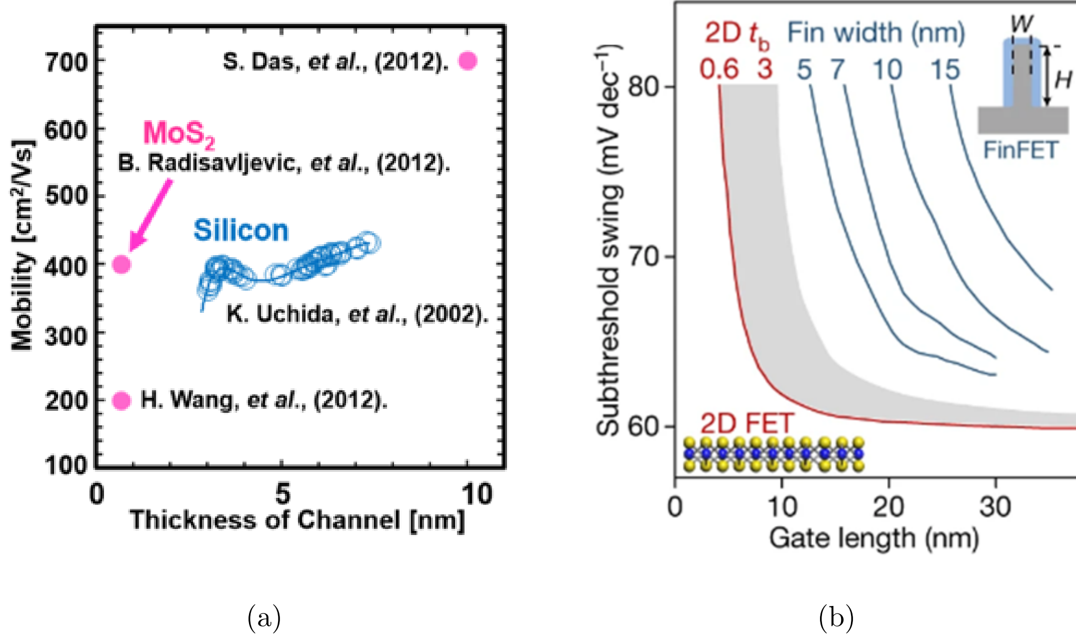


(a) (b)

**Figure 1.10**: (a) Mobility benchmark depending on $MoS_2$ and Silicon channel thickness. (b) Benchmark subthreshold swing depending on gate length ($L_g$) in $MoS_2$-FET compared from Si-FinFET [15].

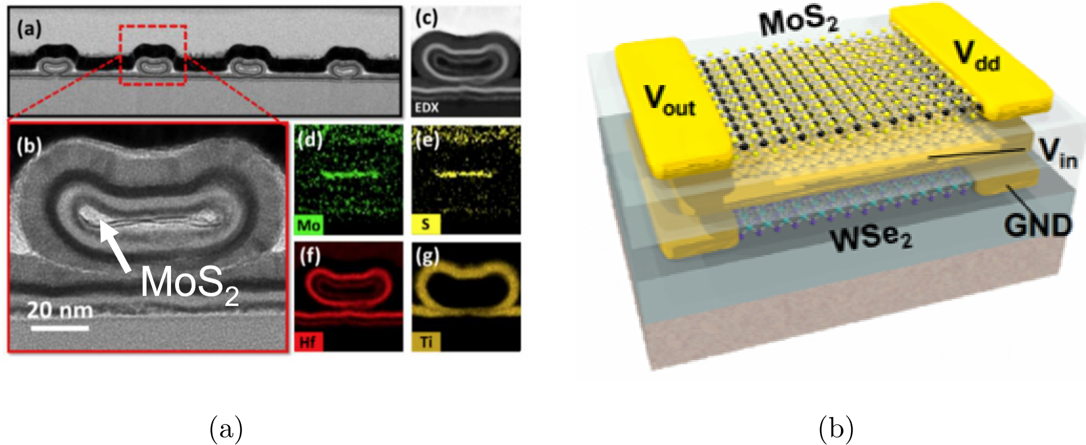


(a) (b)

**Figure 1.11**: (a) Schematic diagram of gate all around (GAA) nano-sheet (NS) field electric transistor (FET) using $MoS_2$ film [16]. (b) Schematic of p/n 3D-stacked FETs using $MoS_2$ film [17].

## 1.4 $MoS_2$ film formation methods

Conventional synthesis methods for $MoS_2$ film formation are exfoliation and chemical vapor deposition (CVD). Figure 1.12 (a) shows the exfoliation method [18], and Fig-

ure 1.12 (b) shows the CVD method [63]. Exfoliation is a method that uses scotch tape for the $MoS_2$ bulk and transfers $MoS_2$ film to the substrate. It enables us to make good quality films and high mobility (~380 $cm^2/Vs$) [12,18]. However, it is not possible to make large films. In addition, its carrier density is automatically high because of alkali metal contamination. And it is difficult to control these impurities [64]. The $MoS_2$ film formation by CVD is adopted as a popular method capable of forming large films [17, 63, 65]. In the CVD method, $MoS_2$ is formed on the substrate by a chemical reaction of evaporated precursors (like $MoO_3$ and S). $MoS_2$ film by CVD has high quality, good electric properties, and large grain. However, to obtain a good CVD-$MoS_2$ film with large crystal grains, there are some problems, such as the necessity of applying perylene-3,4,9,10 tetracarboxylic acid tetrapotassium salt (PTAS) to the base substrate [17,63]. Furthermore, even if a promoter is not used, a high-temperature process of 800°C or higher is required to deposit high-quality films. The deposition time is extended to at least one hour per wafer [17], leading to problems with production time and heat resistance. Therefore, a large-area formation without special treatment has been investigated to suppress contamination.

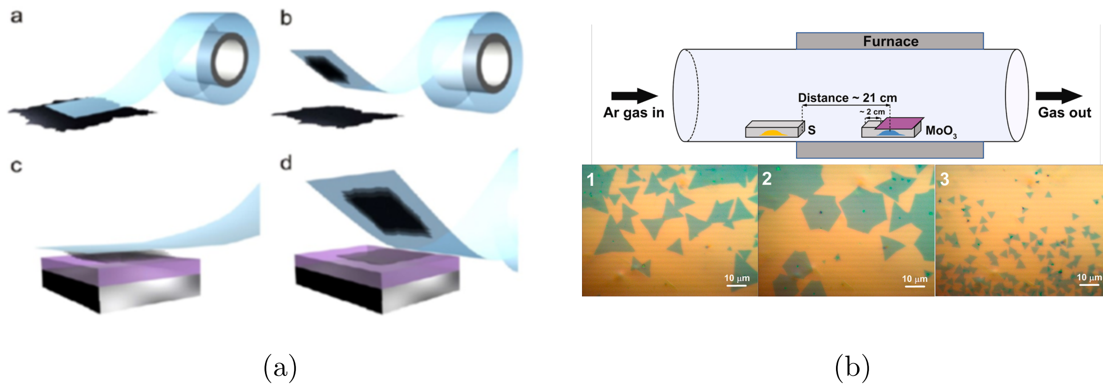


(a) (b)

**Figure 1.12**: Schematic illustrations of standard 2D film fabrication methods. (a) Micromechanical exfoliation of 2D material [18]. (b) CVD for $MoS_2$ film fabrication [17].

From the above, to achieve industrial application of FETs using $MoS_2$ film, we adopt radio frequency (RF) magnetron sputtering for $MoS_2$ thin film formation. Figure 1.13 (a) shows a conceptual diagram of the RF magnetron sputtering process. Sputter deposition is one of the physical vapor deposition (PVD) methods. The advantages of this method include its ability to deposit films at low temperatures, specifically below 500°C. Additionally, it enables short deposition times, with one layer taking less than one minute. This approach also facilitates the reduction of defect density, demonstrates high compatibility with conventional semiconductor processes, and allows for large-area deposition with minimal thickness variation [19, 19, 66, 67]. Therefore, sputtering is the expected method for the industrial introduction of the device process. However, there are certain limitations. The crystal size is approximately less than 10 nm, and sulfur vacancies are a

notable concern, which leads to deterioration of the crystallinity and electrical properties. Therefore, the process of sulfur compensation is essential. Figure 1.14 shows the schismatics of sulfur vapor annealing, which is called S-annealing. To compensate for the sulfur vacancies in the $MoS_2$ film, S-annealing is conducted [20, 21]. This process significantly reduces the carrier density in the PVD-$MoS_2$ film and enhances its mobility, as illustrated in Figure 1.15 (a). Consequently, as shown in Figure 1.15, this improvement facilitates the realization of normally-off $MoS_2$ nMISFETs [21]. The benchmark of each FET characteristic is shown in Table 1.2. Comparing them, it can be seen that the mobility and $I_{on}/I_{off}$ ratio of sputtered film is degraded compared to exfoliation and CVD methods. Therefore, it is necessary to improve the quality of the $MoS_2$ film by combining sputtering and S-annealing, and it is also desirable to improve the film quality by sputtering alone.

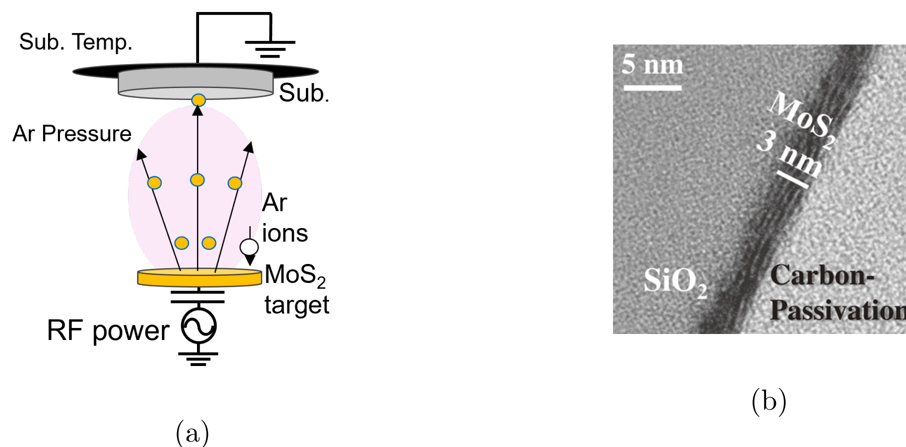


**Figure 1.13**: (a) Schematic image of RF magnetron sputtering (b) TEM image of thin $MoS_2$ film formed by RF magnetron sputtering [19].

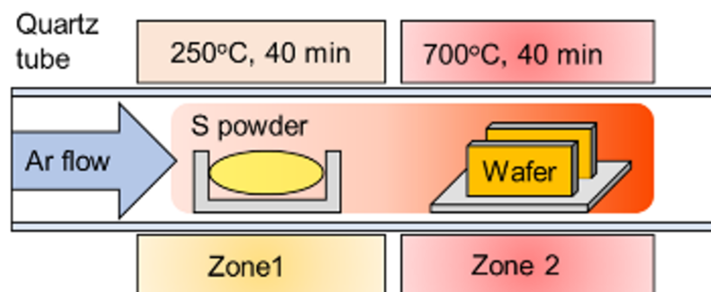


**Figure 1.14**: Schematic of sulfur vapor annealing (S-annealing) [20].

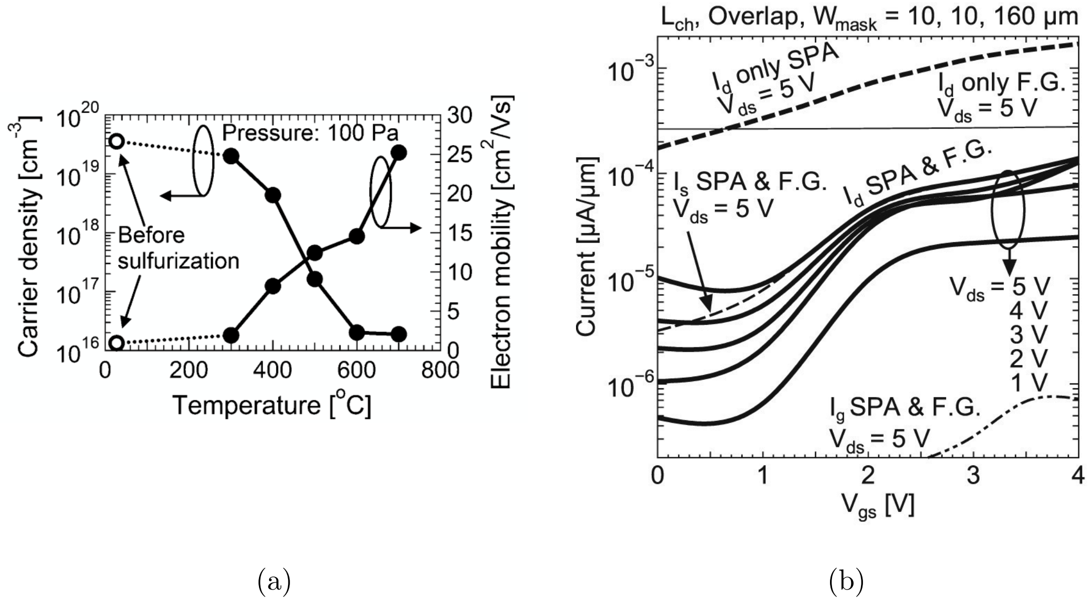


(a) (b)

**Figure 1.15**: (a) Hall-effect measurement results of carrier density and electron mobility for approximately 4-nm-thick $MoS_2$ film as function of temperature [20] and (b) $I_d$-$V_{gs}$ characteristics of metal isolation semiconductor FET (MISFET) with $MoS_2$ film formed by sputtering and S-annealing [21].

**Table 1.2**: Benchmark of $MoS_2$ devices fabricated by various methods.

| Method | Growth Temperature | Mobility [$cm^2/Vs$] | $I_{on}/I_{off}$ Ratio | Reference |
|---|---|---|---|---|
| Sputtering + S-annealing | 400°C (2 min) + 700°C (40 min) | 0.21 | $\sim 10^2$ | [21] |
| Exfoliation | Room temperature (RT) | 700 | $\sim 10^8$ | [68] |
| Exfoliation on PMMA | Room temperature (RT) | 30–60 | $10^4$ | [69] |
| CVD Sulfur + $MoO_3$ | 1100°C (130 min) | $\sim 17$ | $\sim 10^8$ | [70] |
| CVD Sulfur + $MoO_3$ | 850°C (10 min) Transferred from sapphire | 24 | $10^6$ | [71] |

## 1.5 Purpose of this study

From the previous discussion, the objective of this study is to improve the quality of sputtered $MoS_2$ films for future 3D-stacked FETs.

## 1.6 Structure of doctoral thesis

The structure of this paper is shown in Figure 1.16. This paper consists of 7 chapters. Chapter 1 describes the demand and scaling of logic semiconductors, the background of the demand for 2D semiconductors, the reasons for deposition by sputtering, and the current issues with $MoS_2$ films by sputtering. Chapter 2 compares with previous studies and sets the target value for improving the quality of $MoS_2$ films. Chapter 3 examines the elementary reactions of $MoS_2$ film formation using sputtering. To achieve the target value set in Chapter 2, the directions of $MoS_2$ film quality improvement in sputtering film formation are set. Chapter 4 examines the substrate temperature dependence of $MoS_2$ film quality in sputtering film formation. Chapter 5 performs an RF power swing to control the sputtered particles that reach the substrate. This chapter explains how adjusting the particle flux and particle energy when changing the RF power of sputtering can increase the crystal size of $MoS_2$ film. Chapter 6 explains low-particle-flux sputtering, which can increase the crystal size. Finally, Chapter 7 presents the conclusions of the study and further directions.

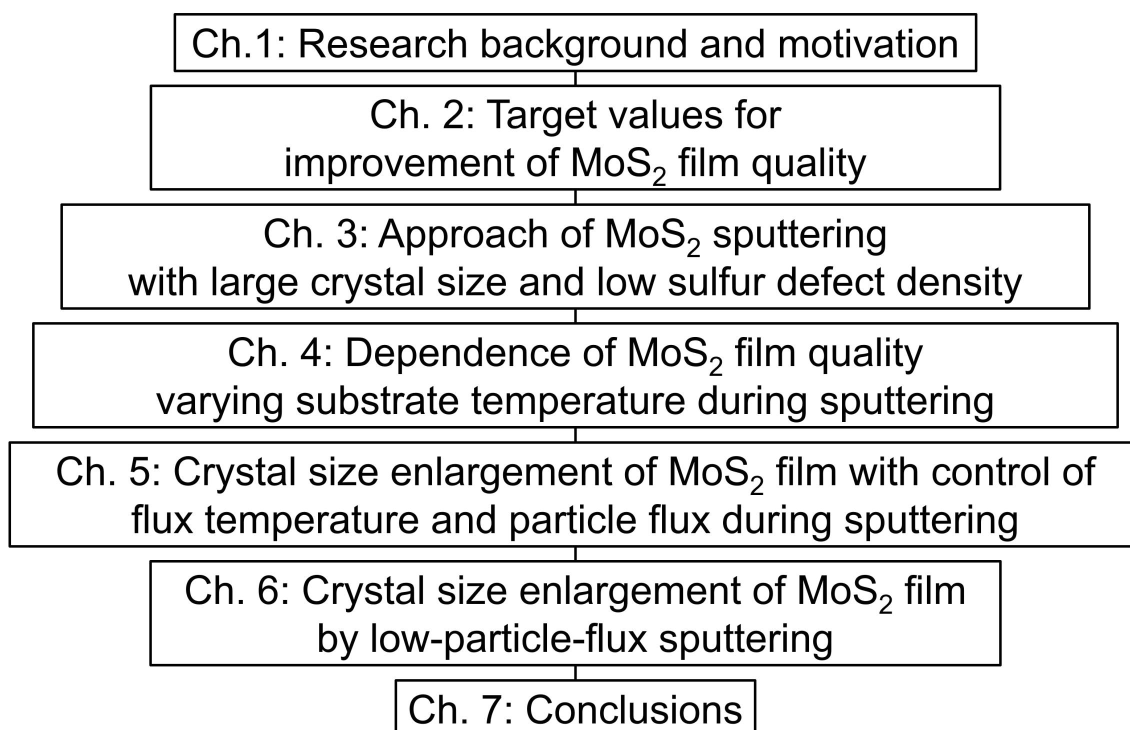


**Figure 1.16**: Structure of this thesis.

# Chapter 2

# Target values for improvement of $MoS_2$ film quality

In this chapter, target values are decided for improving $MoS_2$ film quality compared to the previous reports and future direction. First, the target indicates required to enhance the $MoS_2$ film quality are the following:

- Examination of the upper limit of deposition temperature.
- Achievement of target crystal size.
- Reduction of sulfur vacancy defect density for high-mobility $MoS_2$ films.

These indices are explained in the following sections.

## 2.1 Thermal budget requirement for $MoS_2$ film

To estimate the thermal budget requirement, it is necessary to consider the process of future logic transistors using $MoS_2$ film formation. the process flow for $MoS_2$-NSFET fabrication is shown in Figure 2.1 [16], as follows in the below lists:

1. 2D material/sacrificial layer stacking.
2. Gate patterning.
3. Inner spacer formation.
4. Source/Drain (S/D) contact formation.
5. Plug metal and Chemical Mechanical Polishing (CMP).
6. Nanosheet (NS) patterning.
7. NS release.
8. High-k Metal Gate (HKMG) formation.

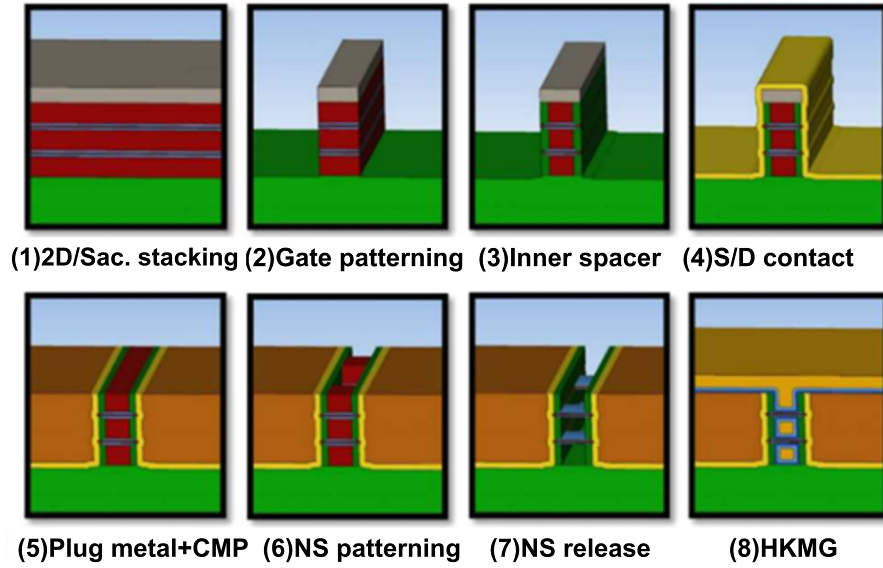


**Figure 2.1**: Process flow of $MoS_2$-nanosheet (NS) field electric transistor (FET) [16].

Figure 2.2 shows the cross-sectional transmission electron microscope (TEM) images of the stacked $MoS_2$/Sacrificial layer during the first process step (1 Stacked 2D epitaxial growth). Stacking the sacrificial (Sac.) layer and $MoS_2$ layer requires a deposition method that does not damage the under-$MoS_2$ layer. Plasma deposition and high-temperature annealing are not permissible due to their potential to cause damage. The formation of source/drain (S/D) contacts necessitates etching the Sac. layer to release the $MoS_2$ layer. During this process, a high etch selectivity of the Sac. layer over the $MoS_2$ layer is essential for successful fabrication [72]. Suitable materials for the Sac. layer include $SiO_2$, $Al_2O_3$, and $HfO_2$, which are amorphous oxides. However, candidates for nitride insulating films such as $SiN_x$ are excluded because they require plasma deposition and high-temperature deposition, which degrade the $MoS_2$ film properties [73, 74].

The effects of low-temperature films on the suppression of oxygen diffusion were analyzed in a previous study [22]. Figures 2.3 (a) and (b) illustrate models of the reactions that occur when $MoS_2$ films are deposited on $SiO_2$ and $Si_3N_4$, followed by high-temperature annealing at 700°C. It has been reported that oxygen diffusion occurs in the $MoS_2$ film on $SiO_2$, while no such diffusion takes place in the $MoS_2$ film on $Si_3N_4$. As shown in Figures 2.4 (a) and (b), XPS measurements confirm the presence of oxygen bonds only in the $MoS_2$ film on $SiO_2$. Therefore, $MoS_2$ is susceptible to damage when the temperature exceeds 700°C. In the presence of oxygen, the material undergoes oxidation, degrading its electrical properties [15, 72]. To ensure the stability of the $MoS_2$ layer during its growth, using low-temperature deposition with a sacrificial layer (Sac. layer) is crucial. The use of low-temperature deposition below 700°C is effective in suppressing oxygen diffusion. This process minimizes the potential for oxygen contamination during $MoS_2$ stacking. It also

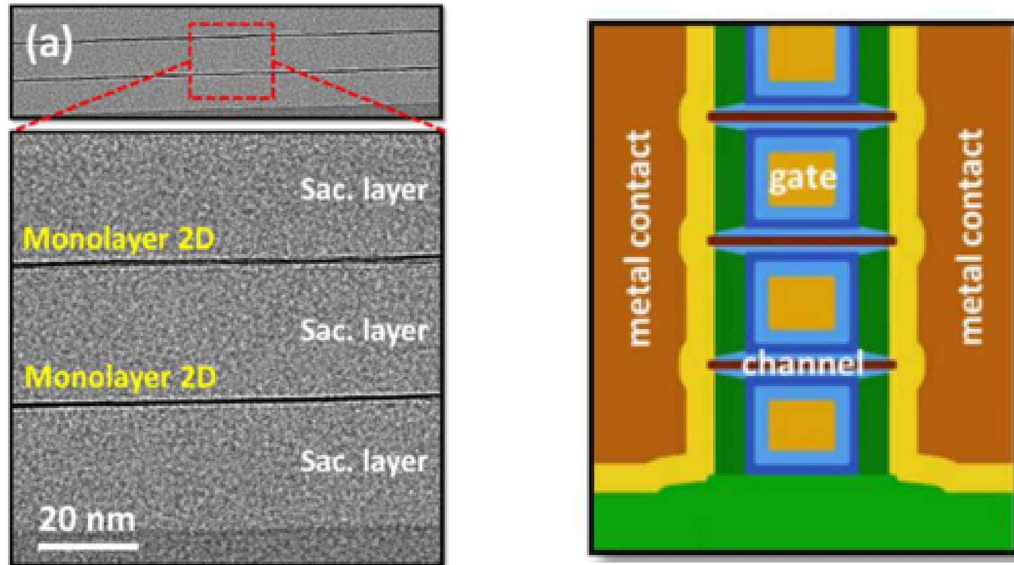


**Figure 2.2**: (a) Cross-sectional transmission electron microscope (TEM) images of stacked $MoS_2$/Sacrificial layer structure and (b) Schematic of $MoS_2$ NS-FET [16].

prevents oxidation during subsequent etching processes for $MoS_2$ removal [72].

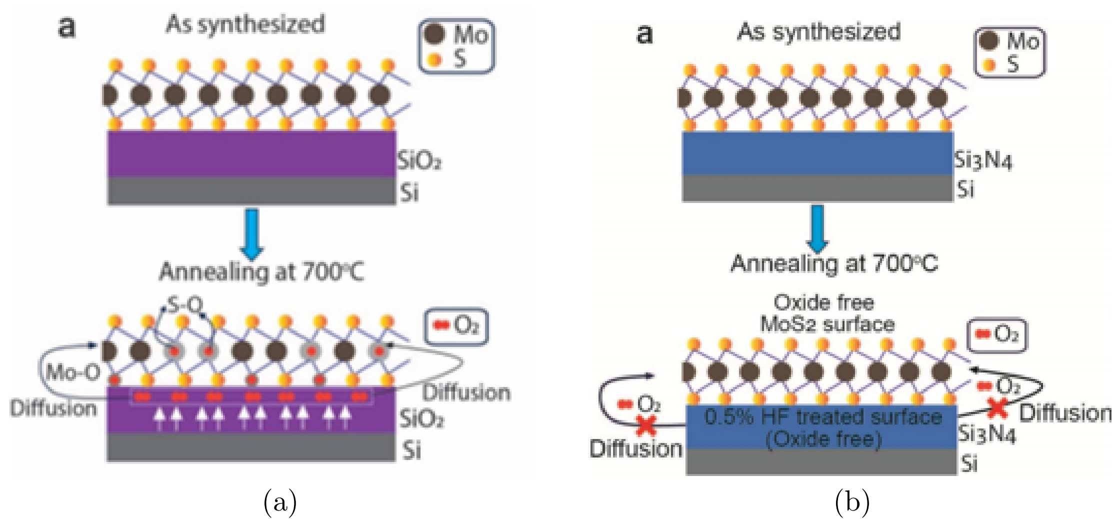


**Figure 2.3**: Model of oxygen diffusion reaction in $MoS_2$ film on (a) $SiO_2$ and (b) $Si_3N_4$ substrate during high-temperature annealing with Ar gas [22].

Furthermore, the deposition and integration of $MoS_2$ films are expected for the back end of line (BEOL) integration in Si-complementary metal-oxide-semiconductor (Si-CMOS) circuits and 2D-CMOS circuits, as shown in Figures 2.5 and 2.6 [23, 24]. Low-temperature

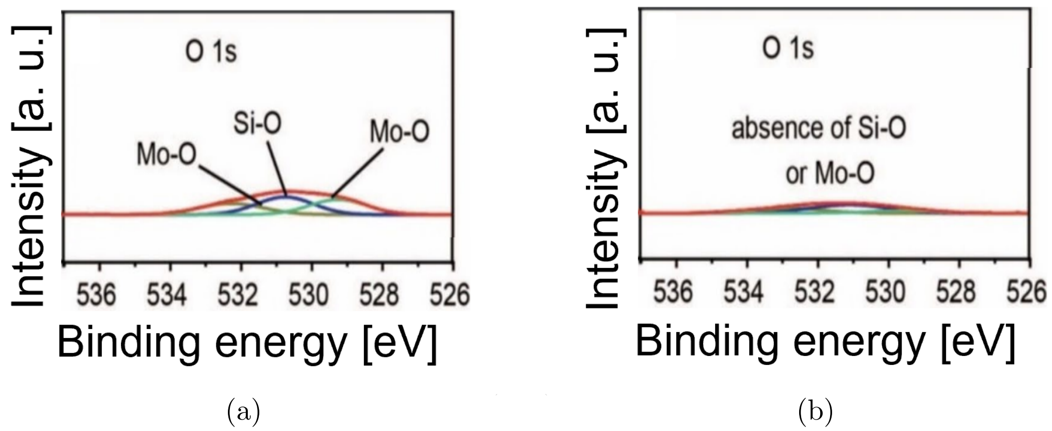


**Figure 2.4**: X-ray photoelectron spectroscopy (XPS) results of O 1*s* orbits in $MoS_2$ film on (a) $SiO_2$ and (b) $Si_3N_4$ after Ar annealing at 700°C from Figure 2.3 [22].

deposition below 400°C is required. Silicon dopant distribution, gate-induced body effect, and interconnect integrity degrade above 400°C.

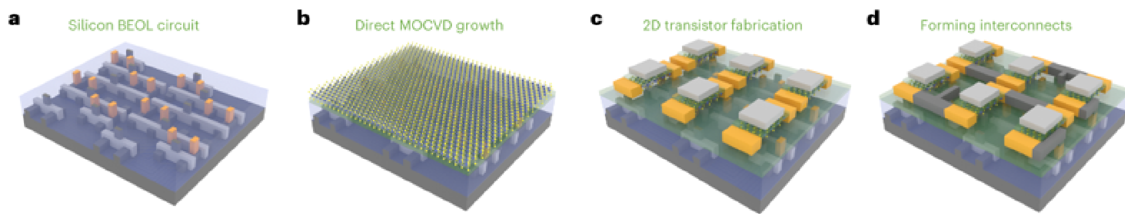


**Figure 2.5**: Process of $MoS_2$ film deposition and device fabrication during back end of line (BEOL) integration in Si-complementary metal-oxide-semiconductor (CMOS) circuits [23].

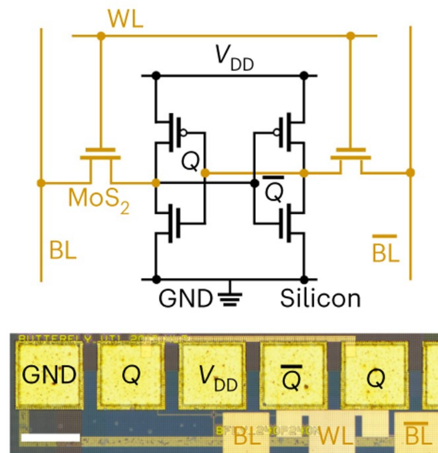


**Figure 2.6**: Static random-access memory (SRAM) circuit utilizing Si transistors in front end of line (FEOL) and $MoS_2$ transistors in back end of line (BEOL) [23].

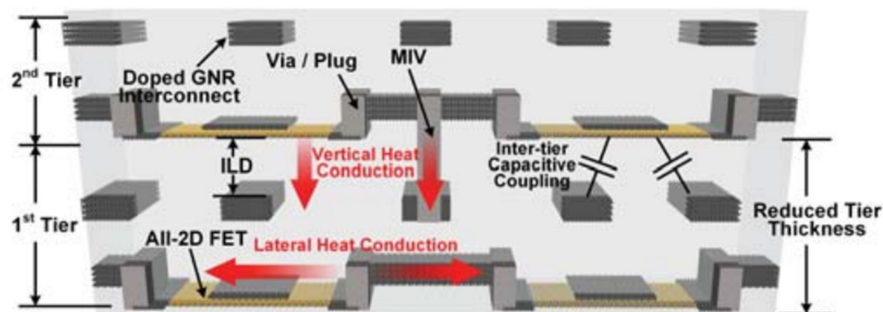


**Figure 2.7**: Schematic of three-dimensional stacked integrated circuits (IC) using two-dimensional channel transistors [24].

The target values for formation temperature are summarized as follows. For $MoS_2$ film using sputtering:

- Direct deposition onto amorphous oxide film.
  - Ease of selective etching compared to $MoS_2$
  - Low-temperature deposition that minimizes damage to $MoS_2$
- Front end of line (FEOL): Deposition at 700°C and less.
- Back end of line (BEOL): Deposition at 400°C and less.

## 2.2 Crystal size requirement

To achieve high-performance devices using $MoS_2$ channels, the transistor's active channel length ($L_{active}$) must be a single crystalline $MoS_2$ film. Therefore, the size of $L_{active}$ for future $MoS_2$-FETs is evaluated. Figure 2.9 illustrates the projected scaling trends for next-generation device architectures such as FinFETs, Gate-All-Around Nanosheet (GAA-NS) transistors, and 3D-Stacked FETs (3DSFETs) [27]. The key parameters for these architectures are the gate length ($L_g$) and the nanosheet width ($W_{NS}$).

Figure 2.8 shows the future FET structure using $MoS_2$ film [25, 26]. $L_g$, $L_c$, and $L_{sp}$ are the gate length, contact length, and spacer length between the gate and source/drain electrodes, respectively. CGP is contacted gate pitch. From the device dimensions in the previous study [26], the critical dimensions for $MoS_2$-based 3D-stacked-FETs are defined as follows:

- Gate length: $L_g = 5.9$ nm
- Spacer length: $L_{sp} = 1$ nm
- Channel length:
$$L_{ch} = L_g + 2L_{sp} = 7.9 \text{ nm}. \tag{2.2.1}$$
- Aspect ratio: $L_g/W \in [0.8, 2.0]$ [75]
- Nanosheet width: $W_{MoS_2} \leq 7.4$ nm

For achieving high-quality $MoS_2$ films, the grain size must exceed:

$$\text{Crystal size} \geq L_{active} = 7.9 \text{ nm}. \tag{2.2.2}$$

Based on these discussions, the goal is to achieve a crystal size of 7.9 nm or more, and the prediction of trends of gate length and nanosheet width are shown in Figure 2.9.

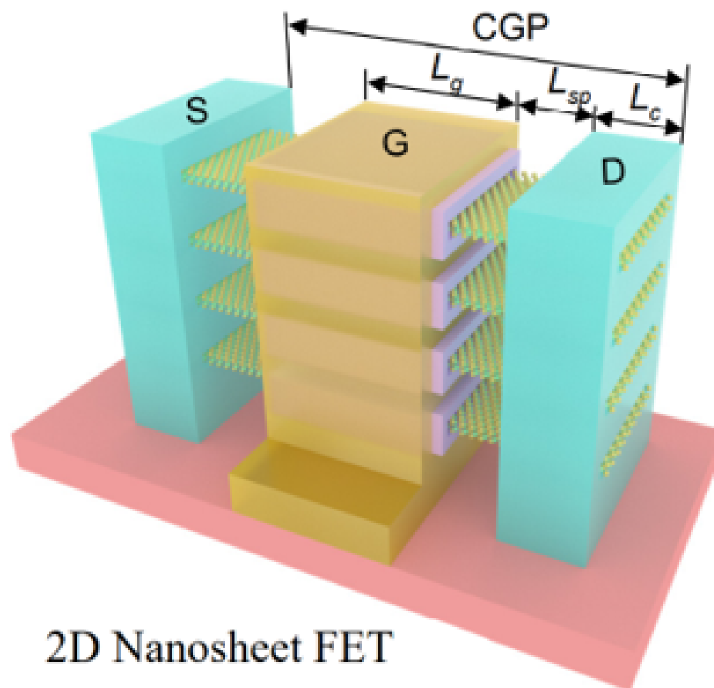


**Figure 2.8**: Schematics of future FET structure using $MoS_2$ film [25, 26]. $L_g$, $L_c$, and $L_{sp}$ are gate length, contact length, and spacer length between gate and source/drain electrodes, respectively. CGP is contacted gate pitch.

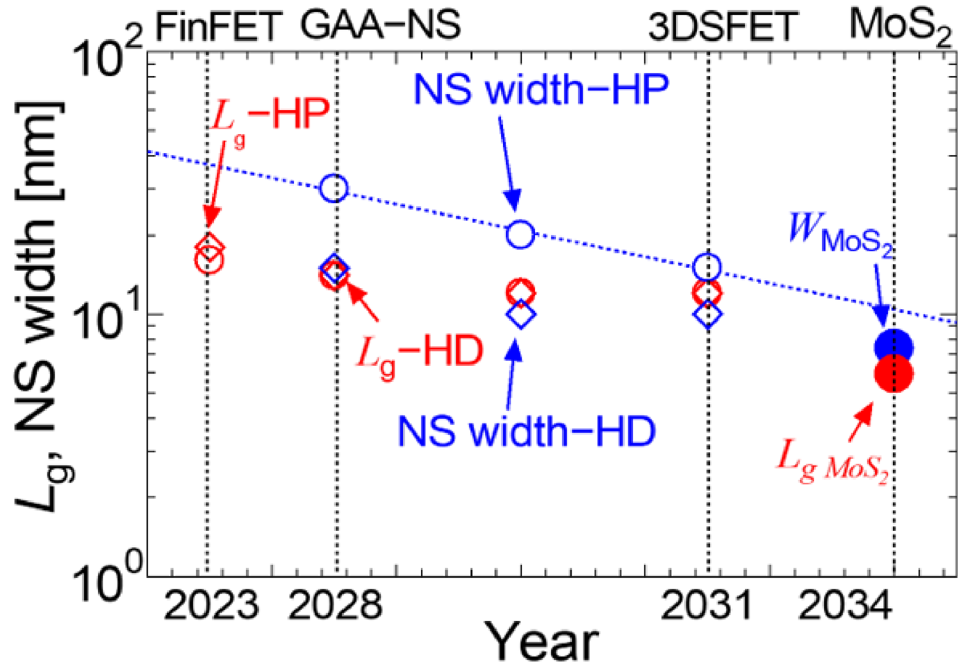


**Figure 2.9**: Prediction trends of gate length ($L_g$) and nanosheet (NS) width ($W$) from 2023 to 2034 [27].

## 2.3 Requirement of mobility in the single crystal $MoS_2$ channel

The ideal mobility of bulk Si is approximately 1400 $cm^2/Vs$ [76]. Figures 2.10 (a) and (b) show the cross-sectional TEM images of Si-gate all around (GAA)-nanosheet(NS)-FET [28]. They have achieved the fabrication of NS-FETs with a Si channel thickness ($T_{\mathrm{Si}}$) of less than 3 nm. Also, $T_{\mathrm{Si}}$ scaling demonstrated to improve short channel effect without penalty to performance down to 3 nm, below which surface roughness scattering degrades transport [28]. The mobility of Si-NSFET with 3 nm-$T_{Si}$ is recorded to 185 $cm^2/Vs$, as shown in Figure 2.10 (c) and (d) [28]. However, one monolayer (ML)-$MoS_2$ film thickness: ~0.6 nm, the mobility of Si with $T_{si} < 1$ nm is less than 10 $cm^2/Vs$, as shown in Figure 1.9 (a). Therefore, in this thesis, the target values of mobility for $MoS_2$ are set to 185 $cm^2/Vs$.

It has been reported that the sulfur vacancy density dependence of the mobility in $MoS_2$ films was analyzed [29]. To achieve the target mobility of 185 $cm^2/Vs$, reducing the sulfur vacancy density of 0.14% is necessary. In addition, the reduction in permittivity in the corresponding direction can be determined by an appropriate Raman shift [30]. The reduction in sulfur vacancies in $MoS_2$ films restores the $E^1_{2\mathrm{g}}$ peak significantly, which may suppress the increase in permittivity along the gate length direction. The reduction in sulfur vacancies causes a decrease in the depletion layer width, as shown in Figure 2.12 (c). The effects of drain-induced tunneling modulation (DITM) in sub-10 nm channels have also been noted in Si-FETs [48], and it is believed that the impact of tunneling current will be even more pronounced in $MoS_2$-FETs with even smaller gate lengths. Therefore, suppressing sulfur defects in the $MoS_2$ film is essential to suppressing the short-channel effect (SCE).

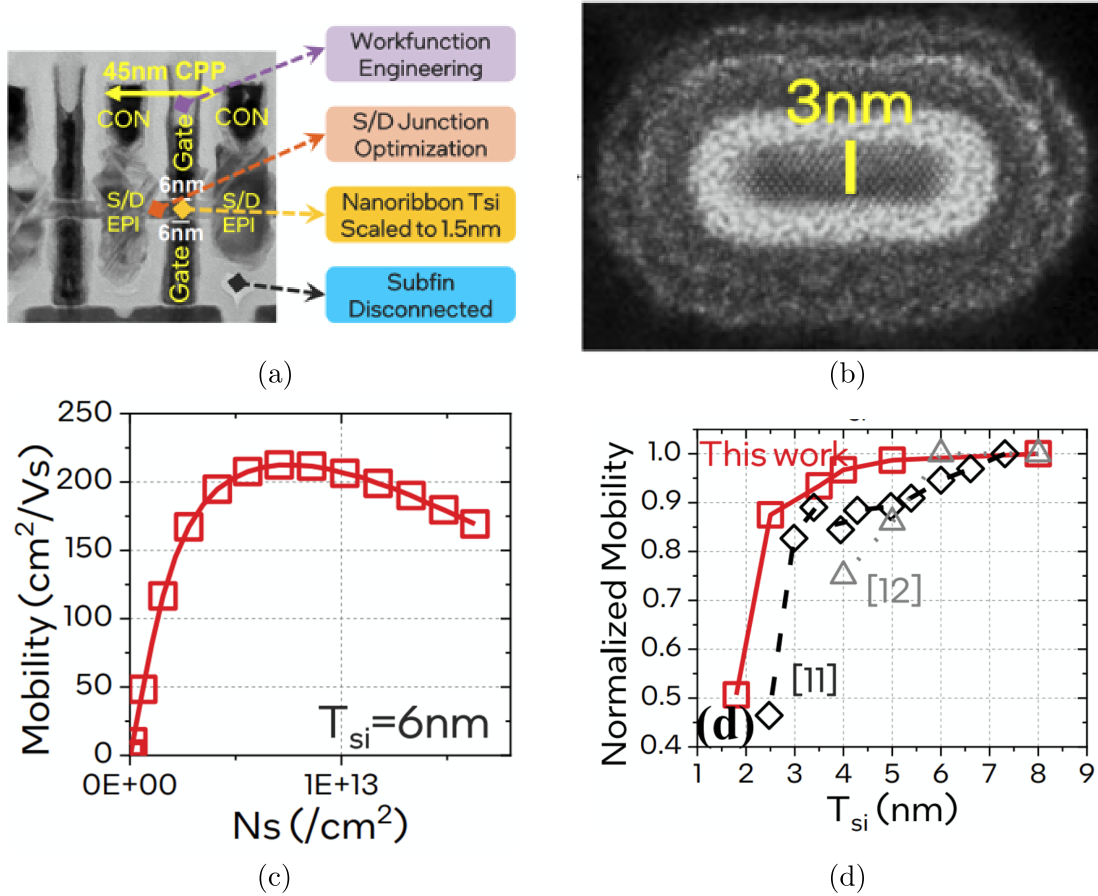


**Figure 2.10**: (a) Cross-sectional TEM image of Si-gate all around (GAA)-nanosheet(NS)-FET [28]. (b) Cross-sectional TEM image of Si channel region in (a). Si channel thickness ($T_{\mathrm{Si}}$) is 3 nm. (c) Mobility of Si-GAA-NS-FET depending on carrier density ($N_{\mathrm{s}}$). Gate length ($L_{\mathrm{g}}$) is 18 nm, and silicon channel thickness ($T_{\mathrm{Si}}$) is 6 nm [28]. (d) Dependence of normalized mobility of Si-GAA-NS-FET on $T_{\mathrm{Si}}$ [28]. Mobility at 3 nm-$T_{\mathrm{Si}}$ is 185 $\mathrm{cm^2/Vs}$.

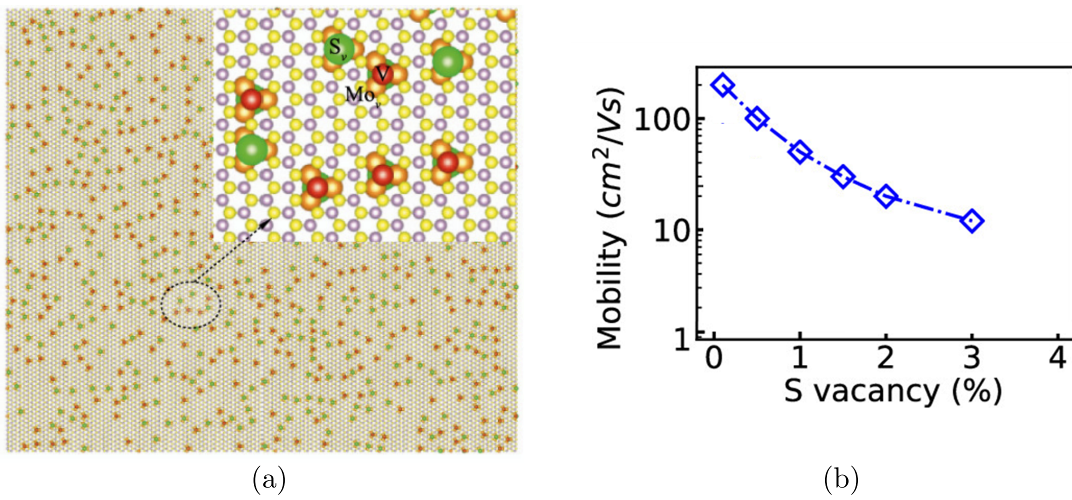


(a) (b)

**Figure 2.11**: (a) Schematic illustration of 1 monolayer (ML)-$MoS_2$ film with 3% sulfur defect density [29]. (b) Electron mobility dependence on sulfur defect density ($V_{\mathrm{s}}$), calculated from (a) [29].

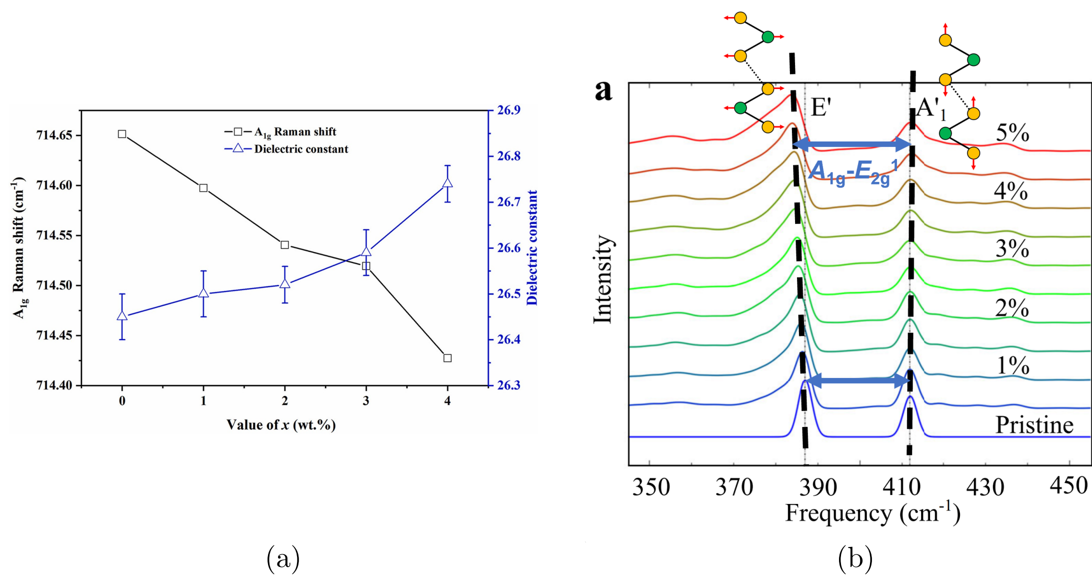


(a) (b)

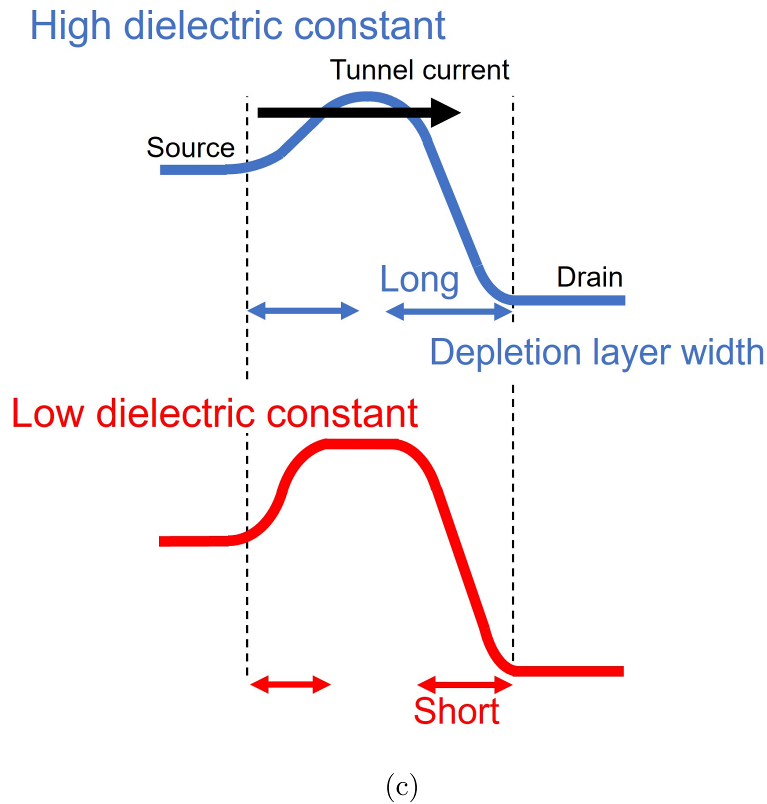


(c)

**Figure 2.12**: (a) Dielectric constant and $A_{1g}$ Raman shift at 714 cm$^{-1}$ of $Li_2ZnTi_3O_8$(LZT)-xwt.%$Nb_2O_5$ (x = 0, 1, 2, 3, 4) ceramics sintered at 1075°C for 4 hours [30]. (b) Raman peak shift depending on amount of sulfur defects ($V_s$) [31]. (c) Influence of short channel effect (SCE) at high dielectric constant of $MoS_2$ film in gate length direction. At low dielectric constant, SCE can be suppressed.

## 2.4 Summary

The target values for the improvement of $MoS_2$ film quality are summarized as follows:

- Deposition temperature:
  - Below 700°C for the front end of line (FEOL).
  - Aiming for even lower temperatures.
  - Below 400°C for the back end of line (BEOL).
- Crystal grain size of $MoS_2$ films:
  - At least 7.9 nm for single crystal size for future active length ($L_{\mathrm{active}}$).
- electron mobility:
  - 185 $cm^2/Vs$ to exceed the mobility of Si-GAA-NS-FET with $T_{\mathrm{Si}} = 3$ nm by reducing the sulfur defect density.
    - Below the sulfur defect density $V_{\mathrm{s}}$ of 0.14% to achieve carrier mobility of 185 $cm^2/Vs$ for single-crystal $MoS_2$ films.

# Chapter 3

# Approach of $MoS_2$ sputtering with large crystal size and low sulfur defect density

In this chapter, to meet the target value set in Chapter 2, the approaches to sputtering deposition will be discussed.

Section 3.1 examines the surface reactions of particles on the substrate and the crystal growth mechanism. It also shows the direction of enhancing the crystal size of $MoS_2$ films. Section 3.2 examines the reactions during the sputtering equipment and the particle flux reaching the substrate. In addition, it considers the sticking coefficient of atoms to the substrate surface. Furthermore, it shows the direction in which the sulfur concentration in $MoS_2$ films is reduced. Section 3.3 summarizes the discussion in this section.

## 3.1 Mechanism of crystal growth on the substrate surface during sputtering

Next, the crystal growth mechanism on the substrate surface is discussed to enhance the crystal size of $MoS_2$ films. Figure 3.1 shows the surface reaction model and nucleation, and nuclear growth mechanism during physical vapor deposition on the substrate. The sputtering method is a physical vapor deposition method, so that the same model can be applied. In particular, during the formation of the $MoS_2$ film, Mo- and S-atom migrate independently on the substrate surface and surface reactions occur. Although nucleation may occur depending on the surface shape of the substrate and the binding energy with the surface particles [77], this phenomenon is not taken into consideration in this study because the substrate is fixed to amorphous $SiO_2$. Therefore, assuming the surface energy is flat, the following reactions occur.

1. Surface diffusion of particles reaching the substrate
2. Formation of the cluster due to collisions between particles during surface diffusion
3. Formation of stable nuclei exceeding critical nuclei due to collisions between clusters and particles (nucleation)
4. Growth of stable nuclei due to the incorporation of diffusing particles (crystal growth)

After that, layer-by-layer $MoS_2$ film formation is assumed to occur through nucleation and crystal growth. It has been reported that new nucleation stops when the diffusion length of particles becomes more significant than the distance between stable nuclei [78]. Therefore, it is clear that an increase in the surface diffusion length of particles is essential for increasing grain size.

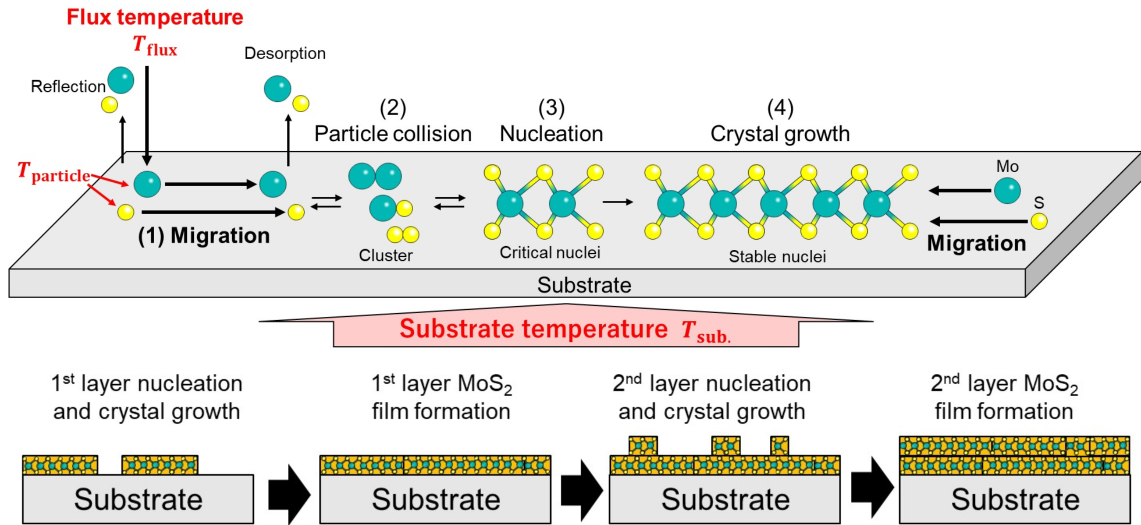


**Figure 3.1**: Surface reaction model and mechanism of nucleation and crystal growth during physical vapor deposition on substrate. Layer-by-layer $MoS_2$ film formation is assumed to proceed through nucleation and crystal growth.

To enlarge the surface migration length of particles on the substrate, There are two approaches, as shown in the below list. One is reducing the number of particles on the substrate surface. The other is enhancing the energy given to particles on the substrate. Furthermore, particle flux represents the number of particles reaching the substrate surface per unit time per unit area, and flux temperature ($T_{\text{flux}}$) represents the energy entering from the plasma gas atmosphere to the substrate surface per unit time per unit area.

- Suppresses the probability of collisions between particles on the surface.
  - Reduces the number of particles on the substrate.
    - Low particle flux
- Enhancing the energy ($T_{\text{particle}}$) imparted to particles on the substrate.
  - $T_{\text{particle}} = T_{\text{sub.}} + T_{\text{flux}}$,
  - where $T_{\text{sub.}}$ is the substrate temperature, and $T_{\text{flux}}$ is the flux temperature.
    - High substrate temperature ($T_{\text{sub.}}$, below 700°C).
    - High flux temperature ($T_{\text{flux}}$).

Therefore, reducing the particle flux, increasing the substrate temperature ($T_{\text{sub.}}$), and enhancing the flux temperature ($T_{\text{flux}}$) are essential for improving the crystal size.

Furthermore, it should be noted that the migration behavior of Mo and S atoms on the substrate is different, as shown in Figure 3.1. Moreover, the surface migration length of

particles on the substrate is given by the following equation [79]:

$$D \approx D_\infty \exp(-U/k_B T), \tag{3.1.1}$$

where $D_\infty$ is migration coefficient, $k_B$ is the Boltzmann constant, and $U$ is the migration barrier energy. In addition, $T$ is the temperature on the substrate, which is the same as the ($T_{particle}$) in this study. It has been reported that the lateral growth of $WS_2$ is mainly limited by W migration with a more significant migration barrier of W-atom than S-atom [79, 80]. Like W atoms, Mo atoms have a heavier mass than S atoms and higher interaction with the $SiO_2$ surface than S atoms; the migration barrier energy of Mo atoms is higher than that of S atoms. Consequently, it is considered that the surface migration length of Mo governs the lateral growth of the final $MoS_2$.

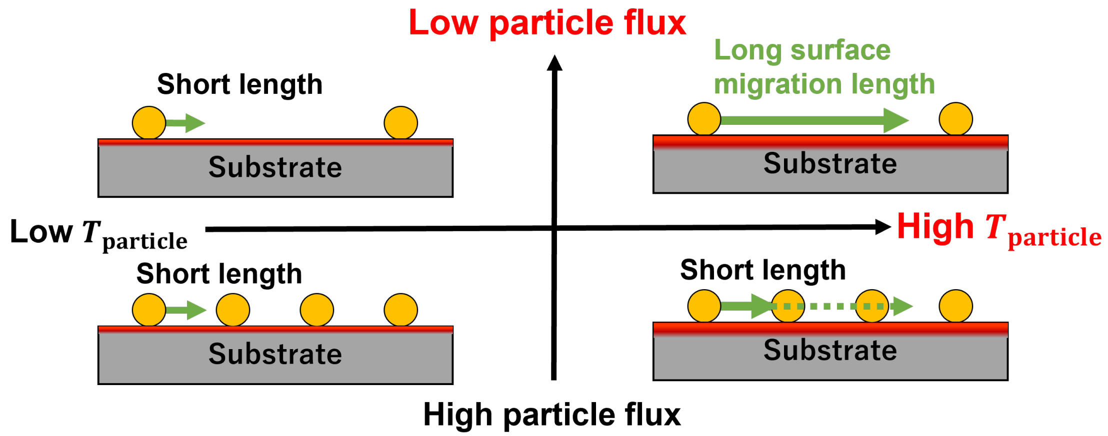


**Figure 3.2**: Approach for achieving long surface migration length of particles on substrate by controlling particle temperature ($T_{particle}$) and particle flux during sputtering deposition on substrate.

## 3.2 Discussion on the particle reaching the substrate surface for low sulfur vacancy density in $MoS_2$ film

### 3.2.1 Particle Species Reaching the Substrate in $MoS_2$ Sputtering

In the sputtering process for $MoS_2$ thin films, various particle species reach the substrate due to multiple interactions within the plasma and with the target. These interactions determine the energy and composition of the particles, which influence the quality of the deposited film. As illustrated in Figure 3.3, the following particle species reach the substrate during sputtering:

- Sputtered particles: Mo, S
- Recoiled particles: Ar atoms from the plasma
- Plasma species: $Ar^+$ ions, electrons from the plasma

Gas scattering in the plasma can reduce the number of Mo and S atoms reaching the substrate, altering the S/Mo ratio at the substrate. The energy loss due to the collisions with Ar gas leads to the thermalization of the sputtered particles, which behaves the same as Ar gas. The energy loss due to scattering and collisions is critical in determining the deposition rate and film properties.

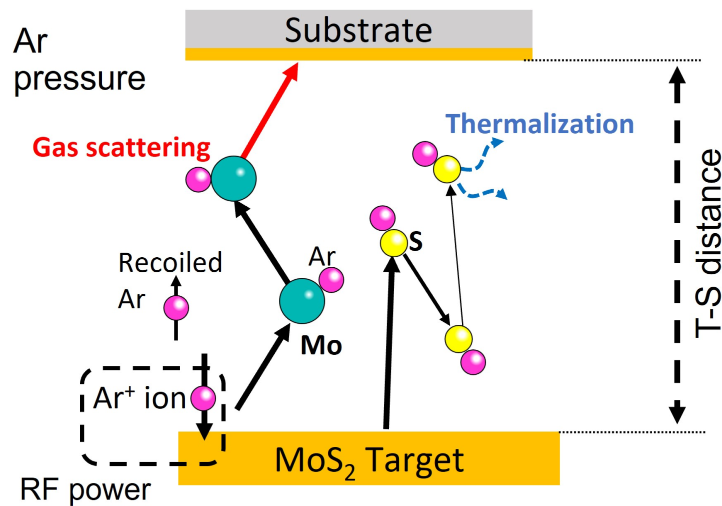


**Figure 3.3**: Schematic of particle species reaching substrate during $MoS_2$ sputtering, including gas scattering and thermalization of sputtered particles in sputtering system [32].

### 3.2.2 Thermalization of sputtered particles and investigation of particle behavior

As the thermalized particles move in all directions while repeatedly colliding with Ar, they adhere to the walls and are expelled, with fewer particles reaching the substrate. The following equation gives the mean free path:

$$\lambda = \frac{k_B T}{\sqrt{2}\pi d^2 p}, \tag{3.2.1}$$

where $\lambda$ represents the mean free path, $k_B$ is the Boltzmann constant, $T$ is the Ar gas temperature, $p$ is the Ar pressure, and $d$ is the effective collision diameter. When the effective collision diameters ($d$) for Ar-Ar, Mo-Ar, and S-Ar are set to 3.4, 3.7, and 3.3 Å, respectively; the mean free paths of thermalized particles in Ar gas are shown in Table 3.1. The results indicate that, although S has a more significant mean free path than Mo, both are significantly smaller than the minimum effective target-substrate distance (168 mm), demonstrating that they are more likely to diffuse within the apparatus. Conversely, high-energy particles move directionally from the target to the substrate, and most particles reach the substrate. For this reason, it is presumed that when the distance over which particles are thermalized is longer than the T-S distance, the supply of particles to the substrate increases. With these things in mind, we will discuss the reactions in the sputtering equipment.

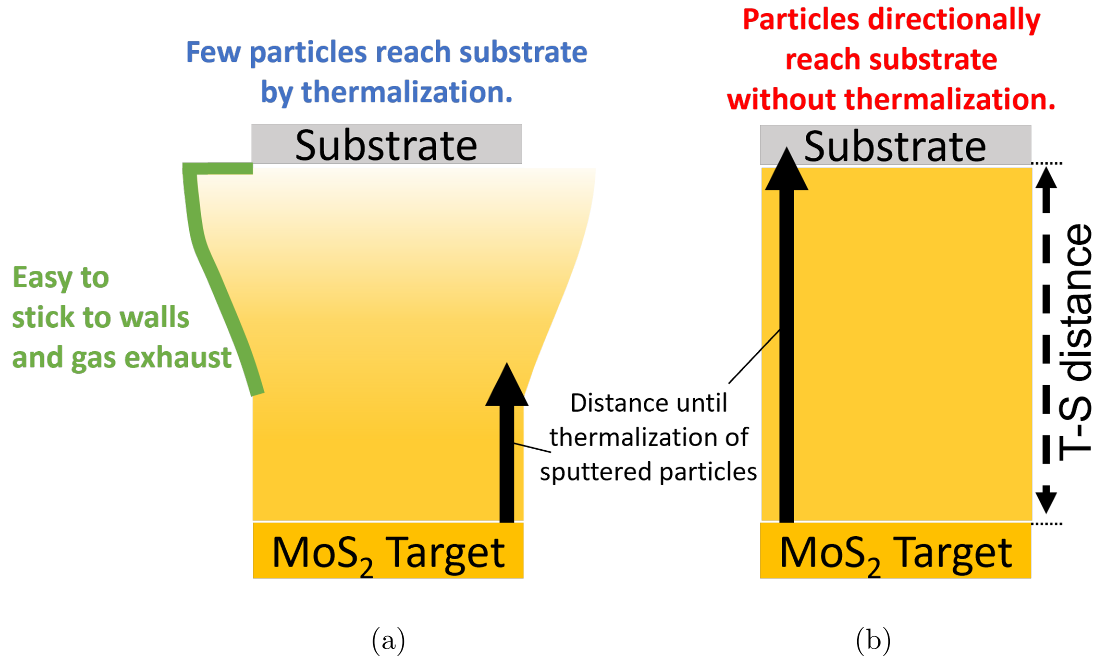


**Figure 3.4**: Model diagram of thermalization distance of sputtered particles and number of particles reaching substrate. (a) Case where thermalization distance is shorter than target-to-substrate (T-S) distance. Sputtered particles are thermalized before reaching substrate, reducing number of particles reaching substrate. (b) Case where thermalization distance is longer than T-S distance. Particles are not thermalized and reach substrate with directionality toward substrate.

**Table 3.1**: Mean free path $\lambda$ for thermalized particles at 0.4 Pa and 0.5 Pa in Ar gas.

| Collision Pair | $\lambda$ at 0.4 Pa (mm) | $\lambda$ at 0.5 Pa (mm) |
|---|---|---|
| Ar–Ar | 20.1 | 16.1 |
| Mo–Ar | 17.0 | 13.6 |
| S–Ar | 21.4 | 17.1 |

The particles reaching the substrate surface are discussed to reduce the sulfur defect density. First, the principle of the sputtering mechanism needs to be considered. Figure 3.5 illustrates the principle of the sputtering apparatus and the potential distribution formed inside the chamber. Radio frequency sputtering refers to using a high-frequency power supply as a power source. The most significant feature is that the compound target with low conductivity, like $MoS_2$, can be used. In the RF discharge, ions are trapped between the electrodes, and electrons reciprocate between the electrodes to ionize and maintain the

plasma discharge. In the case of RF discharge, the DC component does not flow because a blocking capacitor is used. Electrons flowing into the electrode deposit on the electrode surface and become negative electric charges to the plasma. The electrode is negative, the plasma becomes raw, and a voltage is generated. This voltage is called self-bias and becomes a voltage for accelerating Ar ions. The accelerated ions strike the target, and material atoms pop out from the target due to the energy. This series of phenomena is called sputtering. The protruding atoms are transported in the plasma and deposited in atomic form on the substrate to form a thin film. The sputtering process is divided into two steps to analyze the particles reaching the substrate.

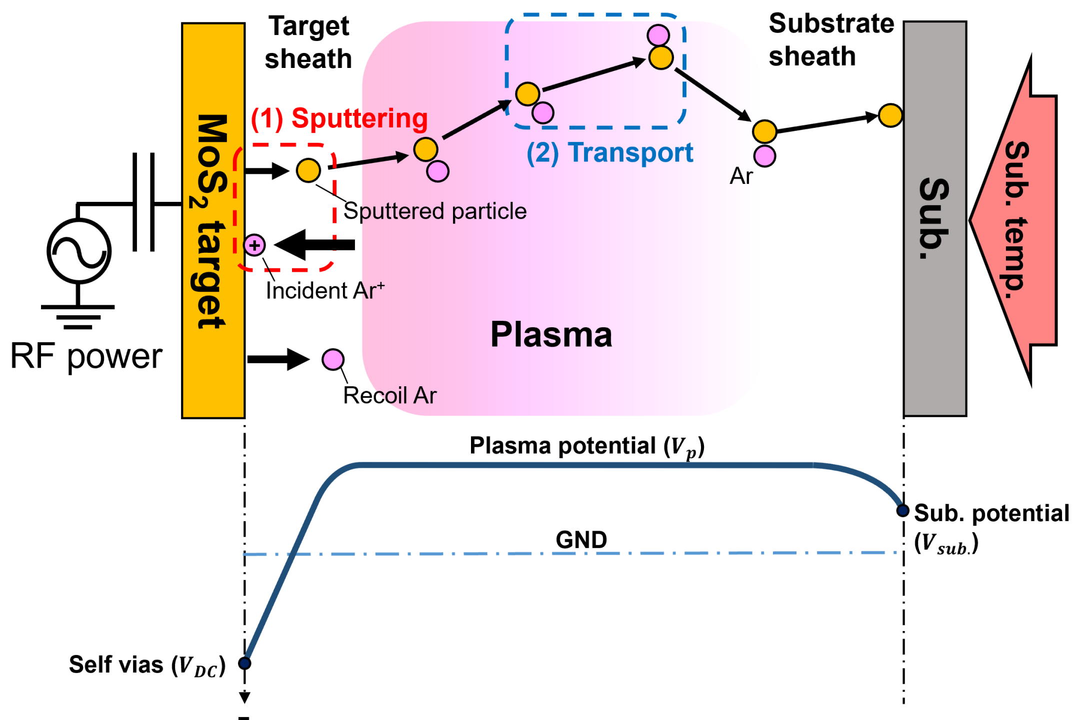


**Figure 3.5**: Principle of RF magnetron sputtering for $MoS_2$ film and potential distribution inside sputtering equipment.

### 3.2.3 Step 1: Sputtering

Argon plasma is generated inside the apparatus. A self-bias $V_{DC}$ voltage is applied to the target surface via the RF power supply. The potential difference between the plasma potential near the target surface and the self-bias, $q(V_p - V_{DC})$, accelerates Ar ions, which collide with the target and eject particles (Mo or S atoms) from its surface. This region is

referred to as the target sheath. Near the substrate, a potential difference exists between the plasma potential $V_{\mathrm{p}}$ and the substrate potential $V_{\mathrm{sub.}}$. This region is referred to as the substrate sheath. The energy distribution of the sputtered particles can be expressed using the Thompson formula [81]:

$$f(E) \propto E \frac{1 - \sqrt{(E_b + E)/\Lambda E_1}}{(E + E_b)^3} \tag{3.2.2}$$

$$\Lambda = 4m_i m_t/(m_i + m_t)^3 \tag{3.2.3}$$

where $E_1$ is the energy of incident $Ar^+$ ions (50–150 eV), $E_b$ is the surface binding energy (4.42 eV), $m_i$ is the mass of incident ions (40.0 u), and $m_t$ is the mass of the target (Mo: 95.9 u, S: 32.1 u). respectively [82]. The average incident energy of $Ar^+$ ions increases with the target sheath:

$$E_1 = q(V_p - V_{\mathrm{DC}}), \tag{3.2.4}$$

where $q$ is an electric charge, $V_p$ is the plasma potential, and $V_{\mathrm{DC}}$ is the bias voltage. Figure 3.6 (a) shows the energy distribution of sputtered Mo-atoms when the incident energy of Ar ions is set to 50, 100, and 150 eV. As observed, the particles exhibit a peak energy of around 3 eV. However, as the incident energy of Ar ions increases, a higher-energy tail becomes more pronounced. Figure 3.6 (b) summarizes the average energies of sputtered particles.

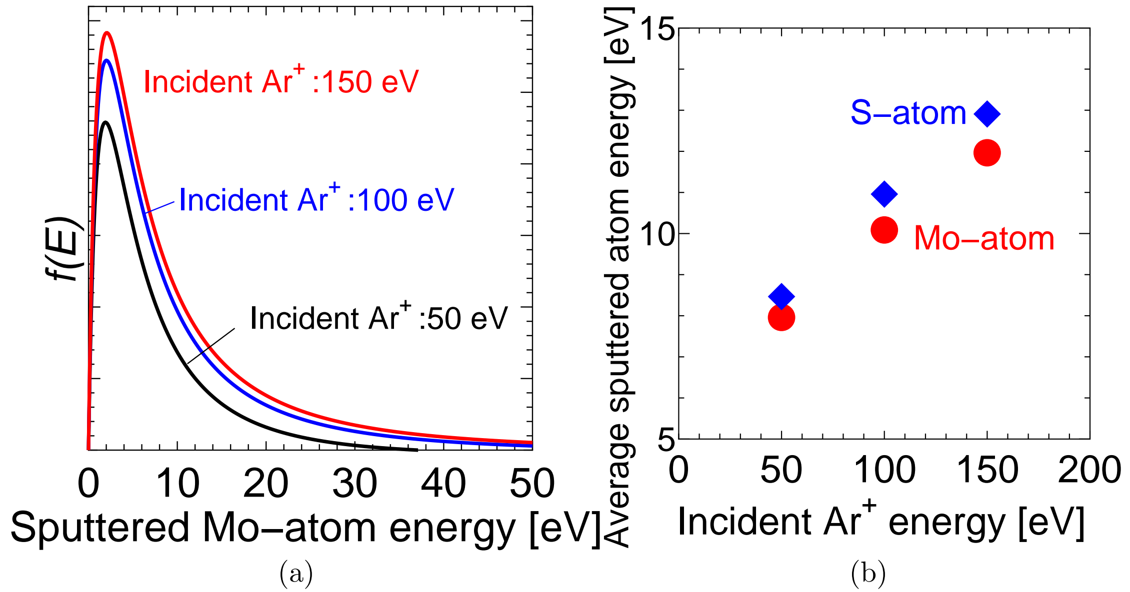


**Figure 3.6**: (a) Energy distribution function of sputtered Mo atoms. (b) Average energy of sputtered atoms from target surface. Ar incident ion energy ($E^{+}_{Ar}$) is varied from 50 to 150 eV.

### 3.2.4 Step 2: Transport

Sputtered particles travel the distance between the target and the substrate while colliding with Ar gas molecules. The energy loss during these collisions varies depending on the material type. When the particle's energy reaches near-zero due to collisions, the particle becomes the gas phase; this phenomenon is referred to as thermalization [83, 84]. To calculate the average transport distance of particles, a simulation software called "Stopping and Range of Ions in Matter (SRIM)" is adopted [85–87]. Although the phenomena occurring during collisions between solids and gases may differ, SRIM calculations have been performed using experimental data on the energy loss during collisions for both solid and gas targets [88, 89]. SRIM calculations have been performed for Ar gas targets with various particles [90], and the error between the calculated and experimental values is about ±5 10%, so the results in this study are considered valid [91].

Figure 3.7 shows the nuclear- and electronic-stopping power of sputtered atoms versus energy near the target surface from SRIM simulation, which indicates that although the original assumption of the SRIM calculation is to calculate the behavior of ion species, the stopping power of electrons is low, and the calculation of the behavior of neutral particles can approximate the behavior of ions, so the calculation results are useful. Figure 3.8 shows the average distance traveled in the Ar atmosphere versus the sputtered atom energy. The simulation parameters were set to an Ar pressure of 0.5 Pa and an Ar gas temperature of 300 K. The incident particles were Mo and S with an energy range of 50-300 eV. The results show that the average transport distance of Mo atoms is longer than that of sulfur atoms. The minimum distance between the sputtering equipment target and the substrate used in this study is 150 mm, but the effective T-S distance (168 mm) is shown by the dashed line in Figure 3.8 because the central axes of the target and the substrate are misaligned by 75 mm. Figure 3.9 also shows the average transport distance of Mo and S atoms when the initial energy is assumed to be the average energy of the sputtered atoms calculated in Figure 3.6(b). Ar pressure is set to 0.5 and 0.4 Pa, respectively. The results show that S-atoms have a smaller transport distance than Mo-atoms and are less likely to reach the substrate. In addition, it was found that sulfur can reach the substrate more efficiently by increasing the energy of the incident $Ar^+$ and by lowering the Ar pressure. Based on the above considerations, we determine that high RF power, low Ar pressure, and short T-S distance are the indicators for reducing the sulfur defect density in $MoS_2$ films to increase the S/Mo flux ratio as much as possible.

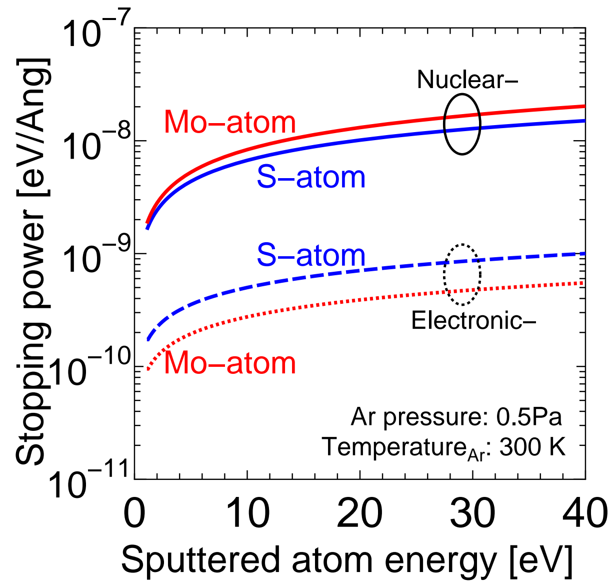


**Figure 3.7**: Nuclear-stopping and electronic-stopping power of sputtered atoms as function of energy calculated using SRIM.

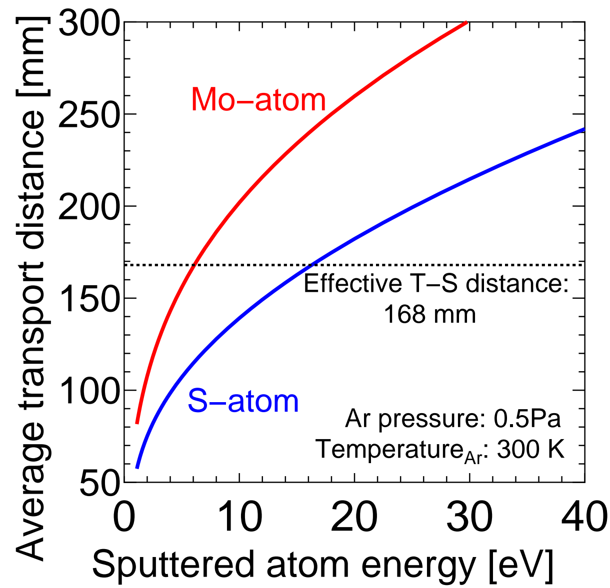


**Figure 3.8**: Average transport distance of sputtered atoms as function of energy near target surface.

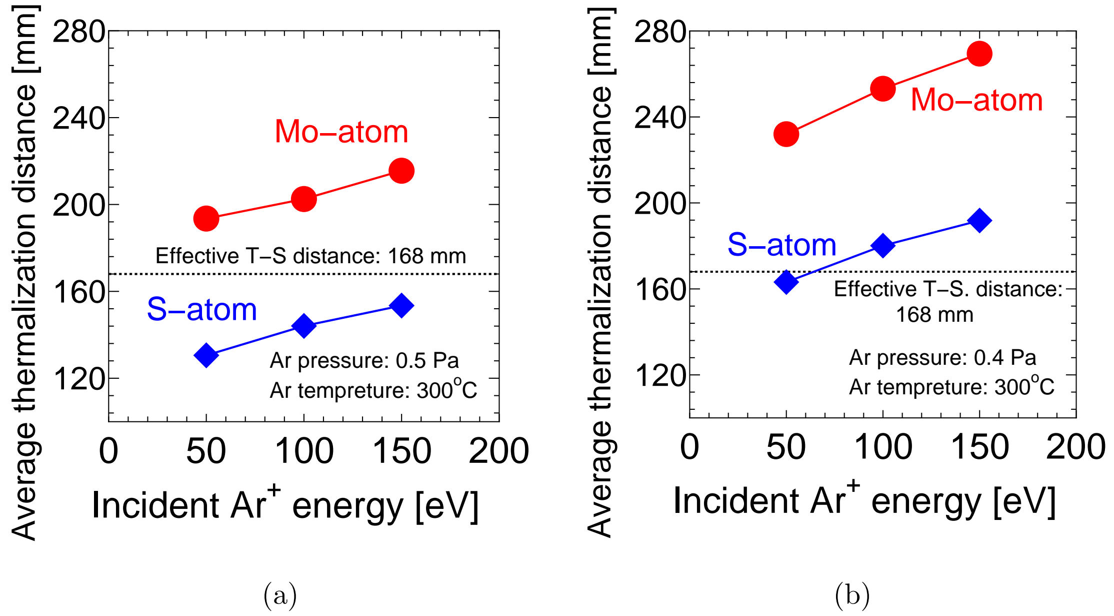


(a)

(b)

**Figure 3.9**: Average thermalization distance of sputtered particles as function of incident $Ar^+$ energy. Ar temperature was set to 300°C, and Ar pressure was set to (a) 0.5 Pa and (b) 0.4 Pa, respectively.

### 3.2.5 Consideration of the sticking coefficient on the number of particles on the substrate surface

In the previous subsection, we discussed the S/Mo flux ratio to the substrate. To determine the final S/Mo ratio in the deposited $MoS_2$ film, it is necessary to consider the sticking coefficients of Mo and S atoms [92]. In the sputtering process, the effective sticking coefficient considers the reflection of particles immediately after colliding with the substrate, as well as long-term processes such as surface migration, thermal desorption, and other time-dependent phenomena, which determine the final amount of particles retained on the substrate [92, 93]. Additionally, since the sticking coefficient evaluates retention, including particle detachment due to thermal desorption, which becomes significant at high substrate temperatures, as well as re-sputtering on the surface, it provides a value that more closely reflects the actual film deposition efficiency. Therefore, the sticking coefficient is a crucial parameter in modeling compound growth, as a higher sulfur sticking coefficient increases the fraction of sulfur particles that remain on the surface upon collision, leading to an increased S/Mo ratio. In this subsection, the discussion focuses on three factors influencing the sticking coefficient: re-sputtering, reflection, and desorption.

Some Ar ions accelerate toward the target and reach the substrate as recoiled Ar. These particles collide with the growing film with considerable energy, potentially causing re-sputtering. Naturally, Re-sputtering reduces the effective sticking coefficient [92]. Since the effects, such as deposition rate reduction at low Ar pressure, which will be discussed

in later chapters, have not been observed, this study assumes that the influence of re-sputtering is negligible.

Sputtered particles with smaller masses are more likely to be reflected by the substrate, which may reduce the sulfur content on the substrate. On the other hand, it has been reported that the reflection coefficient of sputtered particles is nearly zero for low-energy particles ($E < 25$ eV) [92, 94]. The reflection coefficient becomes non-negligible only for high-energy particles ($E > 25$ eV) that strike the surface at large angles. Under the sputtering parameters used in this study, as shown in Figure 3.9, Mo and S atoms reaching the substrate have energies below 25 eV, and no Mo or S particles possess large incident angles and high energy. Thus, the reflection process can be excluded.

Finally, the desorption rate ($R$) of an atom adsorbed on the surface at temperature $T$ is expressed by following equation [95, 96]:

$$R = \nu \exp(-E_{\mathrm{des.}}/k_{\mathrm{B}}T), \tag{3.2.5}$$

where $\nu$ is the frequency of vibration of an adsorbed molecule perpendicular to the surface, $k_{\mathrm{B}}$ is the Boltzmann constant, and $E_{\mathrm{des.}}$ is the activation energy for desorption. $T$ is the temperature on the substrate, which is the same as the ($T_{\mathrm{particle}}$) in this study. $R$ represents the rate at which particles already residing on the surface escape back into the gas phase, such as thermal energy. Desorption becomes more likely when the substrate temperature is high or when a surface binding is weak. As shown in Table 3.2, the activation energy for desorption is lower for S than for Mo, resulting in a higher desorption rate of sulfur at elevated $T_{\mathrm{particle}}$. In Chapter 4, the substrate temperature ($T_{\mathrm{sub.}}$) dependence is discussed to the possible influence of desorption on the sticking probability. On the other hand, as mentioned in Chapter 5, an increase in flux temperature ($T_{\mathrm{flux}}$) leads to an increase in the S/Mo ratio, which contradicts this assumption. This contradiction is attributed to the significant variation in the supply ratio of S and Mo particles to the substrate due to fluctuations in $T_{\mathrm{flux}}$ in this study, beyond the difference in sticking probability between S and Mo, As a result, the $MoS_2$ film quality has likely been altered.

Considering these aspects, the discussion will proceed in the following chapters.

**Table 3.2**: Activation energy for desorption of Mo and S atoms from various sources.

| Desorption Source | Desorbing Atom | Activation energy for desorption [eV] |
|---|---|---|
| Mo metal | Mo | 6.8 [97] |
| Solid S | S | 2.6 [97] |
| Si surface | Mo | 5.63* |
| | S | 5.32* |
| $MoS_2$ film | Mo | 4.9~7.0** |
| | S | 1.5~2.7** |

*Surface binding energy from silicon is listed, respectively [82].
**Formation energy of Mo and S vacancies from bulk $MoS_2$ is listed, respectively [98].
Since the surface binding energy and defect formation energy are relatively small, the desorption activation energy ($E_{des.}$) for S is expected to be lower than that for Mo.

## 3.3 Summary

Below is a summary of this chapter. It summarizes approaches to improving film quality. It also indicates which chapter discusses each approach.

- Objective
  - Investigation of sputtering growth directions for increasing crystal size and reducing sulfur defect density in $MoS_2$ films.
- Approaches
  - Enhancing crystal size in $MoS_2$ film: increasing particle surface diffusion on the substrate
    - Appropriate substrate temperature ($T_{sub.}$): Verify in Ch. 4.
    - Optimal flux temperature ($T_{flux}$): Verify in Ch. 5 and Ch. 6.
    - Low particle flux: Verify in Ch. 6.
  - Reducing sulfur defect density in $MoS_2$ film: increasing the S/Mo supply ratio during sputtering
    - Low $T_{sub.}$ to suppress sulfur desorption: Verify in Ch. 4.
    - High RF power: Verify in Ch. 5.
    - Low Ar pressure: Optimize for 0.4 Pa.
    - Short T-S distance: Set to the minimum value.

# Chapter 4

# Dependence of $MoS_2$ film quality varying substrate temperature during sputtering

## 4.1 Background

In this chapter, enhancing substrate temperature ($T_{\text{sub.}}$) is used to extend the surface migration length of particles on the substrate, as shown in Figure 4.1. On the other hand, in a previous study, at vacuum annealing temperatures above 200°C, sulfur vacancies ($V_{\text{s}}$) are observed in bulk $MoS_2$ films [33]. This phenomenon is evidenced by the appearance of sulfur-deficient peaks in the XPS spectra, as shown in Figure 4.2. Furthermore, Table 4.1 shows the relationship between vacuum temperature and the sulfur-to-molybdenum (S/Mo) ratio, indicating a progressive reduction in the S/Mo ratio with increasing annealing temperature. Therefore, sulfur may be desorbed during cooling immediately after deposition, forming these defects in sputtering under high-temperature conditions. The time evolution of $T_{\text{sub.}}$ is shown in Figure 4.3, where two phases are evident: the sputtering phase ($t_{\text{sputter}}$) and the natural cooling phase ($t_{\text{cool}}$). During sputtering $T_{\text{sub.}}$, sulfur loss is unlikely to occur in high sulfur flux depositions. However, at the start of natural cooling ($t_{\text{cool}}$), sulfur vacancies ($V_{\text{s}}$) may form in the film due to the no sulfur supply with high substrate temperatures, which degrades the crystal quality of the $MoS_2$ films. Moreover, the sulfur desorption due to high $T_{\text{sub.}}$ during sputtering may be a possible reason, as discussed in Subsection 3.2.2. Therefore, the $MoS_2$ film quality varying the substrate temperature ($T_{\text{sub.}}$) is investigated in this chapter. Furthermore, annealing in a sulfur vapor atmosphere (S-annealing) was performed to compensate for sulfur defects in the $MoS_2$ film [20], and the relationship between the film qualities after sputtering and S-annealing were evaluated.

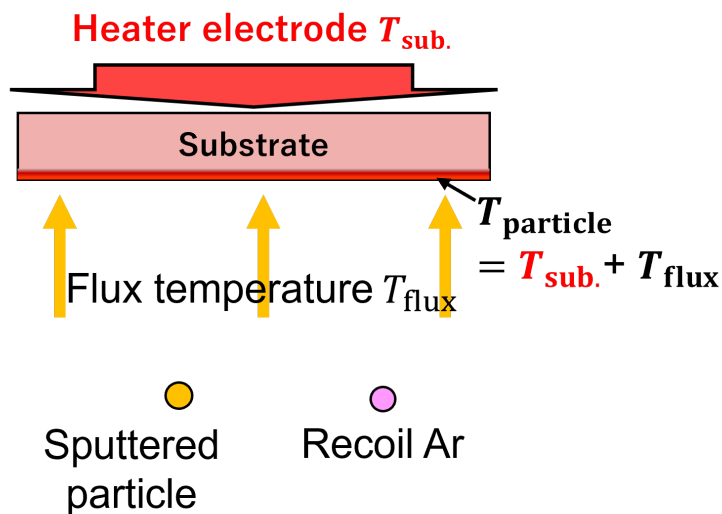


**Figure 4.1**: Approach to enhance surface migration length by high substrate temperature ($T_{sub.}$).

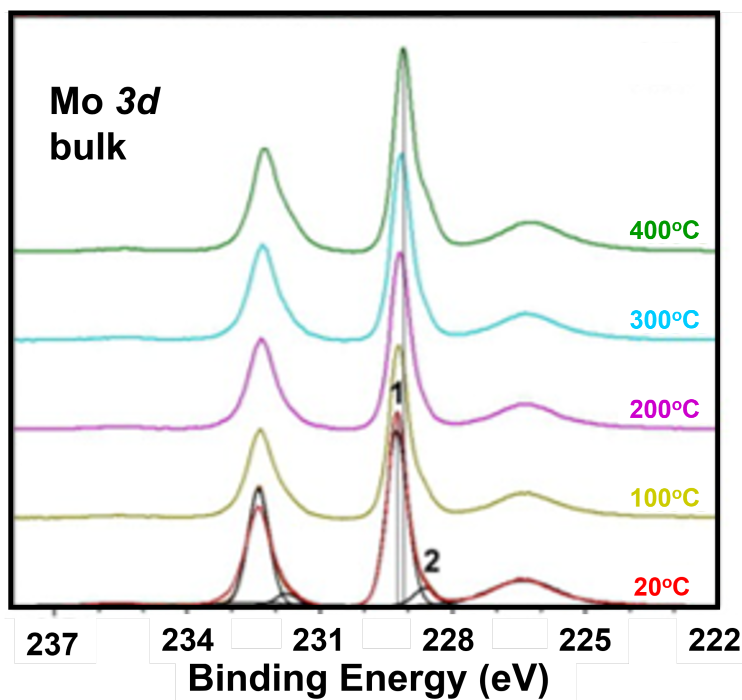


**Figure 4.2**: XPS peaks of bulk $MoS_2$ with ultra-high-vacuum annealing [33].

**Table 4.1**: S/Mo ratio in bulk $MoS_2$ under different vacuum annealing temperatures [33].

| **Annealing temperature [°C]** | **S/Mo Ratio** |
|---|---|
| 20 | 2.0 |
| 100 | 2.0 |
| 200 | 1.95 |
| 300 | 1.90 |

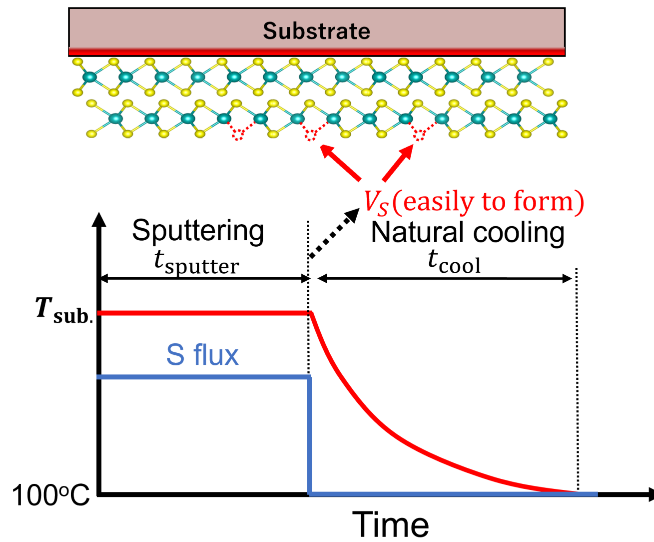


**Figure 4.3**: Changes in substrate temperature over time during sputtering ($t_{\text{sputter}}$) and natural cooling ($t_{\text{cool}}$) of $MoS_2$ film. At high substrate temperatures during natural cooling ($t_{\text{cool}}$), sulfur defects ($V_{\text{s}}$) are more easily formed in $MoS_2$ film.

## 4.2 Experimental methods

Before the formation of the $MoS_2$ film, a sulfuric acid hydrogen peroxide mixture (SPM) ($4:1 = H_2SO_4 : H_2O_2$) was applied at 180°C for 40 min, to remove the metal particles and organic substances on the $SiO_2$/n-Si substrate. Then, a 5-monolayer (ML) assumed $MoS_2$ films were formed by the RF magnetron sputtering with a 4N-$MoS_2$ compound target, as shown in Figure 4.4 (a). To prepare various $MoS_2$ films, the sputtering conditions were controlled at the substrate temperatures between 200 and 500°C under Ar pressure of 0.55 Pa with Ar flow rate of 7 sccm and a target-substrate distance of 150 mm. It is noted that the duration time of the high substrate temperatures just after sputtering is for about 20 seconds, and then the temperature gradually decreases under the vacuum. Figure 4.4 (b) shows a sulfur vapor annealing apparatus used for sulfur compensation of the sputtered $MoS_2$ film. The sulfur powder was placed at zone 1 and was heated at 250°C for 40 min, and the samples were placed at zone 2 heated at 700°C for 40 min. The Raman spectroscopy analyzed the $MoS_2$ films and also the full width at half maximum (FWHM) values and shift values of the $E^1_{2g}$ and $A_{1g}$ peaks were extracted. X-ray photoelectron spectroscopy (XPS) with an Al $K_\alpha$ X-ray source, X-ray diffraction (XRD) measurement, and scanning transmission electron microscopy (STEM) were also performed for structural characterization.

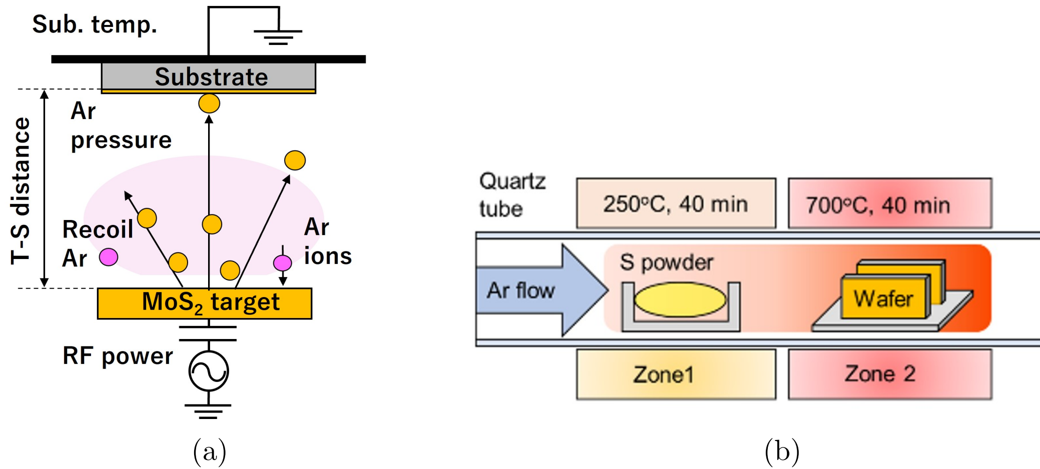


**Figure 4.4**: Schematic of (a) sputtering and (b) sulfur-vapor annealing (S-annealing) systems.

## 4.3 Results and discussion

### 4.3.1 Comparing the $MoS_2$ film quality after sputtering and S-annealing

Since the $MoS_2$ film deposited by sputtering has sulfur vacancies the S-annealing process is necessary to compensate for these vacancies. Therefore, the $MoS_2$ film quality after sputtering and S-annealing was evaluated. To evaluate the composition ratio of the $MoS_2$ films, Figure 4.5 shows the (a) Mo 3*d* and (b) S 2*p* orbits of the XPS spectra after sputtering at an RF power of 40 W under substrate temperature ($T_{\mathrm{sub.}}$) of 300°C and after S-annealing. The almost Mo 3*d* peaks consist of Mo-S and Mo-Mo bonds, and the S 2*p* peaks consist of S-Mo and S-S bonds. The S/Mo composition ratios were obtained according to the equation,

$$\frac{\mathrm{S}}{\mathrm{Mo}} = \frac{Area_{\mathrm{S}\ 2p}/\mathrm{RSF}_{\mathrm{S}\ 2p}}{Area_{\mathrm{Mo}\ 3d}/\mathrm{RSF}_{\mathrm{Mo}\ 3d}}, \tag{4.3.1}$$

where the relative sensitivity factors (RSFs) are 0.717 and 3.54, respectively. The S/Mo composition ratio increases from 1.58 to 1.86 because of the compensation of sulfur vacancies by S-annealing. In addition, shifts in the binding energy peaks of Mo3*d* and S 2p toward the negative direction were observed after S-annealing. This low energy shift suggests that the Fermi level approaches the valence band maximum (i.e., decreased n-type behavior) [99–101].

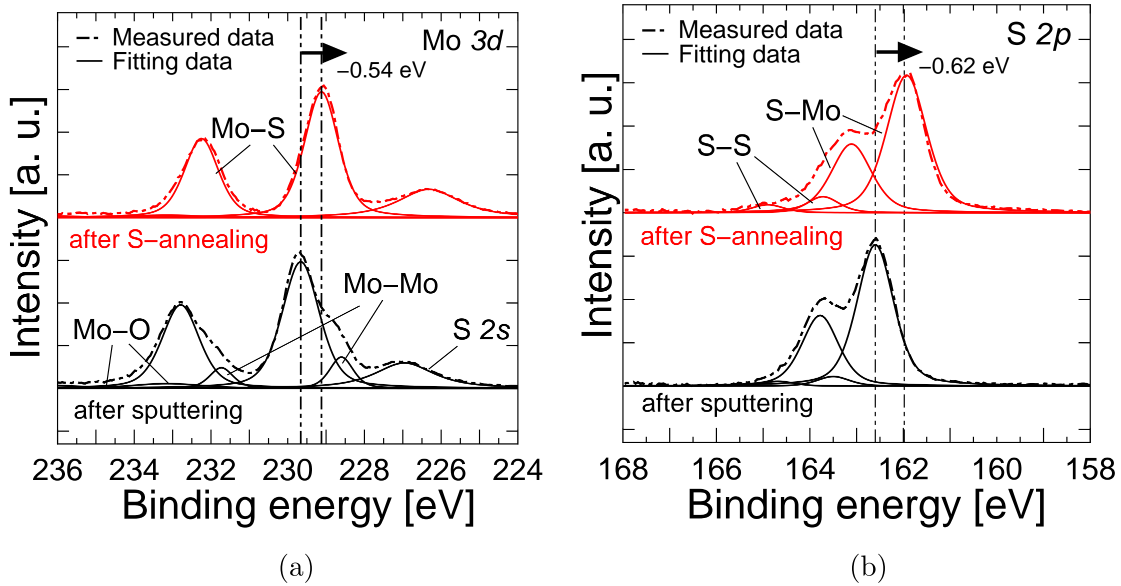


**Figure 4.5**: XPS spectra corresponding to (b) Mo 3*d* and (c) S 2*p* orbitals of $MoS_2$ films after sputtering and S-annealing. 2.5-nm $MoS_2$ films were deposited at 300°C using RF power of 40 W. Dotted and solid lines represent measured and fitted spectra, respectively.

Figure 6.5 shows the Raman spectra of the $MoS_2$ films after sputtering and S-annealing, respectively. S-annealing enhances the intensities of the $A_{1g}$ and $E^1_{2g}$ peaks derived from the longitudinal and lateral vibration modes, respectively, of $MoS_2$ film. These results confirm that the effect of sulfur compensation improves the crystallinity of the $MoS_2$ films.

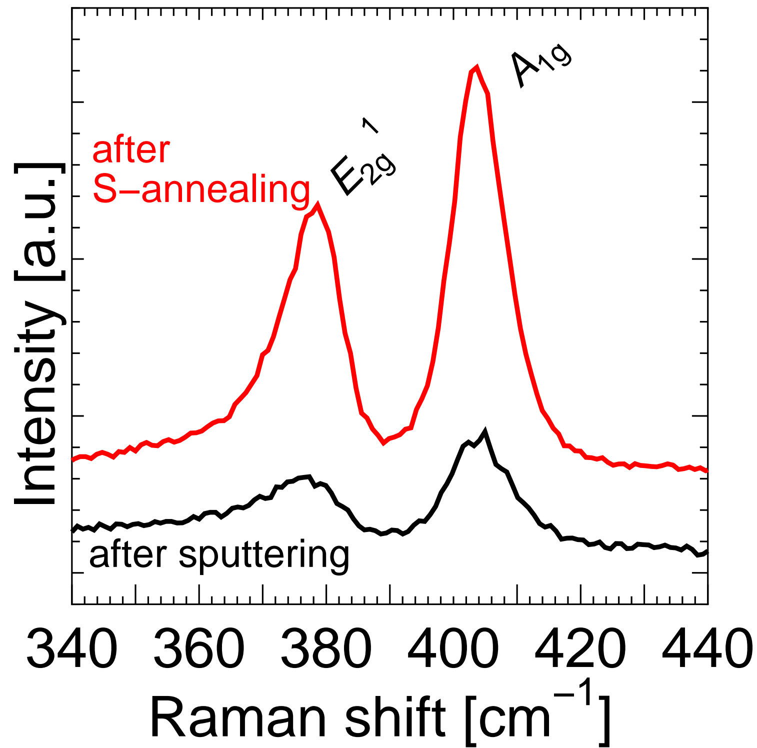


**Figure 4.6**: Raman spectra of $MoS_2$ films after sputtering and S-annealing. 2.5-nm-$MoS_2$ films were deposited at 300°C using RF power of 40 W.

In order to further confirm the $MoS_2$ film crystallinity before and after S-annealing, we measured out-of-plane $2\theta$-$\theta$ X-ray diffraction (XRD) patterns. Figure 4.7 shows the XRD pattern around the silicon (002) peaks in both samples, where those patterns were normalized by the intensity of silicon (004) peaks. The $MoS_2$ (002) peaks were clearly observed. Compared with the intensity of $MoS_2$ (002) peaks for the as-sputtered film, the S-annealed film took a more significant value. Therefore, it is confirmed that the crystallinity of $MoS_2$ film is improved after S-annealing.

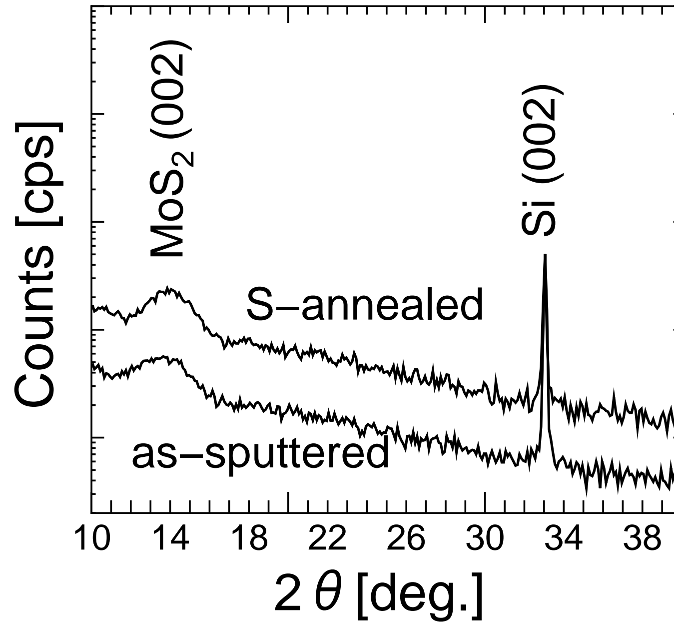


**Figure 4.7**: XRD patterns of as-sputtered and S-annealed $MoS_2$ films, which were sputtered at 40 W under Ar pressure of 0.55 Pa at 300°C. Signal intensities were normalized by intensity of silicon (004) peak.

To evaluate the variation in the in-plane orientation, we measured automated crystal orientation and phase mapping in transmission electron microscopy (ACOM-TEM) using precession-assisted diffraction spot recognition [102, 103]. The structure and pole figure map of the measured sample are shown in Figures 4.8 (a) and (b), respectively. It was confirmed that the $MoS_2$ (100) and (110) planes were randomly distributed in the in-plane (TD and RD) directions.

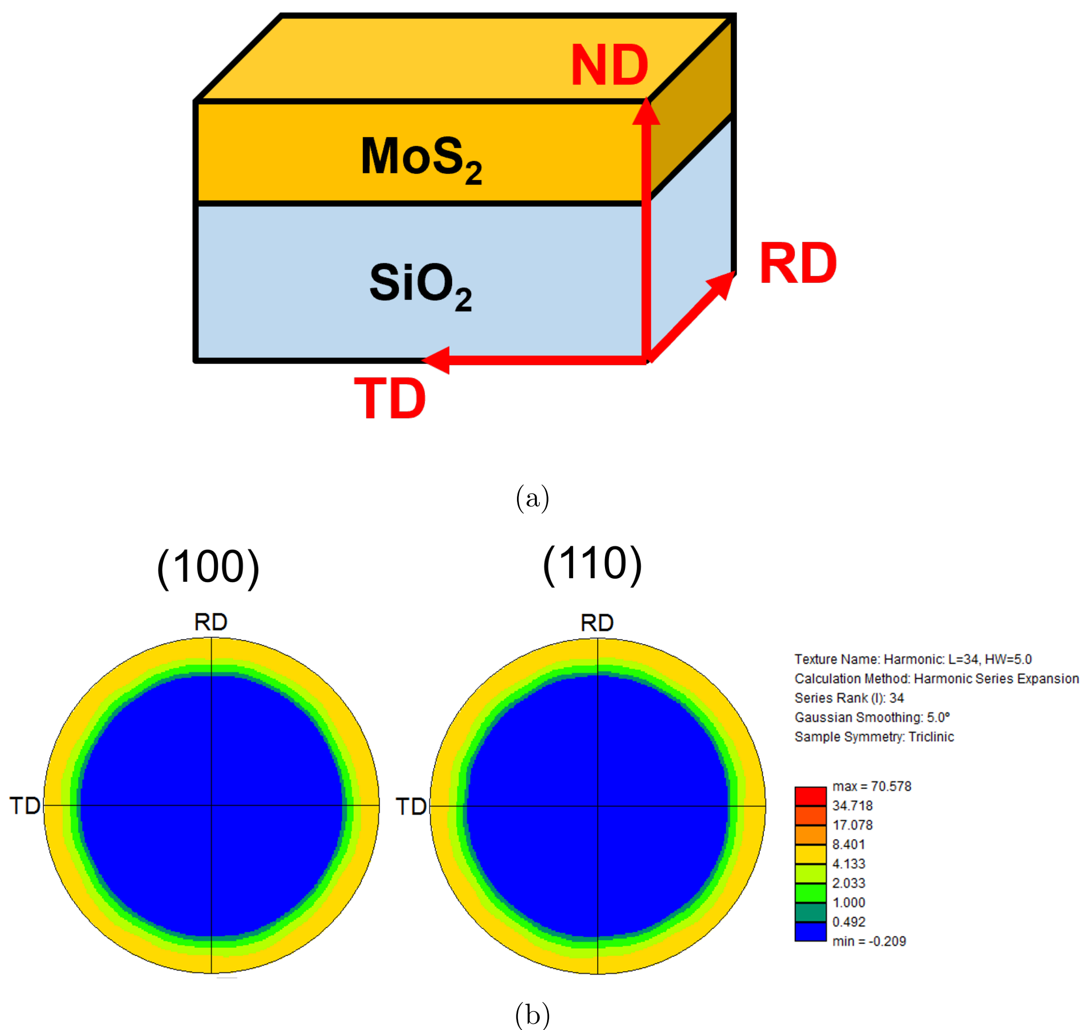


**Figure 4.8**: (a) Structure of the $MoS_2$ sample for automated crystal orientation and phase mapping in transmission electron microscopy (ACOM-TEM). TD, RD, and ND correspond to transverse, rolling, and normal directions. (b) Pole figure maps for $MoS_2$ (100) and (110) planes.

To precisely confirm the $MoS_2$ film crystallinity formed by sputtering and S-annealing, STEM images in the HAADF (high-angle annular dark-field) and ABF (annular bright-field) modes were obtained, as shown in Figures 4.9 (a) and (b). It is found that the multi-layered $MoS_2$ film was formed by the two-step processes consisting of compound sputtering using the $MoS_2$ target and sulfur annealing.

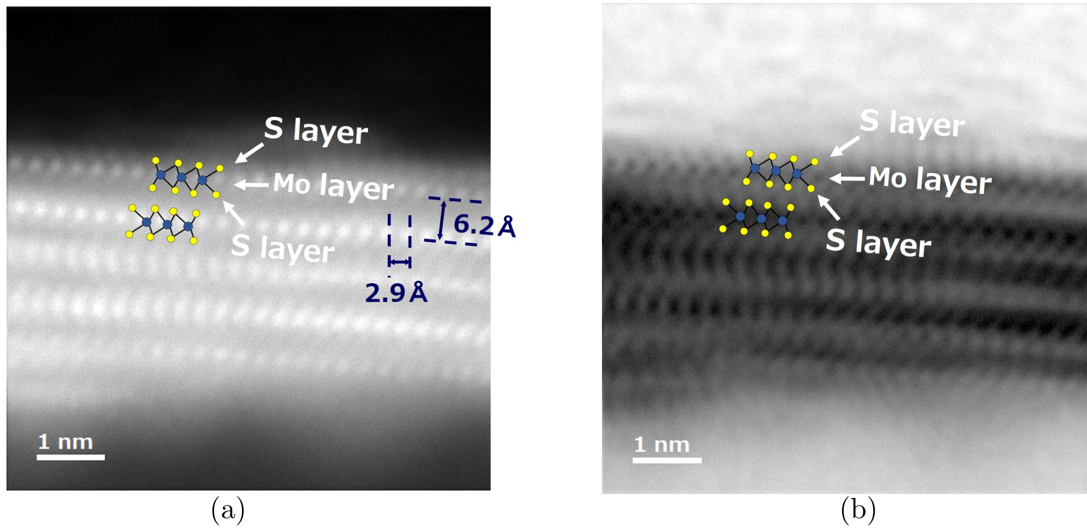


(a) (b)

**Figure 4.9**: Cross-sectional STEM images in (a) HAADF and (b) ABF modes for sputtered $MoS_2$ film obtained with RF power of 40 W at 300°C following sulfur annealing.

To evaluate the crystal structure of the $MoS_2$ film formed by sputtering, plan-view transmission electron microscopy (TEM) observations were conducted. To prevent damage to the $MoS_2$ film during the TEM specimen preparation, a TEM grid with a 20-nm-thick $SiO_x$ membrane was used. In addition, a single-layer $MoS_2$ film was sputtered directly onto the TEM grid to prevent the observation of moiré patterns in the $MoS_2$ film [104], and TEM observations were subsequently conducted in Figure 4.10 (a). Crystal structures were obtained by high-angle annular dark-field scanning TEM (HAADF-STEM). The acceleration of the electron beam was set to 80 kV for the HAADF-STEM. 1ML-$MoS_2$ films were directly deposited on the TEM grid consisting of a 20 nm-$SiO_x$ membrane. The reciprocal lattice pattern of $MoS_2$ single crystals is confirmed, as shown in Figure 4.10 (b). It is observed that $MoS_2$ films are formed on the amorphous $SiO_x$. The reciprocal lattice pattern of $MoS_2$ single crystals is confirmed, as shown in Figure 4.10 (b). It is observed that $MoS_2$ films are formed on the amorphous SiOx. Figures 4.11 show the low-magnification STEM images of 1 monolayer (ML)-$MoS_2$ films after (a) sputtering and (b) S-annealing. Microcrystals were observed in the $MoS_2$ film immediately after sputtering. In addition, it was also confirmed that S-annealing caused the microcrystals to disappear and the grain size of the $MoS_2$ film to increase. Additionally, the reciprocal lattice points of the FFT

after S-annealing is clearly observed. Therefore, the recovery of crystallinity by S-annealing is confirmed. Consequently, it is considered that the microcrystals are incorporated into each other or into the large $MoS_2$ crystallites after S-annealing, which enhances the grain size.

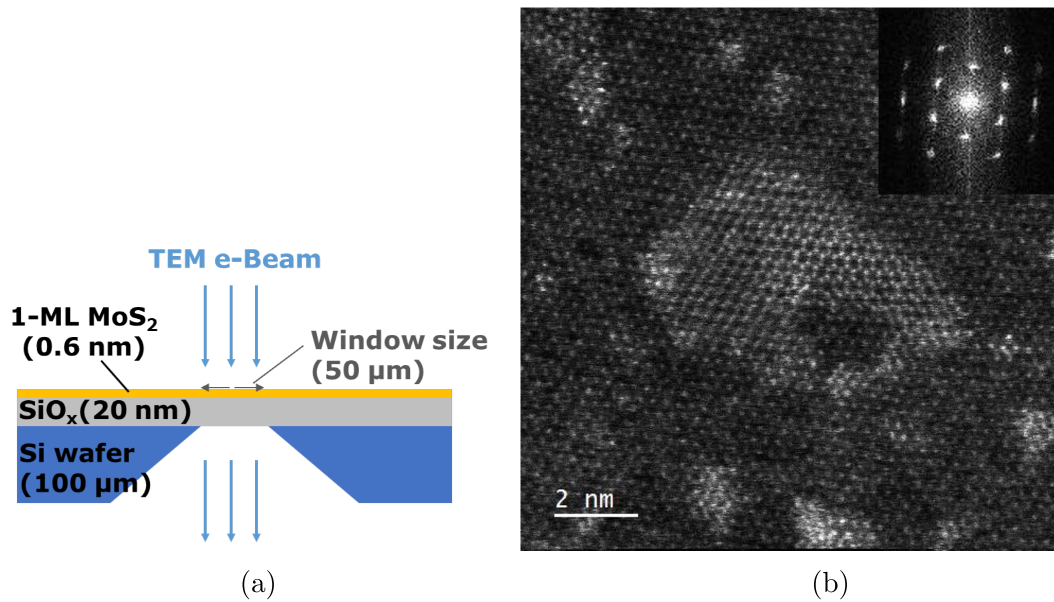


**Figure 4.10**: (a) Schematic of TEM observation structure for $MoS_2$ film. (b) STEM image of 1 monolayer (ML)-$MoS_2$ film after S-annealing.

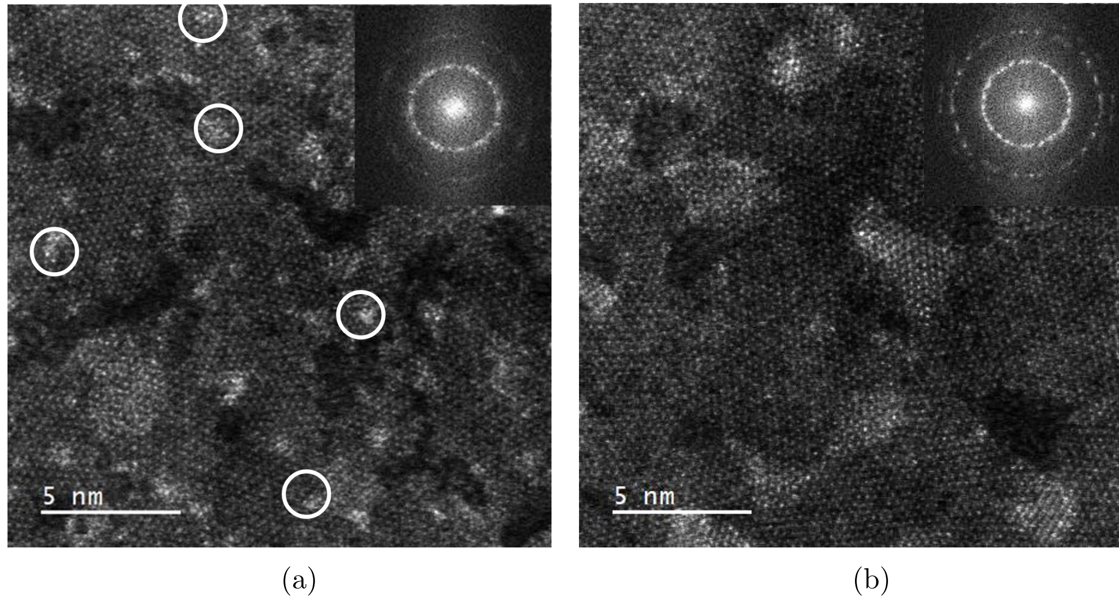


(a) (b)

**Figure 4.11**: STEM images of 1 monolayer (ML)-$MoS_2$ films after (a) sputtering and (b) S-annealing. 1ML-$MoS_2$ film was sputtered directly onto TEM grid that consisted of 20-nm-$SiO_x$ membrane. $MoS_2$ microcrystallites are observed in white circles.

### 4.3.2 Discussion of S-annealing effect for $MoS_2$ film deposited by sputtering

Based on the results obtained, the effect of S-annealing was examined. Figure 4.12 shows the variation of edge formation energy in $MoS_2$ film. It indicated that the Zigzag-Mo edge is easily formed in the S-poor atmosphere with low chemical potential. On the other hand, the Zigzag-S and the Antenna-S edge are formed in the S-rich atmosphere. Figure 4.13 shows the effects of S-annealing. S-annealing is speculated to have two main effects. One is the filling of sulfur vacancies (Vs) with sulfur-atom, and the other is an increase in crystallite size. Figure 4.12 shows that S-annealing binds S to the Mo edge of $MoS_2$. Furthermore, the STEM results suggest that S-annealing has the effect of incorporating microcrystals into each other or large $MoS_2$ crystallites and that the movement of microcrystals forms new $MoS_2$ crystallites.

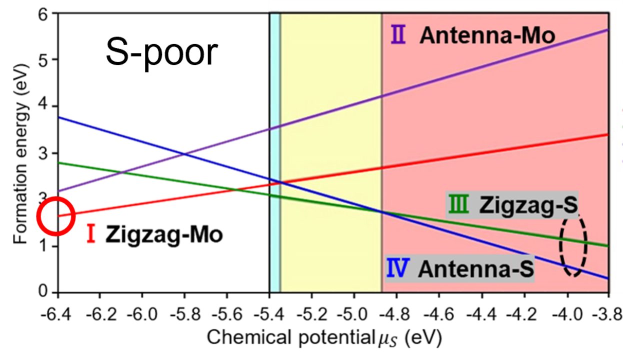


**Figure 4.12**: Variation of edge formation energy in $MoS_2$ film as function of chemical potential of sulfur ($\mu_S$) for triangular nanoflakes with different edge configurations [34].

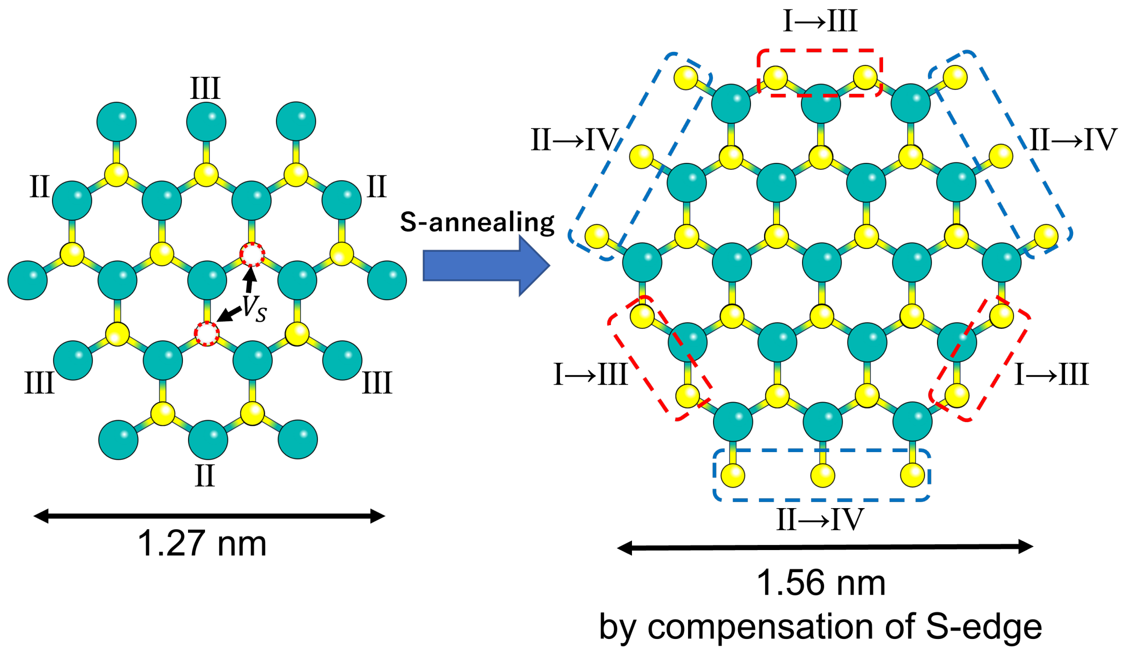


**Figure 4.13**: Model of S-annealing effect in $MoS_2$ film. I, Ⅱ, Ⅲ, and Ⅳ are Zigzag-Mo, Antenna-Mo, Zigzag-S, and Antenna-S edge structures in $MoS_2$ film.

### 4.3.3 $MoS_2$ film quality after sputtering and S-annealing depending on substrate temperature ($T_{sub.}$)

Figure 4.14 shows the dependence of the FWHM values on the substrate temperature ($T_{sub.}$) during sputtering. FWHM is used to evaluate the crystallinity of $MoS_2$ films, speculated to indicate the crystallinity of film quality, including sulfur defect density and crystal size. For the as-sputtered $MoS_2$ film below 300°C, the $MoS_2$ crystallinity was improved with an increase in the substrate temperature. However, the crystallinity of the as-sputtered $MoS_2$ film was degraded at temperatures higher than 300°C. It is speculated that the surface migration length on the substrate of particles decreased at lower substrate temperatures ($T_{sub.}$) during the sputtering, leading to the degradation in the $MoS_2$ film crystal size. On the other hand, at temperatures higher than 300°C, the $MoS_2$ film crystallinity was also degraded due to an increase in sulfur desorption [33]. For the sulfur-annealed $MoS_2$ films, a similar trend was also observed below 300°C. At the $T_{sub.}$ higher than 300°C, the FWHM values of sulfur-annealed film increase with an increase in the sputtering temperature, which is more severe than as-sputtered film. Therefore, it is concerned that sulfur desorption influences the recovery of $MoS_2$ film after S-annealing.

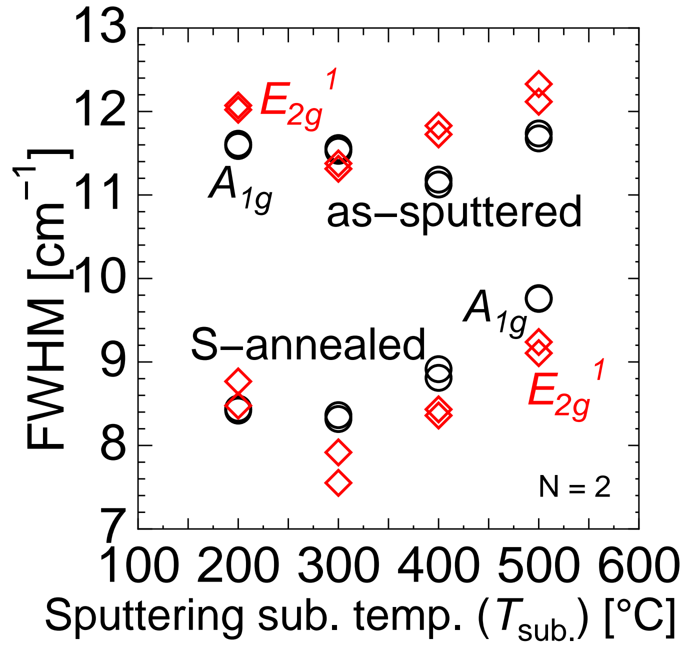


**Figure 4.14**: FWHM values in a wafer for $E^1_{2g}$ and $A_{1g}$ modes from the Raman spectra for as-sputtered and S-annealed $MoS_2$ films as function of substrate temperature during sputtering ($T_{flux}$).

Figure 4.15 shows the correlation between the FWHM values before and after sulfur annealing based on Figure 4.14. The crystallinity for all of the $MoS_2$ films is improved by sulfur annealing. The deviation at 400 and 500°C from the correlation coefficient might indicate that the excessive sulfur desorption just after sputtering severely influences in the amount of crystal recovery during sulfur annealing. On the other hand, the lateral vibration peak is more important for the layered $MoS_2$ film crystallinity, Therefore, we focus on discussion with $E^1_{2g}$ mode. Obtained by subtracting the least squares method from all of $E^1_{2g}$ peaks, a slope coefficient between as-sputtered and sulfur-annealed $MoS_2$ films is 1.5, which is remarkably greater than one. It is thought to be related to the dependence of the lateral crystal size before and after S-annealing. On the other hand, no dependence of $A_{1g}$ peak was observed. However, this is thought to be because there is almost no change in the vertical crystal size before and after S-annealing. Therefore, this result suggests that the improvement of the as-sputtered film quality greatly affects the crystallinity of the $MoS_2$ film obtained after S-annealing. Moreover, it is revealed that using the $MoS_2$ target leads to a higher quality of the final $MoS_2$ film than that of the Mo-target.

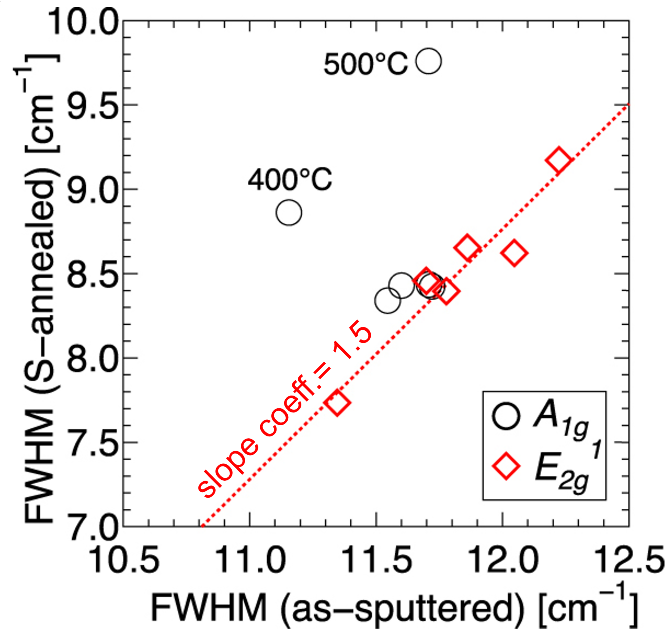


**Figure 4.15**: Relationship between FWHM values for $E^1_{2g}$ and $A_{1g}$ modes of as-sputtered and S-annealed $MoS_2$ films from Figure 4.14. The average values of two-point data for each condition in Figure 4.14 are plotted.

The FWHM values' results discussed the possibility of changing the crystal size and sulfur defect density of $MoS_2$ films by adjusting substrate temperature ($T_{sub.}$). Here, the sulfur defect density is isolated, and the film quality is evaluated. In previous studies, it was reported that the low sulfur vacancy ($V_s$) density reduces the $A_{1g} - E^1_{2g}$ shift values, as shown in Figures 4.16 [31, 42]. Therefore, the $A_{1g} - E^1_{2g}$ shift values are adopted for evaluation of sulfur defect density of $MoS_2$ film deposited by sputtering. The $A_{1g} - E^1_{2g}$ shift values depending on the substrate temperature during sputtering ($T_{sub.}$) is illustrated in Figure 4.17. The diamond data are the $A_{1g} - E^1_{2g}$ shift values for 1–6 monolayers (ML) $MoS_2$ films in previous studies [35]. The reduction in $T_{sub.}$ resulted in a decrease in the $A_{1g} - E^1_{2g}$ shift values. This phenomenon is attributed to a lower sulfur vacancy density ($V_s$), which was mitigated at lower temperatures. Furthermore, after S-annealing, the $A_{1g} - E^1_{2g}$ shift decreased further, indicating that sulfur supplementation during annealing effectively reduced sulfur vacancy density. At a substrate temperature of 300°C combined with S-annealing, the $A_{1g} - E^1_{2g}$ shift approached values similar to those of exfoliated $MoS_2$ with 5–6 ML, as reported in previous studies. This suggests that the process conditions were optimized to minimize sulfur deficiencies and achieve high-quality $MoS_2$ films. On the other hand, when $T_{sub.}$ is 200°C or above 400°C, the Raman shift increases after S-annealing, which is due to an increase in the sulfur defect density.

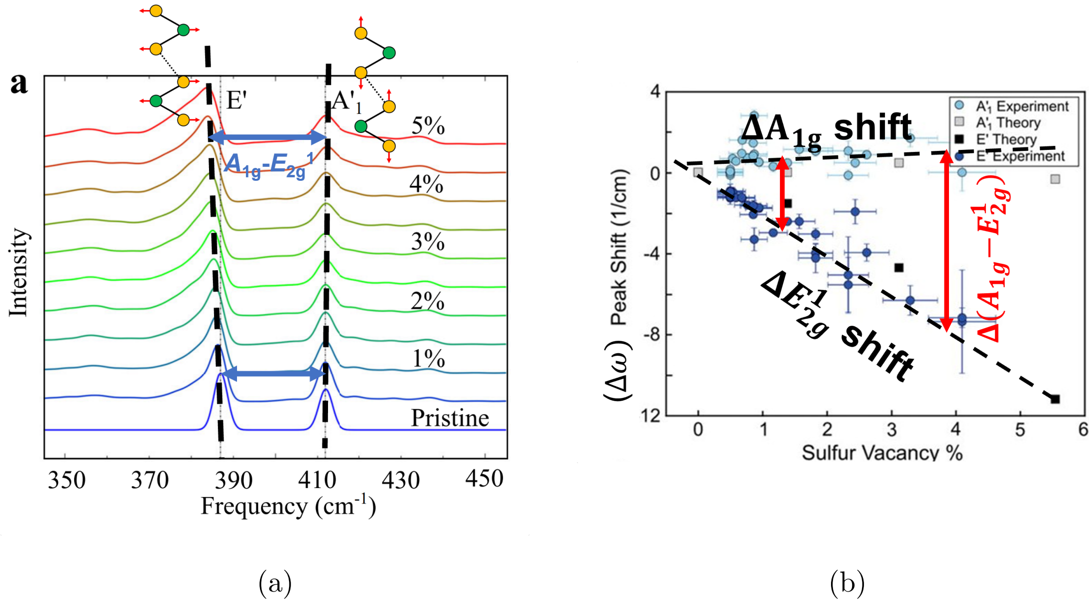


**Figure 4.16**: (a) $MoS_2$ Raman peak intensities and (b) Raman peak shift depending on amount of S defects ($V_s$) [31].

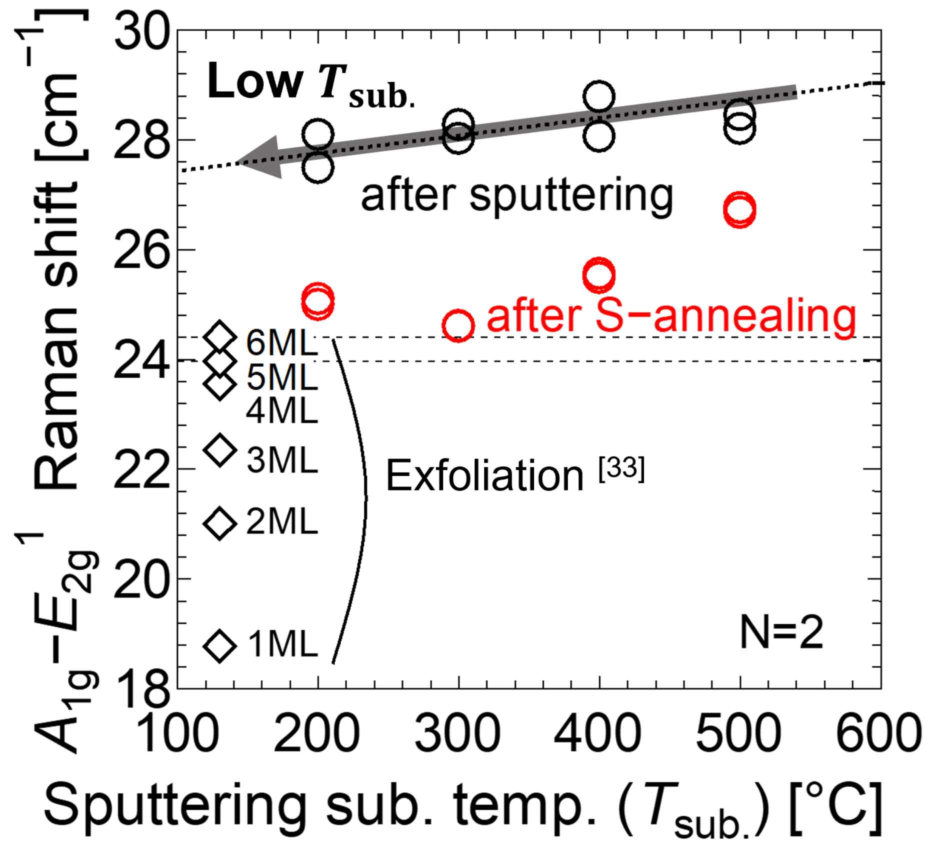


**Figure 4.17**: Dependence of $A_{1g}$-$E^1_{2g}$ shift values after sputtering and S-annealing on sputtered substrate temperature ($T_{sub.}$). Diamond data are those values for 1–6 monolayers (ML) exfoliated $MoS_2$ films [35].

To confirm the sulfur behavior in $MoS_2$ film after sputtering on different substrate temperatures during sputtering ($T_{\text{sub.}}$), as shown in Figure 4.17, the X-ray photoelectron spectra of the Mo $3d$ orbitals for the as-sputtered $MoS_2$ films obtained at 300 and 500°C are shown in Figures 4.18 (a) and (b), respectively. In addition, Figures 4.19 (a) and (b) also show XPS spectra of the S $2p$ orbitals for the as-sputtered $MoS_2$ films at 300 and 500°C, respectively. Mo-S and S-Mo bonds are observed in all Figures 4.18 and 4.19, respectively. However, at 500°C, the Mo-Mo bonds are observed in Figure 4.18 (b), and the S-S bonds are simultaneously observed in Figure 4.19 (b). These results indicate that excessive sulfur desorption generates excessive sulfur remains. On the other hand, at 300°C, no peak of the Mo-Mo and S-S bonds is observed, Mo-O bonds are found in Figure 4.18 (a) and 4.19 (a), respectively. To estimate the sulfur desorption from the as-sputtered $MoS_2$ film, the S/Mo composition ratio was calculated from Figures 4.18 and 4.19. The S/Mo composition ratio of the $MoS_2$ film was obtained by the fraction of areas for Mo $3d$ and S $2p$ spectra divided by their respective relative sensitivity factors (RSF) of 3.54 and 0.717, respectively, as the following equation,

$$\frac{\text{S}}{\text{Mo}} = \frac{\text{Area}_{\text{S }2p}/\text{RSF}_{\text{S }2p}}{\text{Area}_{\text{Mo }3d}/\text{RSF}_{\text{Mo }3d}}. \tag{4.3.2}$$

The calculated S/Mo ratios of the samples after sputtering were 1.69 at 300°C and 1.67 at 500°C, which means sulfur desorption increased at high $T_{\text{sub.}}$. Therefore, it was confirmed that excessive sulfur desorption may influence a crystal recovery during sulfur annealing, as shown in Figure 4.14. On the other hand, although the oxidation of molybdenum is found in Figure 4.18 (a), it has been reported that the oxidation of molybdenum is easily sulfurized [105]. Also, in this study, the S-annealing for the samples sputtered at 300°C is enhanced, compared to the sample at 500°C, as shown in Figure 4.14. Therefore, it is speculated that the S-annealing is enhanced by the presence of oxygen in molybdenum.

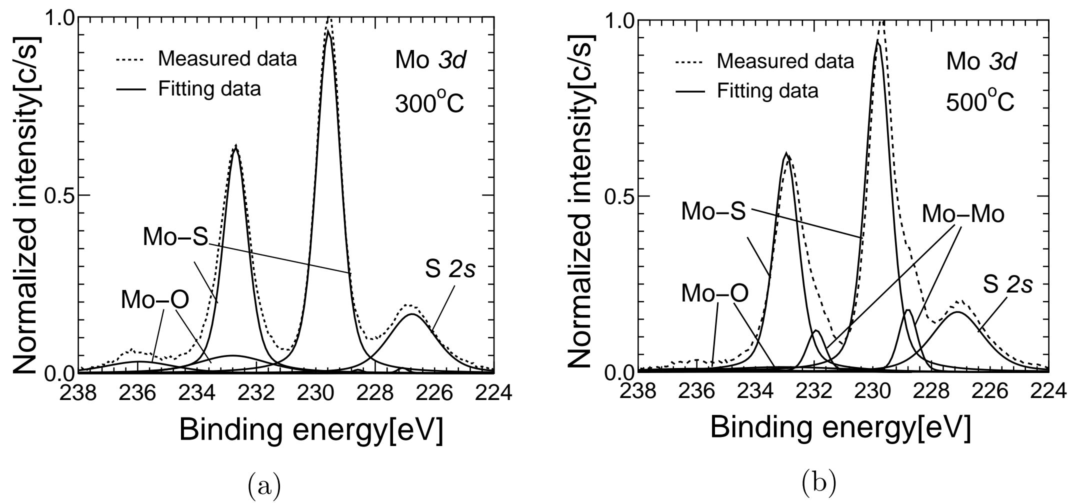


**Figure 4.18**: XPS spectra of molybdenum $3d$ in as-sputtered $MoS_2$ films obtained with substrate temperatures of (a) 300 and (b) 500°C for RF power of 40 W under Ar gas pressure of 0.55 Pa.

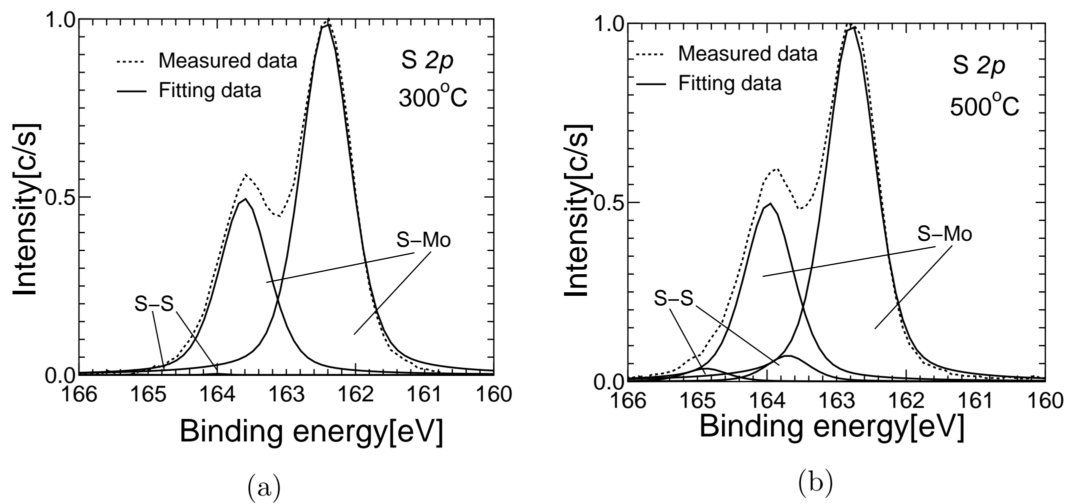


**Figure 4.19**: XPS spectra of sulfur $2p$ in as-sputtered $MoS_2$ films obtained with substrate temperatures of (a) 300 and (b) 500°C for RF power of 40 W under Ar gas pressure of 0.55 Pa.

### 4.3.4 Study on the S-annealing effect of $MoS_2$ films at different substrate temperatures during sputtering ($T_{sub.}$)

From the results of Raman shift values and XPS results, the dependence of substrate temperature during sputtering ($T_{sub.}$) on the S-annealing effects for $MoS_2$ thin films are discussed, as shown in Figure 4.21. The Raman peaks originating from amorphous $MoS_2$ were clearly observed at 200°C, as shown in Figures 4.20 [36–38], in which it is speculated that the amorphous region becomes more prominent when the substrate temperature is low. At the $T_{sub.}$ of 200°C, the substrate predominantly exhibits amorphous regions. Under this condition, the energy required to transform from the amorphous regions to crystalline $MoS_2$ is high, resulting in insufficient crystallization and a high density of residual sulfur vacancies. In contrast, when the $T_{sub.}$ is raised to 500°C, the sulfur vacancy density on the substrate increases drastically. At such high temperatures, sulfur atoms are more likely to desorb from the substrate, leading to severe degradation in crystallinity. At the $T_{sub.}$ of 300°C, the formation of crystalline $MoS_2$ becomes more pronounced, reducing sulfur vacancies. Furthermore, S-annealing performed under this condition significantly decreases the sulfur vacancy density, enhancing the thin film's crystallinity, which suggests that a sputtering temperature of around 300$o$C, combined with S-annealing, provides optimal conditions for minimizing sulfur deficiencies and improving film quality. These discussions demonstrate that the sputtering temperature is critical to influencing the crystallization process and defect formation in $MoS_2$ thin films. In particular, combining an appropriate sputtering temperature and S-annealing is key to achieving high-quality $MoS_2$ films.

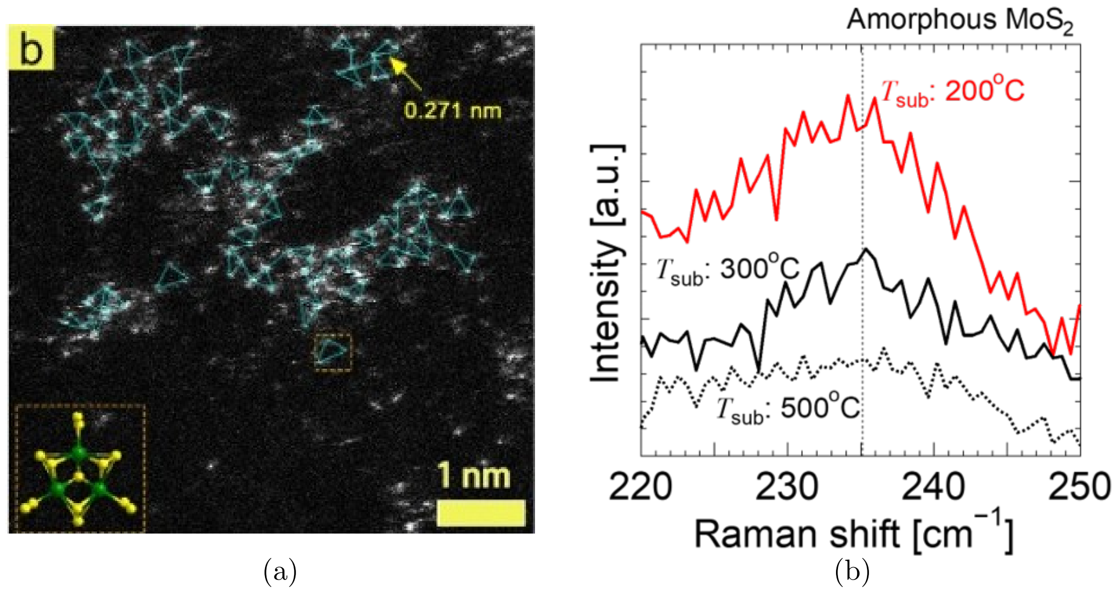


**Figure 4.20**: (a) planner TEM image of amorphous $MoS_2$ [36]. (b) Raman peak results notarized by Si peak intensity of $MoS_2$ film after sputtering at sputtering substrate temperatures ($T_{sub.}$) of 200, 300, and 500°C. amorphous peaks. The peak of amorphous $MoS_2$ is located at 230-240 $cm^{-1}$ [36–38].

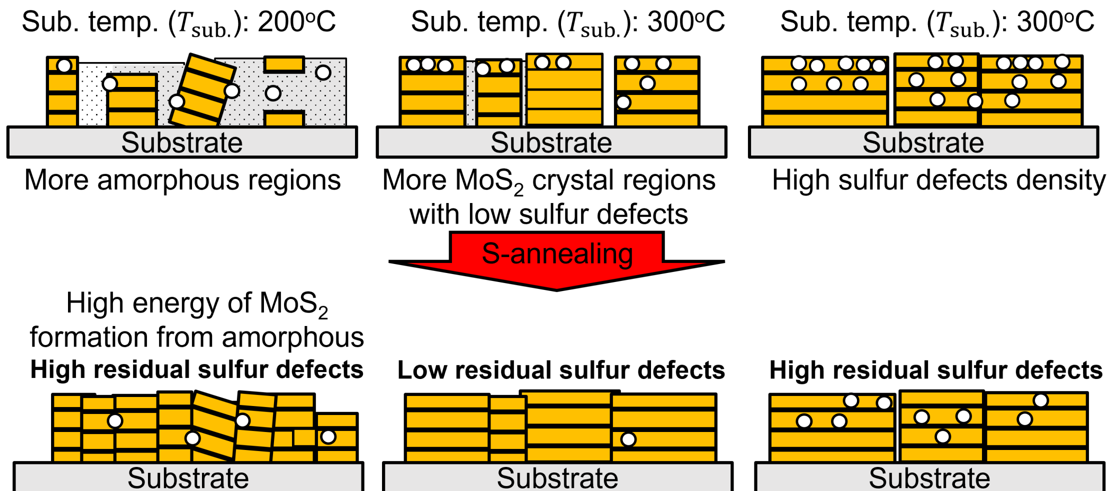


**Figure 4.21**: Comparison of reaction models in S-annealing at sputtering substrate temperatures of 200, 300, and 500°C.

## 4.4 Summary

First, this chapter investigated the effect of S-annealing on sputtered $MoS_2$ films. HAADF-STEM results reveal that S-annealing increases the crystal size of $MoS_2$ films. In

addition, it is considered to have the effect of converting the edge parts of $MoS_2$ crystals from Mo-edge to S-edge and compensate for sulfur defects $V_s$ in the $MoS_2$ film.

Next, the chapter aimed to model the properties of $MoS_x$ films under varying sputtering substrate temperatures ($T_{sub.}$). The results demonstrate that the substrate temperature during sputtering significantly influences the sulfur vacancy density and the resulting film quality. After sputtering, it was observed that higher substrate temperatures led to an increase in sulfur vacancy density. This can be attributed to the lack of sulfur supply under high-temperature conditions immediately after sputtering, resulting in a high concentration of sulfur vacancies. Following sulfur vapor annealing, the sulfur vacancy density was further reduced compared to the as-sputtered films. The results suggest that sulfur supplementation during annealing effectively mitigates sulfur deficiencies. Furthermore, combining a substrate temperature of 300°C during sputtering and subsequent sulfurization annealing produced films with the lowest sulfur vacancy density. These conditions also potentially minimized the presence of amorphous regions in the $MoS_2$ films, indicating enhanced crystallinity and the promotion of sulfur supplementation effects. In future work, sputtering substrate temperatures will be fixed at 300°C to minimize sulfur desorption while reducing amorphous regions and ensuring high-quality $MoS_x$ films.

# Chapter 5

# Crystal size enlargement of $MoS_2$ film with control of flux temperature and particle flux during sputtering

## 5.1 Background

In Chapter 4, the sulfur vacancies have been successfully suppressed by adjusting the substrate temperature to 300°C, with enlargement of the surface migration length of the particles on the substrate. To further reduce the sulfur vacancy density, an attempt will be made to enhance the amount of S flux reaching the substrate. In section 3.2.1, it is revealed that high RF power enhances the Sulfur particle flux reaching the substrate, resulting in a high S/Mo flux ratio. Furthermore, the RF sputtering power also enhances the flux temperature ($T_{\text{flux}}$). At this point, the particle flux to the substrate also increases. Therefore, When adjusting the RF power, a trade-off exists between achieving a high S/Mo flux ratio and a low particle flux on the substrate. Understanding the change in $MoS_2$ film quality due to RF power fluctuation is necessary. In this Chapter, as shown in Figure 5.1, the flux temperature ($T_{\text{flux}}$), which is the energy of the particles reaching the substrate when the RF power is changed, is set to a sufficiently appropriate value to change the migration length of the particles on the substrate surface.

## 5.2 Experimental methods

### 5.2.1 $MoS_2$ film formation by sputtering and S-annealing

A $SiO_2$/Si substrate was used as the base substrate and was cleaned with sulfuric acid: hydrogen peroxide mixture ($4 : 1 = H_2SO_4 : H_2O_2$) to remove organic and metallic impurities. To deposit the $MoS_2$ films, magnetron sputtering systems with radiofrequency (RF) powers from 25–100 W were used, as depicted in Figure 5.2 (a). Other sputtering

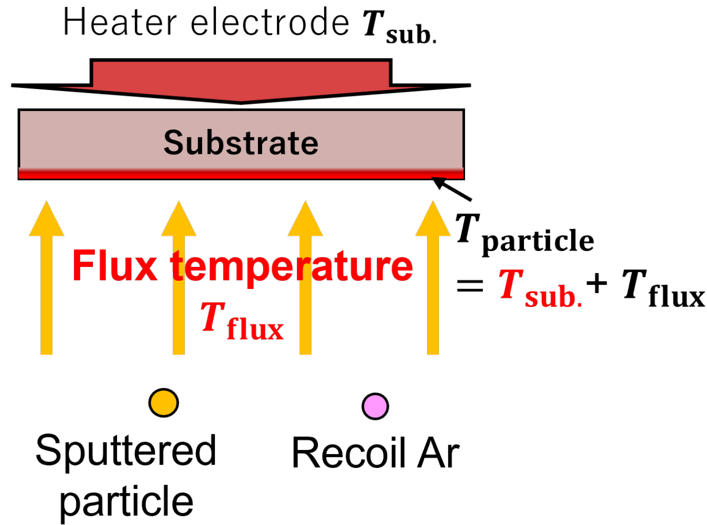


**Figure 5.1**: Approach of long surface migration length of particles on substrate by high flux temperature ($T_{flux}$) with increase in RF power.

parameters included a substrate temperature of 300°C, an Ar pressure of 0.5 Pa, an Ar flow rate of 7 sccm, and a target-to-substrate distance of 150 mm [39]. To achieve the desired stoichiometric composition ratio of the $MoS_2$ film, a sulfur-vapor annealing (S-annealing) was performed, as illustrated in Figure 5.2 (b) [20, 41]. The sulfur placed in zone 1 was heated at 250°C, and the sample placed in zone 2 was heated at 700°C for 40 min. To accurately control the thickness of the $MoS_2$ film, the deposition rate of the $MoS_2$ film was calculated using the following equation:

$$\text{Deposition rate} = \frac{\text{thickness of MoS}_2\text{ film by sputtering and S-annealing}}{\text{deposition time during sputtering}}. \qquad (5.2.1)$$

Figure 6.3 depicts the deposition rate of the $MoS_2$ film depending on the RF power. The deposition rate of the $MoS_2$ film increases with an increase in the RF power attributed to the high particle flux during sputtering. To obtain a $MoS_2$ film with the same thickness of 2.5 nm, the deposition time of sputtering was adjusted based on the deposition rate. This thickness was chosen for two reasons, in which first, it has been reported that an increase in the $MoS_2$ film thickness of more than 10 nm enhances the roughness, resulting in perpendicular growth to the substrate surface [19, 106]. Additionally, it is easy to evaluate the physical properties, such as the Raman spectroscopy and in-plane X-ray diffraction (XRD), with a high signal-noise ratio in the $MoS_2$ film above 2.5 nm. The reason is that the $MoS_2$ films deposited by sputtering have a small peak intensity in these measurements due to smaller grain sizes and higher sulfur defect density than those of the monolayer $MoS_2$ film deposited by exfoliation or CVD. The films were characterized using transmission electron microscopy (TEM) and atomic force microscopy (AFM).

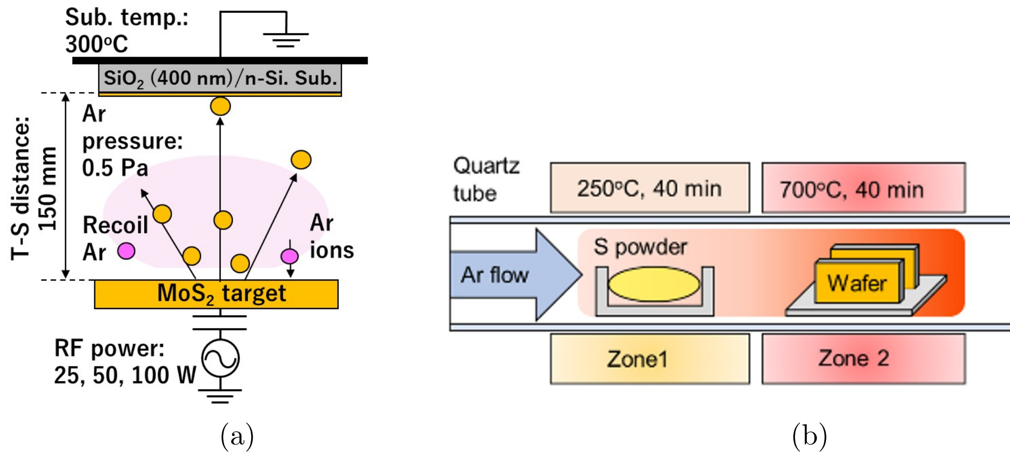


**Figure 5.2**: Schematic of (a) sputtering and (b) sulfur-vapor annealing (S-annealing) systems [39].

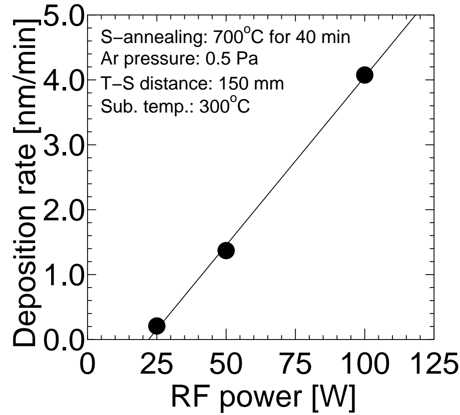


**Figure 5.3**: Deposition rate on RF power of $MoS_2$ films after S-annealing. All samples were deposited by sputtering at 300°C using Ar pressure of 0.5 Pa.

### 5.2.2 Ion energy distribution during sputtering

To evaluate the RF power dependence of the flux temperature ($T_{\text{flux}}$), measurement of the ionized particles reaching the substrate, which are considered to have high energy, will be attempted. Note that the flux temperature ($T_{\text{flux}}$) mainly refers to the energy of neutral and ionic particles incident on the substrate surface. To assess the ion energy distribution (IED) in a separate experiment from the $MoS_2$ film formation, a retarding field energy analyzer (RFEA) was used due to its high sensitivity to small currents without requiring mass separation [107–109]. Figure 5.4 illustrates the experimental setup for measuring the IED during identical RF magnetron sputtering systems in subsection 5.2.1 using the Semion RFEA from Impedans Ltd. The RFEA was positioned on the $SiO_2$/Si substrate. Based on the cross-sectional structure of the RFEA shown in Figure 5.4, the analyzer

has a thickness of 5 mm and consists of four grid electrodes (G0, G1, G2, and G3) and a collector electrode (C). G0 is connected to the body of this analyzer and shares the same bias on the substrate surface. G1 acts as a repelling grid for negative ions during the positive ion measurements. Conversely, during the negative ion measurement, it is a repelling grid for the positive ions. G2 is a discriminator, and G3 is a repelling grid of the secondary electrons from the collector electrode. The IED was calculated from the first derivative of the ion current with respect to G2 voltage [110, 111]. The RF frequency was 13.56 MHz, and a 99.99%-$MoS_2$ target was used. The sputtering parameters were set as follows: Ar pressure of 0.5 Pa and a target-to-substrate distance of 150 mm. Since the energy of the incident ion particles is independent of the substrate temperature, it was set to room temperature. To analyze the energies of the positive and negative ions at high signal-to-noise ratios, the RF power was varied in the range of 50–150 W, which is different from section 5.2.1.

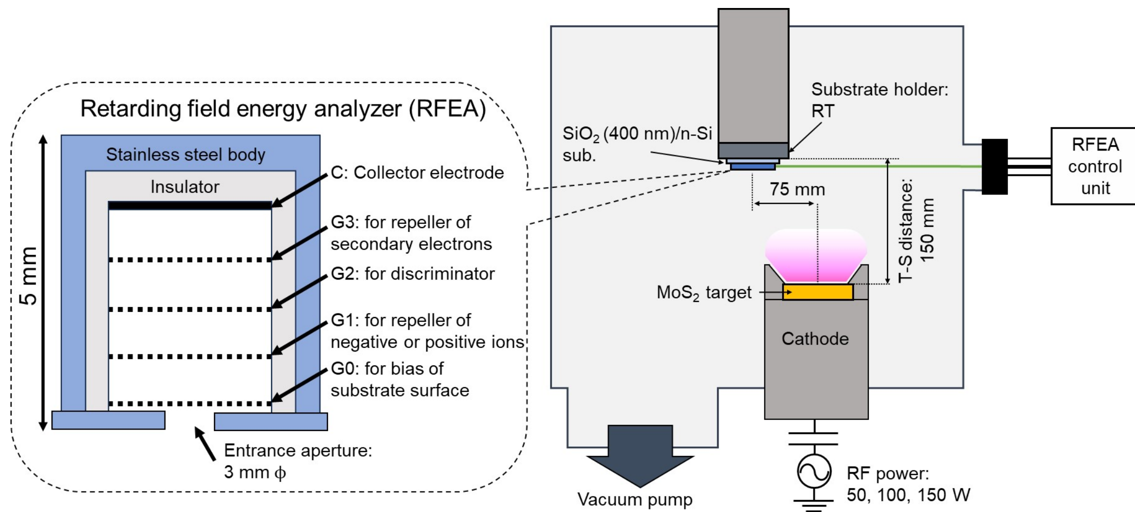


**Figure 5.4**: Experimental setup for ion energy distribution (IED) with retarding field energy analyzer (RFEA) systems during RF magnetron sputtering with $MoS_2$ target. Left inset is cross-sectional structure of RFEA.

## 5.3 Results and discussion

### 5.3.1 $MoS_2$ film formation by sputtering and sulfur-vapor annealing

TEM observations of the samples after sputtering and S-annealing are illustrated in Figures 5.5 (a)-(f). All the $MoS_2$ films after S-annealing are 2.5-nm-thick, as shown in Figures 5.5 (d)-(f). Conversely, when comparing the films after sputtering and S-annealing, an amorphous region is observed at an RF power of 25 W after sputtering, as illustrated in Figure 5.5 (a). These results indicate that at higher RF power, the flux temperature

for the $MoS_2$ crystal growth is sufficient, leading to fewer sulfur vacancies and a negligible thickness difference between the $MoS_2$ films after sputtering and S-annealing.

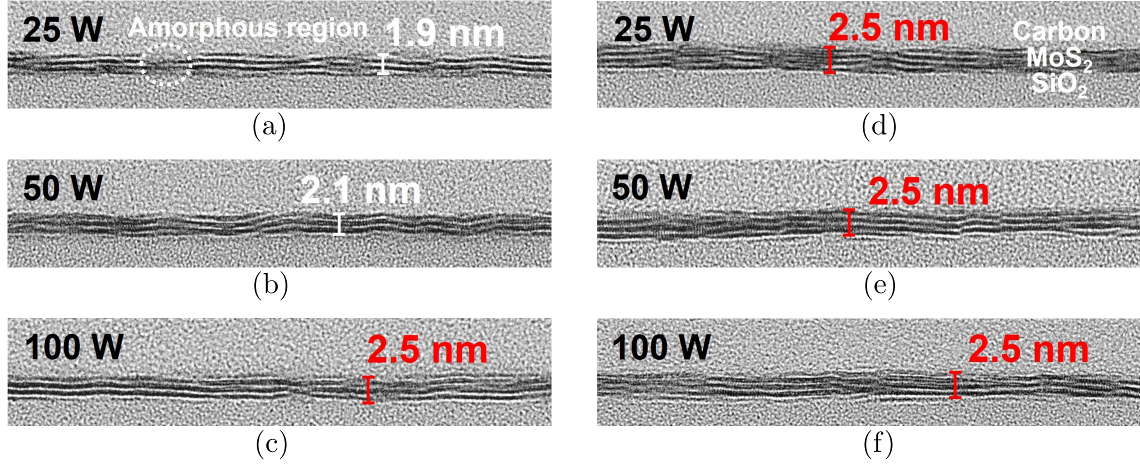


**Figure 5.5**: Cross-sectional TEM images of $MoS_2$ films (a)–(c) after sputtering and (d)–(f) after S-annealing [39].

To assess the crystallinity of the $MoS_2$-film, Figure 5.6 depicts the full width at half maximum (FWHM) values of the $E^1_{2g}$ and $A_{1g}$ peaks in the Raman spectroscopy of the $MoS_2$ films as a function of the RF power. The FWHM values evaluate the inherent crystallinity in terms of both sulfur defect density and crystal size. The FWHM values after sputtering decrease as the RF power increases. This trend is likely because of an increase in the flux temperature ($T_{\text{flux}}$) or S/Mo flux ratio reaching the substrate surface, facilitating crystal growth or low sulfur vacancies, respectively. FWHM values of the $MoS_2$ films after S-annealing are smaller than those after sputtering, indicating that sulfur compensation enhances the crystal recovery. Furthermore, the values observed after the S-annealing exhibit a similar dependence on the RF power after sputtering, signifying the improvement in the crystallinity of the $MoS_2$-film after sputtering is crucial for further enhancement, even after S-annealing [41]. To evaluate the sulfur defect density in $MoS_2$ film by sputtering, Figure 5.7 depicts the $A_{1g}$-$E^1_{2g}$ Raman shift values of the $MoS_2$ film after sputtering and S-annealing compared with those of 1-6 ML $MoS_2$ film in a previous study [35]. These values decrease after sputtering with an increase in the RF power and decrease further after the S-annealing. The $A_{1g}$-$E^1_{2g}$ value in the sample after S-annealing with a power of 100 W is the closest to that of the 5–6 ML $MoS_2$ film in the previous study [35]. Moreover, all samples after S-annealing have a 5–6 monolayer (ML)-$MoS_2$ film, as shown in Figure 5.5 (d)-(f). Parkin *et al.* reported that these values increase with an increase in sulfur defect concentration [42]. Consequently, it is speculated that an increase in the RF power, combined with S-annealing, further reduces the number of sulfur

vacancies due to the high S/Mo flux ratio during sputtering and enhances the crystallinity of the $MoS_2$ film [42].

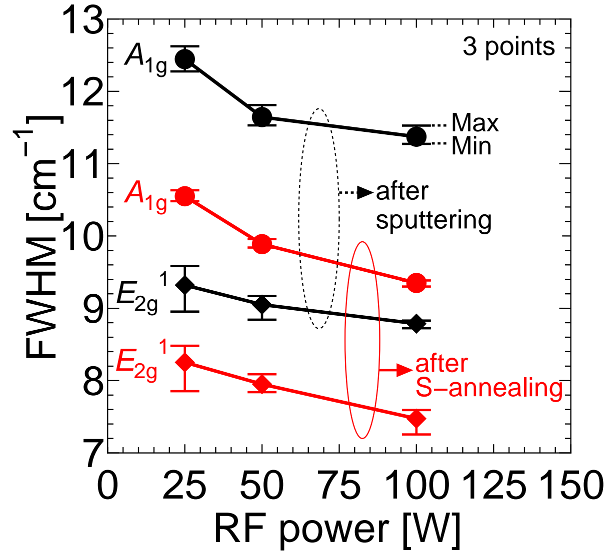


**Figure 5.6**: FWHM values of $E^1_{2g}$ and $A_{1g}$ modes at three points on $MoS_2$ films after sputtering and S-annealing, plotted as function of RF power.

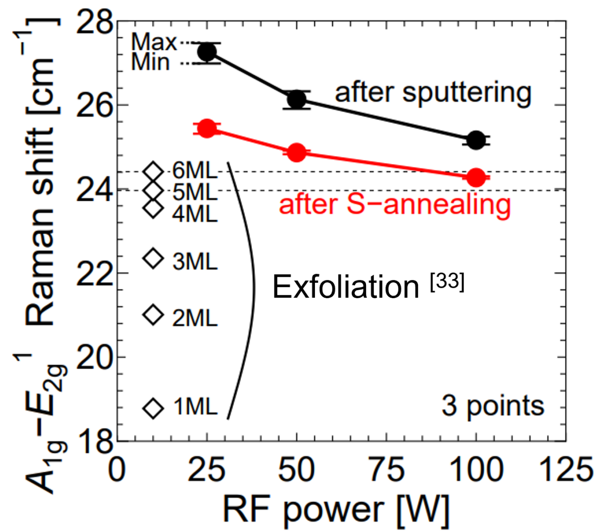


**Figure 5.7**: Raman peak shift values of $A_{1g}$-$E^1_{2g}$ at three points on $MoS_2$ films after sputtering and S-annealing, plotted as function of RF power. Diamond data are those values for 1–6 monolayers (ML) exfoliated $MoS_2$ films [35].

Furthermore, as shown in Figure 5.7, it was confirmed that the sample prepared by low-power sputtering exhibited limitations in improving film quality even after S-annealing. Therefore, the following considerations are made regarding what can and cannot be restored through S-annealing: Restorable by S-annealing, as shown in Figure 5.8.

- Increase in crystal size (incorporation of amorphous and microcrystalline regions into $MoS_2$ crystals).
- Compensation for residual sulfur vacancies in the upper layers.

Not restorable by S-annealing

- Compensation for residual sulfur vacancies in the lower layers.

It has been confirmed that in sputtered samples followed by sulfur annealing, sulfur peaks corresponding to the lower layers are not observed, as shown in Figure 5.9 [40].

To evaluate the morphology and the roughness of the film surfaces, AFM images of $MoS_2$ films after sputtering at an RF power of 50 W and after S-annealing, as shown in Figures 5.10 (a) and (b), respectively. After sputtering, the root mean square (RMS) value is 0.20 nm, confirmed to be almost the same in the lateral layer growth mode of previous research [19]. Therefore, it is speculated that the $MoS_2$ film is formed parallel to the substrate surface. Furthermore, the RMS value after S-annealing is 0.08 nm, which can be attributed to the enhanced wettability during high-temperature annealing with a sulfur vapor atmosphere to promote the smoothing of the $MoS_2$ film.

To evaluate the orientation of $MoS_2$ films, in-plane XRD measurements shown in Figure 5.11 (a) were performed. In-plane XRD can reveal lattice planes perpendicular to the substrate surface by shallowly irradiating X-rays on the substrate surface. Figure 5.11 (b) shows the relationship between grain size and crystallite size in $MoS_2$ films, and in-plane XRD can evaluate the crystallite size.

Figure 5.12 (a) depicts the in-plane XRD results for the $MoS_2$ film after sputtering at an RF power of 50 W and after S-annealing. The $MoS_2$ (100), (110), and (200) peaks are observed, and (002) near 15 degrees and (103) near 40 degrees are not observed [112], indicating that the $MoS_2$ films are arranged in a mosaic pattern on the substrate surface. The $MoS_2$ peak intensities are enhanced after S-annealing, which confirms the effect of the crystal recovery by the sulfur compensation. Furthermore, the crystallite sizes of the $MoS_2$ films are calculated, as illustrated in Figure 5.12 (b) using the Scherrer equation [113]

$$D_{100} = \frac{K_{100}\ \lambda}{B_{100}\ cos\ \theta}, \tag{5.3.1}$$

where the constants $K_{100}$ and the X-ray wavelength $\lambda$ are 0.890 and 0.154 nm, respectively. FWHM values of $B_{100}$ and the Bragg angle $\theta$ were obtained from the $MoS_2$ (100) plane peak shown in Figure 5.12 (a). Estimated crystallite size of the $MoS_2$ film after S-annealing depends on that after sputtering, which indicates that the crystallite size remained consistent even after S-annealing. Notably, the crystallite size decreases at both

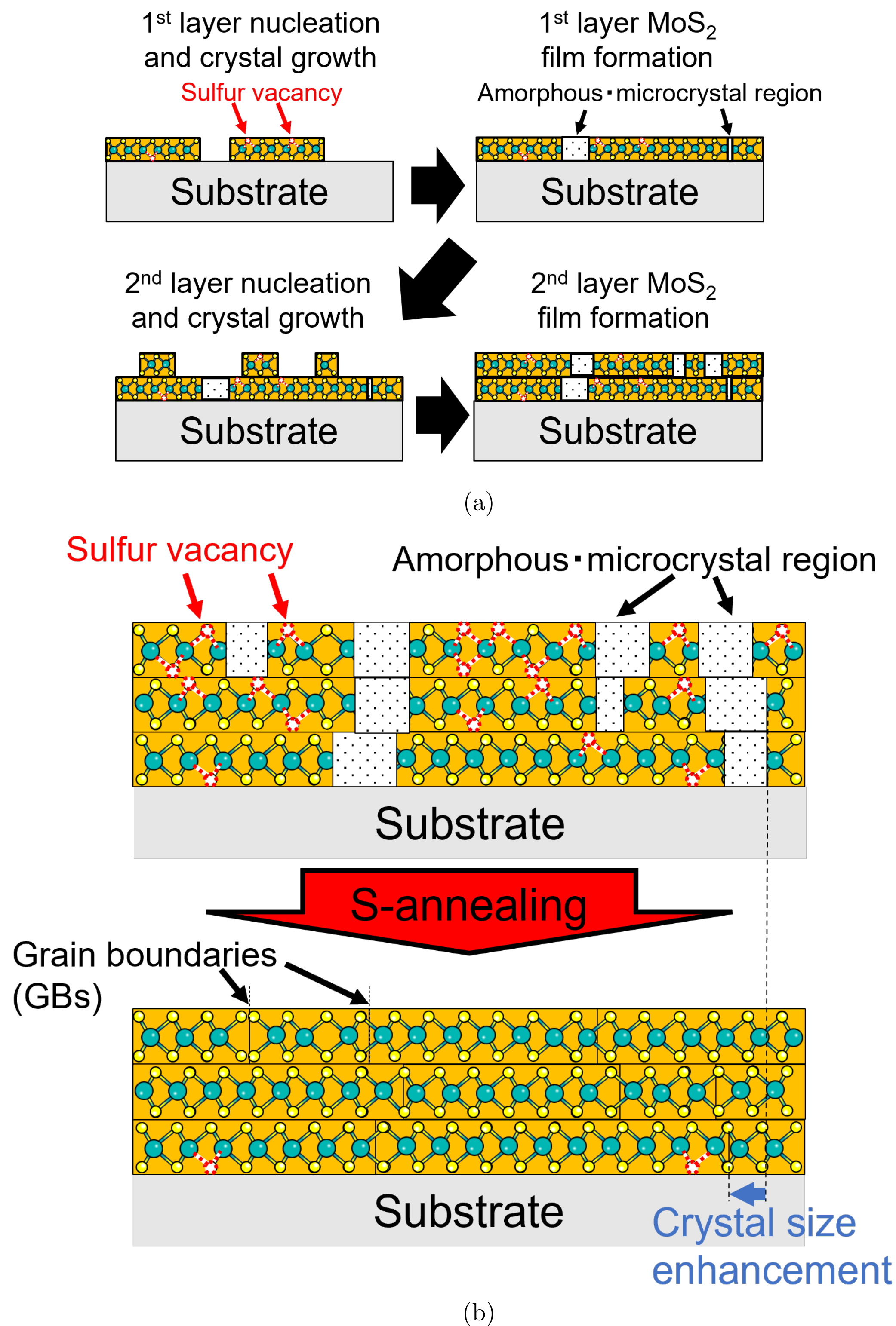


**Figure 5.8**: (a) Model of $MoS_2$ film formation considered with formations of sulfur defects and amorphous/microcrystalline regions during sputtering. (b) Schematic of S-annealing effects and its limitation for $MoS_2$ film by sputtering.

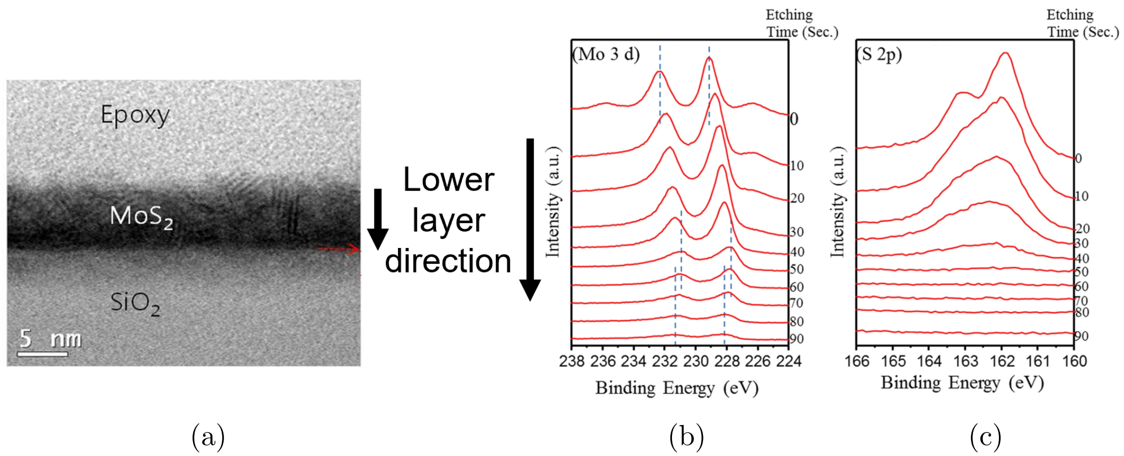


**Figure 5.9**: (a) Cross-sectional TEM image of $MoS_2$ film formed by sputtering and S-annealing. (b) Mo $3d$ and (c) S $2p$ depth profiles of XPS [40]. Black arrow indicates direction of lower layer.

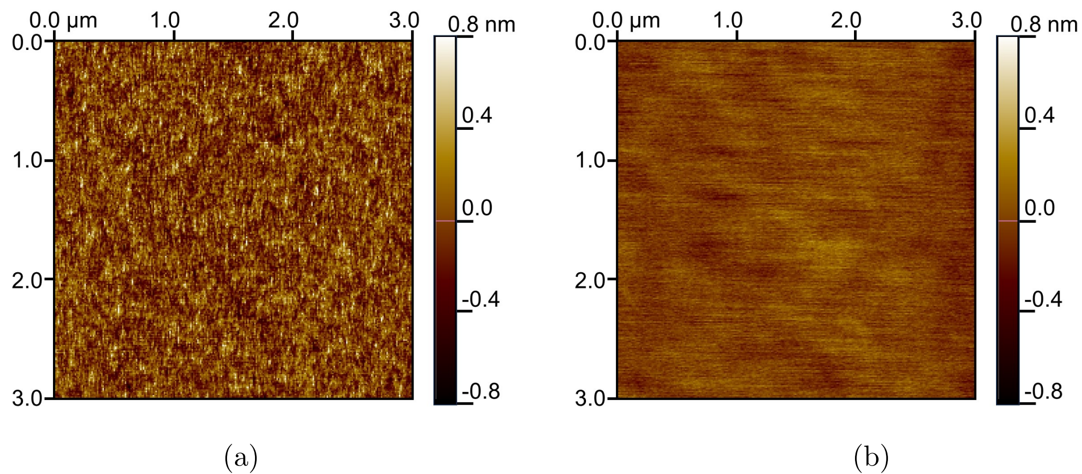


**Figure 5.10**: AFM images of $MoS_2$ films (a) after sputtering with RF power of 50 W and (b) after S-annealing. Root mean square values of roughness are 0.20 and 0.08 nm, respectively.

low and high RF powers, which contradicts the result of the high-$MoS_2$ crystallinity film with a higher RF power, as illustrated in Figure 5.6.

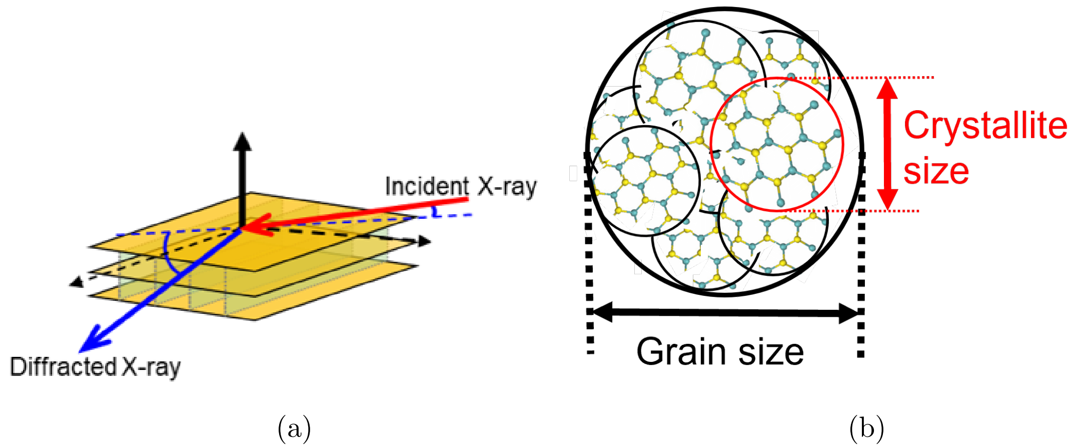


(a) (b)

**Figure 5.11**: (a) Schematic of in-plane X-ray diffraction. (b) Relationship between crystallite size and grain size in $MoS_2$ film.

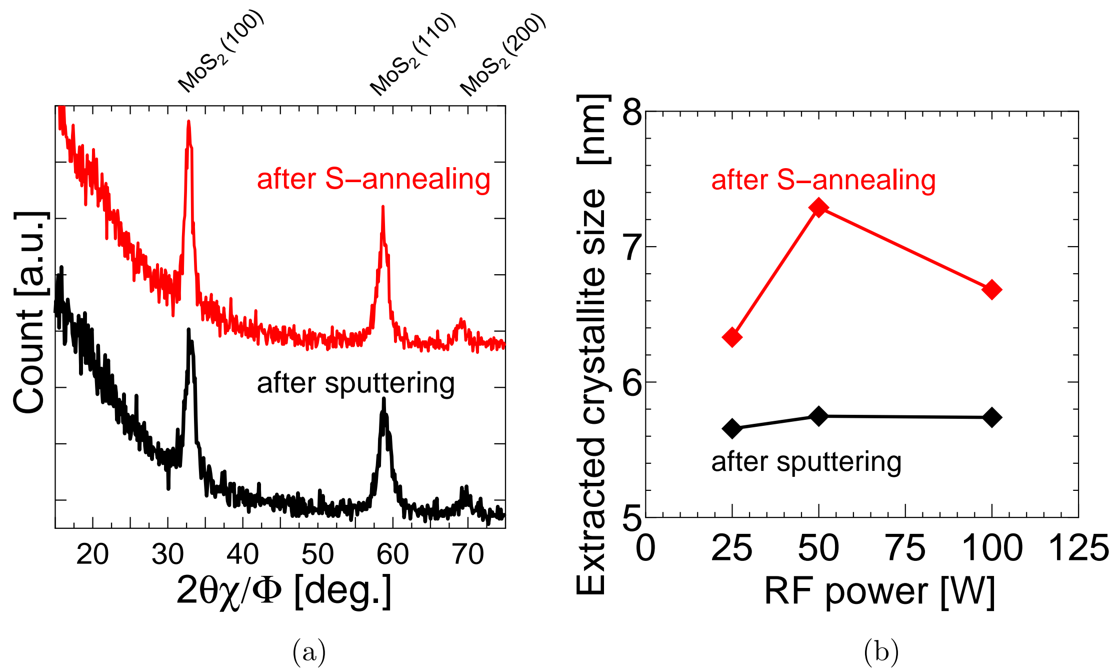


(a) (b)

**Figure 5.12**: (a) XRD patterns and (b) calculated grain size of $MoS_2$ films after sputtering and S-annealing, plotted as function of RF power [39].

### 5.3.2 Ion energy distribution during sputtering

Since the flux temperature depends on the particle energy, the increase or decrease in flux temperature ($T_{\text{flux}}$) in the RF power swing can be estimated from the measurements in this section.

To examine the particle energy reaching the substrate surface depending on the RF power, the positive and negative ion energy distributions (IEDs) were assessed using the retarding field energy analyzer (RFEA) systems, as illustrated in Figure 5.13. The positive ions are considered to be $Ar^+$ in the plasma. Conversely, the negative ions can be sulfur-negative ions, secondary electrons from the target or in the plasma [111, 114]. As the RF power increases, positive and negative IEDs exhibit higher peak intensities due to an increase in the plasma density, which enhances the amount of $Ar^+$, negative ions, and electrons reaching the substrate surface. Figures 5.14 (a) and (b) show the ion fluxes and average energies on the RF power measured by the RFEA systems. The positive and negative ion fluxes increase due to the enhancement in the IED peak intensities, as depicted in Figure 5.13. Furthermore, the average energy of the positive ions decreases with an increase in the RF power, as depicted in Figure 5.14 (b). It is speculated that an increase in the plasma density at the high RF power reduces the electron temperature, leading to the suppression of the $Ar^+$ acceleration in the sheath near the substrate [115, 116]. Conversely, the energy of the negative ions increases with higher RF power due to the enhanced acceleration of the negative ions in the sheath near the target. Figure 5.14 (c) shows the energy fluxes of the positive and negative ions and the total ion energy flux, which is calculated from the product of the ion flux and the average energy. The total ion energy flux, represented by blue circles, increases with an increase in the RF power. Moreover, it is assumed that the energy flux of the neutral particles, such as sputtered particles and recoiling Ar, increases with an increase in the RF power, as presented in Table 5.1 [117, 118]. Thus, the higher energy flux to the substrate surface at the higher power is crucial for enhancing the flux temperature ($T_{\text{flux}}$), which enhances the crystallinity of the $MoS_2$ film, as depicted in Figure 5.6.

**Table 5.1**: RF power dependence of self-bias ($V_{\text{DC}}$) of sputtering target surface.

| RF power [W] | 25 | 50 | 100 | 150 |
|---|---|---|---|---|
| $V_{\text{DC}}$ [V] | - 47.5 | - 73.9 | - 94.8 | - 112 |

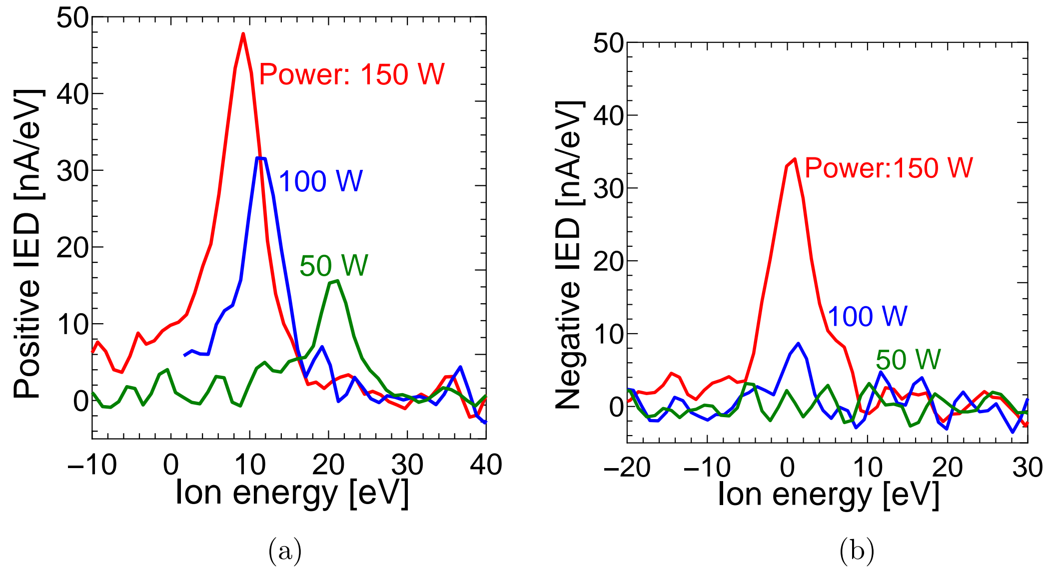


**Figure 5.13**: (a) Positive and (b) negative ion energy distributions (IEDs) using REFA systems during $MoS_2$ sputtering. RF power was varied from 50 to 150 W.

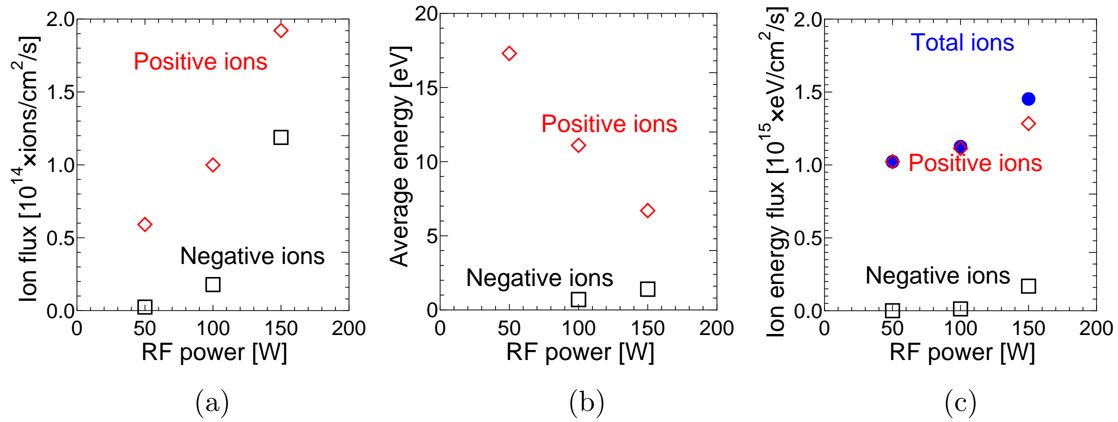


**Figure 5.14**: (a) Ion flux, (b) average energy and (c) ion energy flux of positive and negative ions reaching the substrate surface as function of RF power. (a) and (b) are measured from RFEA systems, and (c) is calculated from product of (a) and (b).

### 5.3.3 Surface migration model during sputtering

To evaluate the $MoS_2$ crystallite size depending on the RF power, a surface migration model of the sputtered particles on the substrate was developed, as depicted in Figure 5.15. This model considers the particle diffusion due to the particle energy and number of particles on the substrate during sputtering, based on Fick's law with the diffusion only by concentration gradients on the substrate surface [119]. At low RF power, the low-flux temperature inhibits the migration of the sputtered particles on the substrate surface, leading to smaller crystallite sizes. Conversely, at high RF power, the flux temperature for the particle migration is sufficient. Since the particle flux is enlarged from the XRR results in Figure 6.3, the number of particle collisions on the substrate surface increases during the sputtering deposition, which results in a smaller surface migration length leading to small crystallite sizes. These considerations are consistent with the crystallite size results in Figure 5.12 (b). Therefore, the intermediate RF power of 50 W is appropriate to enhance the $MoS_2$ crystallite size. Further increase in the $MoS_2$ crystallite size can be achieved by minimizing the particle flux while providing sufficient flux temperature for a longer particle migration length. Although the energy of the Ar plasma controlled by the RF power is expected to be independent of the substrate temperature and Ar pressure, it may be necessary to elucidate in the future how the morphology of the $MoS_2$ films changes with the oblique or normal incidence of ion particles reaching the substrate by the original Thornton and related -models [120]. The crystallite size of the $MoS_2$ film obtained in this study is smaller than that of the CVD [121, 122]. This phenomenon is attributed to be due to elevated particle flux compared to the CVD method, where particles are deposited before reaching a stable position for crystal growth. Therefore, further suppression of the particle flux during sputtering is expected to enhance the $MoS_2$ grain- or crystallite-size [123].

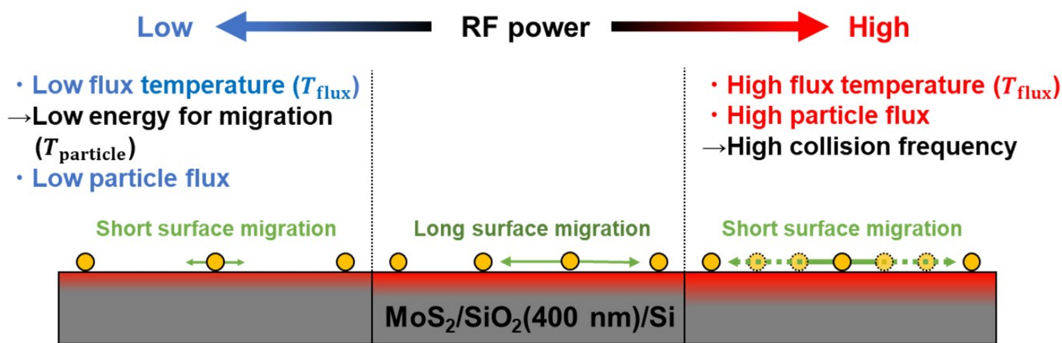


**Figure 5.15**: Schematic of surface migration models of sputtered particles on the substrates during $MoS_2$ film deposition by sputtering.

## 5.4 Summary

In this Chapter, an investigation was carried out to understand the change in $MoS_2$ film quality with RF power.

According to Raman spectroscopy results, the crystallinity of $MoS_2$ films was improved by sputtering with high RF power and S-annealing. It is considered to be the effect of increasing the S/Mo ratio by high RF power and promoting $MoS_2$ crystallization by increasing the flux temperature. Furthermore, XRD analysis showed that the $MoS_2$ crystallite size after sputtering and S-annealing increased significantly at moderate RF power. Moreover, as measured by the RFEA system, the ion energy flux at the substrate surface increases with increasing RF power, which reveals that sufficient flux temperature ($T_{\mathrm{flux}}$) is provided to the substrate at high RF power.

From these results, it is considered that in the case of low RF power, the particle flux is low, and there is time for migration. However, since the $T_{\mathrm{flux}}$ is low, there is little movement on the substrate surface, and crystallization does not occur. Also, because the S/Mo flux ratio was small, there were many sulfur vacancies ($V_{\mathrm{s}}$), and the effect of S annealing appeared to be tremendous, confirming the increase in film thickness. On the other hand, crystallization is more likely to occur at high RF power due to the high $T_{\mathrm{flux}}$. As the next particle arrives, there is no time for migration, and nuclei are generated in unstable locations, resulting in a small crystallite size. Therefore, the moderate RF power is considered to have achieved sufficient $T_{\mathrm{flux}}$ and low particle flux, expanding the surface migration length of the sputtered particles on the substrate surface and enlarging crystallite size of $MoS_2$ film. As in Chapter 4, the effect of S-annealing is to compensate for sulfur vacancies $V_{\mathrm{s}}$ and to enlarge the crystallite size by binding S to the Mo edges of $MoS_2$ crystals and incorporating microcrystals. It was also revealed that this depends on the original $MoS_2$ crystallite size.

A further increase in crystallite size of $MoS_2$ film is expected by further reducing the particle flux during sputtering.

# Chapter 6

# Crystal size enlargement of $MoS_2$ film by low-particle-flux sputtering

## 6.1 Background

In chapter 5, it is confirmed that sufficient flux temperature $T_{\mathrm{flux}}$ and low particle flux enhance the surface migration length of the sputtered particles on the substrate, which enlarges the crystal size of $MoS_2$ film. Further enhancing the crystal size of $MoS_2$ films is important. Notably, enlargement of the grain size of $MoS_2$ films has been reported by using low-rate deposition in the CVD process [124]. Specifically, lowering the evaporation rate of the precursor has reduced the nucleation density and enhanced the grain size [124]. To consider the mechanism of grain size enhancement, it is necessary to reduce the nucleation density. As shown in Figure 6.1, nucleation is assumed to occur where particles collide with each other on the substrate. Therefore, a low collision frequency is assumed to lead to a low nucleation density. This is essentially equivalent to an increase in the surface migration length of particles on the substrate. That is, to lower the collision frequency, it is important to suppress the number of particles reaching the substrate per unit time per unit area (*i.e.*, the particle flux), which is expected to achieve a similar effective method also in physical vapor deposition (PVD).

To achieve the low particle sputtering, the following methods are considered:

- Reduction of the sputtering rate by removing magnets.
- Decrease in sputtering power density per unit area through large target adjustments.
- Suppression of the number of particles reaching the substrate by introducing a grid directly beneath the substrate.

A low-particle-flux deposition method using various grids allows easy implementation and precise control of particle flux by varying the grid's open area ratio. Therefore in this study, a low particle flux in the PVD method is investigated for depositing $MoS_2$ films using a 99.99% molybdenum (Mo) grid placed between the target and substrate in PVD systems to prevent the contamination in $MoS_2$ film due to a concerned erosion of the grid.

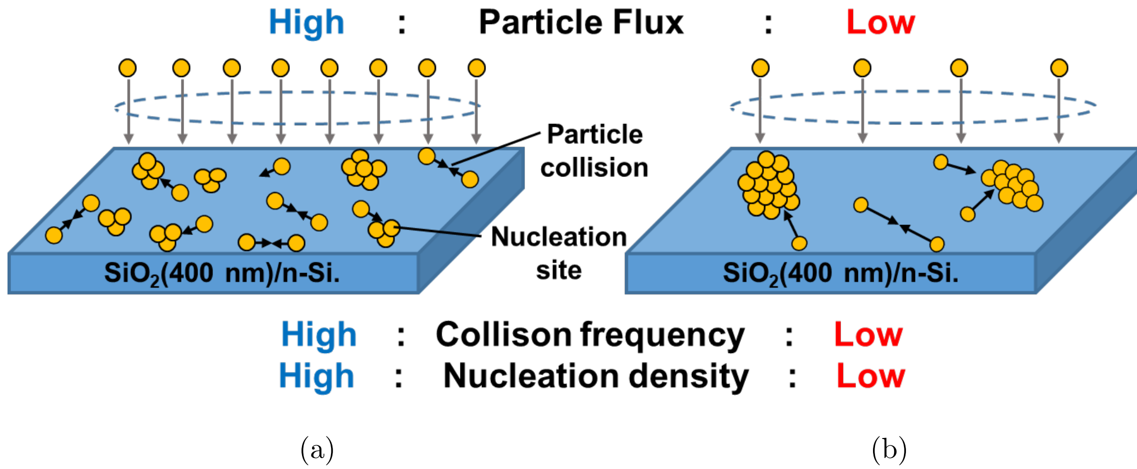


(a) (b)

**Figure 6.1**: Diagram showing particle flux and nucleation density on the substrate surface. Assumptions for at (a) high and (b) low particle flux, respectively.

## 6.2 Experimental methods

Before the formation of a $MoS_2$ film, the $SiO_2$/Si substrate was treated with a sulfuric acid–hydrogen peroxide mixture ($4 : 1 = H_2SO_4 : H_2O_2$) at 180°C for 10 min to remove metal particles and organic materials. The $MoS_2$ film was formed by ultra-high vacuum (UHV) radio frequency (RF) magnetron sputtering using a 99.99% $MoS_2$ target with a diameter of 80 mm. The base pressure was less than $1 \times 10^{-5}$ Pa. The sputtering parameters were an RF power of 40 W, Ar pressure of 0.4 Pa, Ar flow rate of 7 sccm, and target-substrate distance of 150 mm. Although higher substrate temperature is expected to enhance the surface migration length of the particles and improve the crystal size, it has been revealed that the number of sulfur defects increases in the $MoS_2$ film, as shown in chapter 4 Therefore, the substrate temperature was fixed at 300°C.

To reduce the deposition rate, a Mo grid was introduced into the sputtering apparatus in Figure 6.2. The distance between the grid and the target was set to 120 mm. The Mo grid can suppress the amount of sputtered particles per unit time reaching the substrate from the target. Because sputtering parameters such as the RF power and Ar pressure are not changed, the sputtered particle flux can be suppressed without reducing the energy of each sputtered particle. The Mo grid was used under a floating potential, and the projected aperture (PA) ratio of the Mo grid was varied as 100, 60, and 27%. The total PA ratio was calculated from the PA ratios of the respective grids. The PA ratio of 100% means without a grid. The PA ratio of 60% was obtained by two stacked grids with 0.3-mm wire diameter and 2.24-mm aperture gap resulting in 78% aperture area Also, the PA ratio of 27% was achieved by further stacking an additional one grid with 0.35-mm wire diameter and 0.71-mm apertures gap resulting in 44.8% aperture area. Figure 6.3 shows each deposition rate derived from measurements of the $MoS_2$ film thickness using

X-ray reflection. The results confirm that the deposition rate decreased with a decrease in the PA ratios. Under each PA ratio, all the samples were deposited as a 2.5 nm-thick $MoS_2$ film. The samples were evaluated by the Raman spectroscopy at 532 nm, X-ray photoelectron spectroscopy (XPS) with Al $K_\alpha$ radiation and in-plane X-ray diffraction (XRD) with Cu $K_\alpha$ radiation generated at 45 kV and 200 mA.

Table 6.1 is an assumption of the number of particles and flux behaviors on the substrate surface with and without Mo-grids. The number of particles and energy reaching the substrate are represented as $N$ and $E$, and the unit area and unit time as $\mathrm{d}A$ and $\mathrm{d}t$, respectively. The average energy of one particle is noted as $E/N$. The particle number and energy reaching the substrate surface per unit area per unit time are called particle flux and energy flux, respectively. In this study, the flux temperature ($T_{\text{flux}}$) has the same meaning as the energy flux, so the particle flux and flux temperature ($T_{\text{flux}}$) are represented by $N/(\mathrm{d}A \cdot dt)$ and $E/(\mathrm{d}A \cdot dt)$, respectively. Therefore, flux temperature (energy flux) equals the following equation (6.2.1):

$$\text{Flux temperature } (T_{\text{flux}}) = \text{Energy flux} = \frac{E}{\mathrm{d}A \cdot \mathrm{d}t} = \frac{E}{N} \times \frac{N}{\mathrm{d}A \cdot \mathrm{d}t} = \frac{\mathrm{E}}{\mathrm{N}} \times \text{particle flux.} \quad (6.2.1)$$

Even if $E/N$ was constant with or without the grid, the particle flux decreases simultaneously with flux temperature ($T_{\text{flux}}$) when the grid is in place.

**Table 6.1**: Assumption of number of particles and flux behavior with and without Mo-grids.

| | w/o grid | w/ grid |
|---|---|---|
| Deposition rate of $MoS_2$ film | High | Low |
| Average energy of one particle ($E/N$) | Same values | |
| Particle flux ($N/(dA \cdot dt)$) | High | Low |
| Flux temperature ($T_{\text{flux}}$) (Energy flux) ($E/(dA \cdot dt)$) | High | Low |

To evaluate the crystal structure of the $MoS_2$ film formed by sputtering, plan-view transmission electron microscopy (TEM) observations were conducted. To prevent damage to the $MoS_2$ film during the TEM specimen preparation, a TEM grid with a 20-nm-thick $SiO_x$ membrane was used. In addition, a single-layer $MoS_2$ film was sputtered directly onto the TEM grid to prevent the observation of moiré patterns in the $MoS_2$ film [104], and TEM observations were subsequently conducted in Figure 6.4.

Crystal structures were obtained by high-angle annular dark-field scanning TEM (HAADF-STEM). Moreover, crystal orientation distributions were evaluated by the automated crystal orientation mapping in TEM (ACOM-TEM) technique using the ASTAR (TM) systems [102, 125, 126]. The measurement areas are $150 \times 150$ nm$^2$. A 7-degree step in a diffraction pattern in this study classified the grain orientation. The electron beam accel-

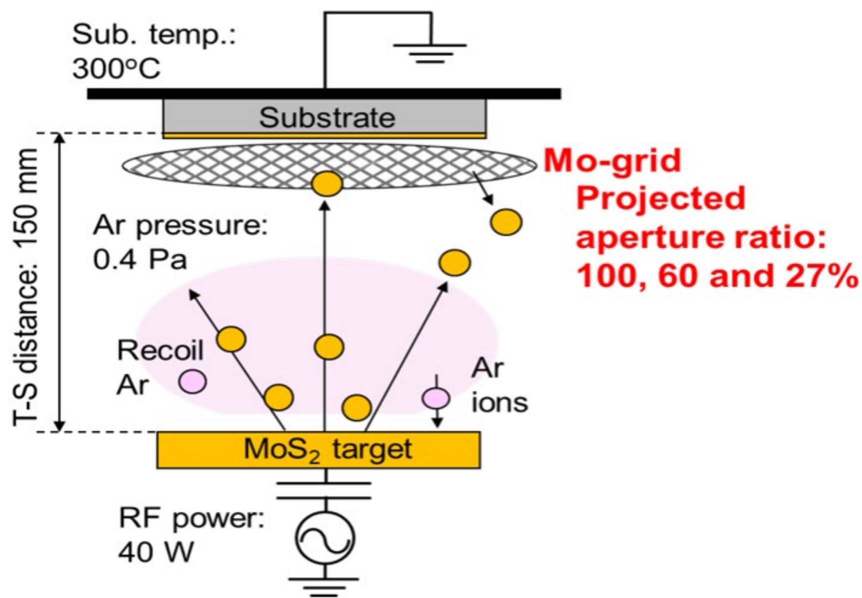


**Figure 6.2**: Schematic of $MoS_2$ low-particle-flux sputtering systems using molybdenum grid, of which the projected aperture (PA) ratio was varied as 100, 60 and 27%.

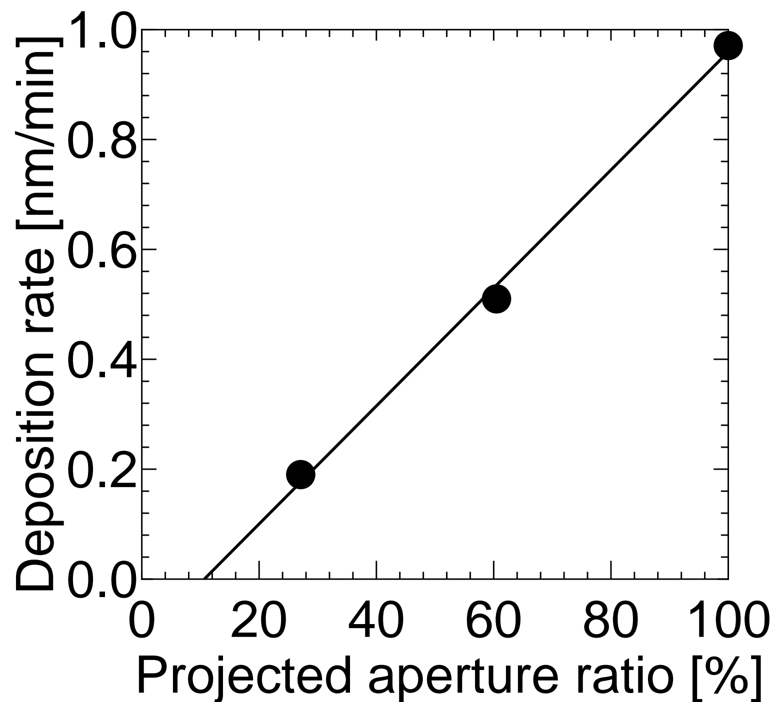


**Figure 6.3**: Dependence of $MoS_2$ deposition rate on PA ratio of molybdenum grid. All thicknesses of $MoS_2$ films are less than 5 nm without perpendicular growth.

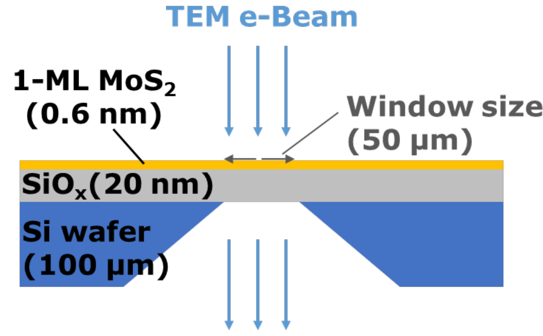


**Figure 6.4**: Schematic of TEM observation structure for $MoS_2$ film.

eration was set to 80 and 200 kV for the HAADF-STEM and ACOM-TEM methods.

## 6.3 Results and discussion

Figure 6.5 (a) shows the Raman spectra of $MoS_2$ films prepared at different deposition rates. It is confirmed that the Raman peak intensity of the $MoS_2$ film increases with a decrease in the deposition rate. In addition, the full-width at half-maximum (FWHM) values of $A_{1g}$ and $E^1_{2g}$ peaks in Figure 6.5 (b) correspond to the vertical and horizontal vibration modes of the $MoS_2$ film, respectively. The results show that the crystallinity improved with a decrease in the deposition rate. We speculate that this is because of the enlargement of crystal size in $MoS_2$ film caused by the reduction of particle flux to the substrate from Table 6.1.

Furthermore, the $A_{1g}$-$E^1_{2g}$ shift value in Raman spectroscopy is shown in Figure 6.6. It was confirmed that the $A_{1g}$-$E^1_{2g}$ shift value decreased, and sulfur vacancies in $MoS_2$ films decreased at low-rate deposition with Mo-grid. This is thought to be because $MoS_2$ crystals were easily formed due to the increase in the surface migration length of particles in low-rate deposition. Moreover, when the deposition rate was decreased to 0.19 nm/min, the $A_{1g}$-$E^1_{2g}$ shift value increased slightly. This is thought to be because the number of sulfur atoms present on the substrate surface under low particle flux conditions decreased due to the tendency of sulfur atoms on the substrate surface to evaporate. Even taking these factors into consideration, the $MoS_2$ film with the smallest $A_{1g}$-$E^1_{2g}$ shift value and the lowest sulfur defect density was obtained when sputtering was performed at a substrate temperature of 300°C.

The number of layers in the experiments was set to 5ML to obtain stable peak intensities with a high signal-to-noise ratio (SNR) for Raman spectroscopy and X-ray diffraction. On the other hand, 1 ML $MoS_2$ film is desirable for suppressing the short channel effect. Additionally, experiments with 1ML and 2ML were carried out, as shown in Figure 6.7. It was confirmed that the $A_{1g}$-$E^1_{2g}$ shift decreased as the number of $MoS_2$ film layers decreased. In addition, the better the 5ML results, the better the 1ML film quality, so

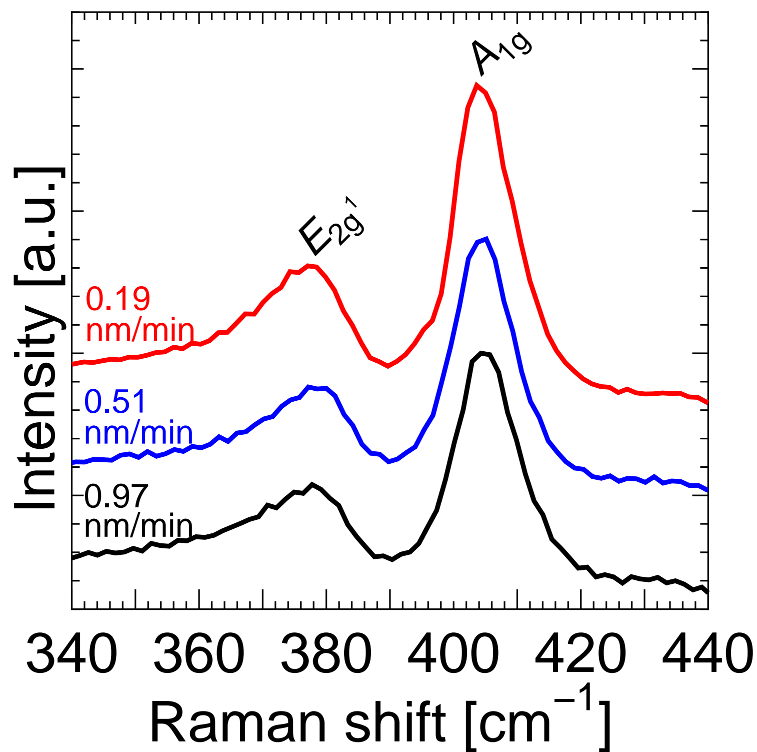


(a)

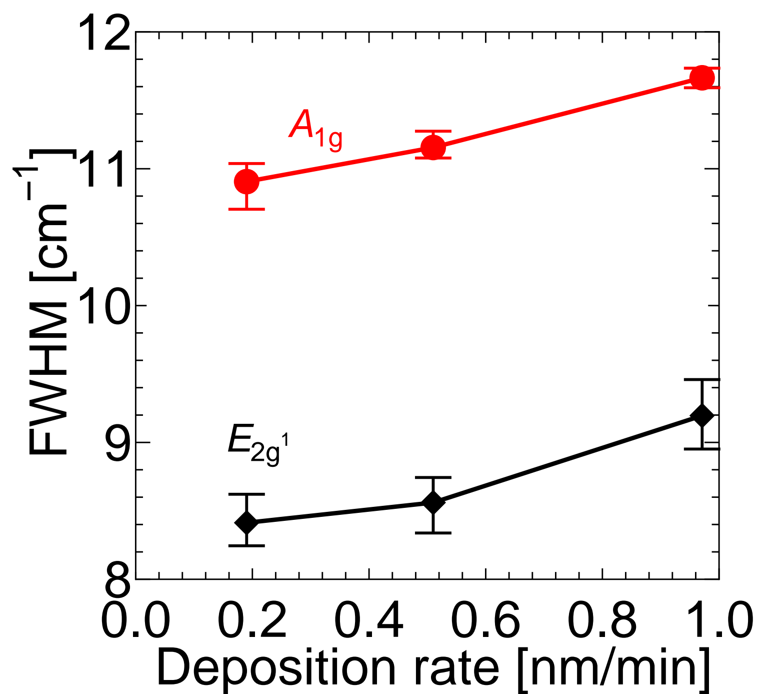


(b)

**Figure 6.5**: (a) Raman spectra of $MoS_2$ films prepared with different deposition rates. (b) FWHM values of the $A_{1g}$ and $E^1_{2g}$ peaks in five spectra for each wafer [41].

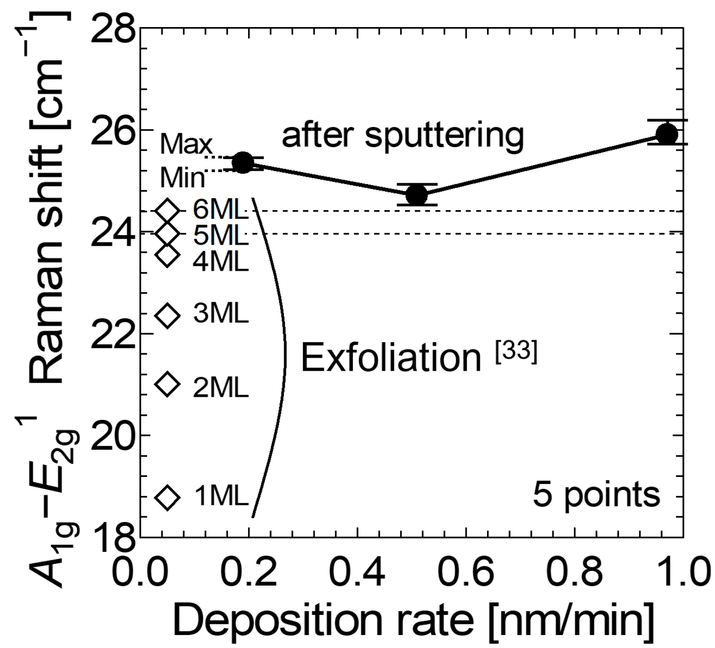


**Figure 6.6**: Deposition rate dependence of $A_{1g}$-$E_{2g}^1$ shift. Diamond data are those values for 1–6 monolayers (ML) exfoliated $MoS_2$ films [35].

it became clear that the film quality dependency of 5ML in this study leads to improved 1ML film quality.

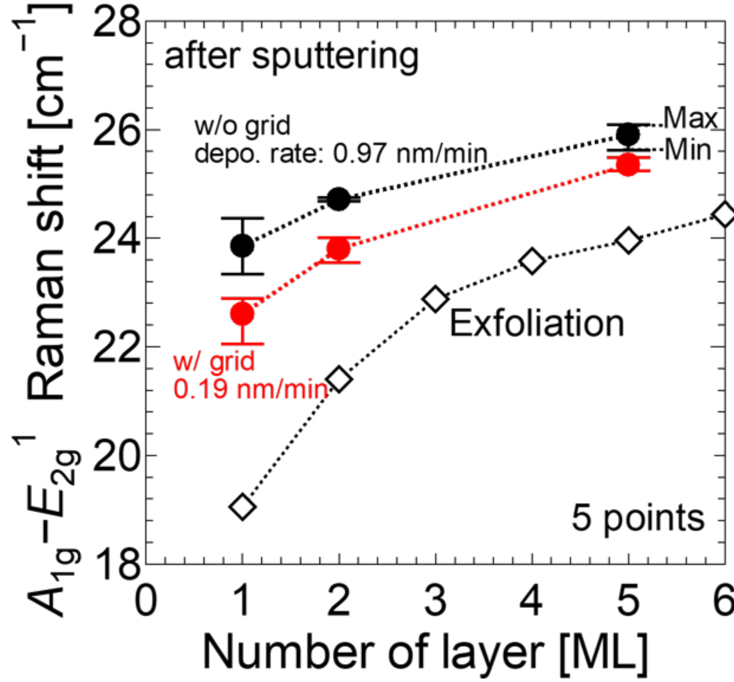


**Figure 6.7**: Layer number dependence of $A_{1g}$-$E^1_{2g}$ shift of $MoS_2$ film with and without grid. Diamond data are those values for 1–6 monolayers (ML) exfoliated $MoS_2$ films [35].

To assess the orientation of the $MoS_2$ films to the substrate surface, in-plane XRD measurements were performed. Figure 6.8 (a) shows the in-plane XRD patterns recorded with a wide range of $2\theta$. In-plane XRD can evaluate lattice planes perpendicular to the substrate surface instead of the out-of-plane ones. The XRD patterns of all the samples reveal peaks corresponding to the $MoS_2$ (100), (110), and (200) planes. However, it is noteworthy that the $MoS_2$ (002) plane is absent in this measurement, indicating no $MoS_2$ film aligned perpendicular to the substrate surface. It indicates that the $MoS_2$ layers are arranged in a mosaic fashion concerning the substrate surface. In addition, we also measured the in-plane XRD patterns with a narrow range around the (100) plane in Figure 6.8 (b) to estimate the crystallite size of the $MoS_2$ films. The crystallite size was calculated from the Scherrer equation [113]:

$$D_{100} = \frac{K_{100}\ \lambda}{B_{100}\ cos\theta}, \tag{6.3.1}$$

where the constant $K_{100}$ and the X-ray wavelength $\lambda$ are 0.890 and 0.154 nm, respectively. The FWHM values of $B_{100}$ and the Bragg angle $\theta$ were extracted from the peak of the $MoS_2$ (100) plane in Figure 6.8 (b). The estimated crystallite sizes of the $MoS_2$ films are shown in Figure 6.9. A decrease in the deposition rate leads to an increase of the $MoS_2$ crystallite size. We speculate that the frequency of particle collisions on the substrate was reduced, resulting in a lower nucleation density and, thus, an increase in the crystallite

size. We confirm that low-rate deposition enabled an enlargement of the $MoS_2$ crystallite size even in the films deposited by the sputtering method. These results support our results in enlarging the crystallite size by the low density of $MoS_2$ precursors and particles on the substrate.

In Figure 6.10, the crystal structure of $MoS_2$ films, deposited targeting the 1 ML under sputtering conditions having the largest grain size in Figure 6.9, was observed by a plan-view HAADF-STEM image. The crystal arrangement of Mo atoms can be seen in Figure 6.10 (b). In addition, the fast Fourier transform (FFT) image in the red-framed area in Figure 6.10 (a) shows the inverse pattern of $MoS_2$ single crystals, indicating the presence of $MoS_2$ crystals. Moreover, the most of the $MoS_2$ grains are observed as 1 ML, indicating the layer-by-layer growth of $MoS_2$ film. On the other hand, 0 ML regions and regions thicker than 1 ML are slightly observed. It suggests that the nucleation of the second layer begins with only low probability, even during the growth of the first layer. This speculation would be a key component to clarify the mechanism of layer-by-layer $MoS_2$ film formation.

ACOM-TEM analyses were conducted for the $MoS_2$ films to evaluate the crystal orientation distribution. Figures 6.11 (a) and (b) show the results of grain orientation mapping for 1-ML-$MoS_2$ films sputtered with a deposition rate of 0.97 and 0.19 nm/min, respectively. In both samples, the $MoS_2$ grains were randomly oriented. In addition, Figure 6.12 shows the histogram of grain size extracted from Figure 6.11.

Grains larger than 18 nm are observed only in the film deposited at a lower deposition rate of 0.19 nm/min, with the largest grain size reaching 26 nm. It suggests that large $MoS_2$ grains were formed because of the sputtering with a low particle flux. The grain size distribution of nano-particles can be approximated by a log-normal distribution function [127–129], expressed as:

$$f(x;\mu,\sigma) = \frac{A}{x\sqrt{2\pi}\sigma}\exp\left(-\frac{(\ln x-\mu)^2}{2\sigma^2}\right), \tag{6.3.2}$$

where $A$ is a constant, $\mu$ is the mean value of $\ln x$, and $\sigma$ is the standard deviation of $\ln x$. Figure 6.12 (b) shows the fitting results using the log-normal distribution function for the grain size histogram in Figure 6.12 (a). The average value and standard deviation of the log-normal distribution with and without a grid are calculated from the following equations with obtained fitting results, shown in Table 6.2,

$$\text{Average value} = \exp\left(\mu+\frac{\sigma^2}{2}\right), \tag{6.3.3}$$

$$\text{Standard deviation} = \exp\left(\mu+\frac{\sigma^2}{2}\right)\cdot\sqrt{\exp(\sigma^2)-1}. \tag{6.3.4}$$

It was confirmed that the average value increases with low particle flux deposition. On the other hand, the standard deviation increases, which indicates that large grain sizes are formed and that the distribution is broadened to the right. In addition, the values of $\mu-3\sigma$

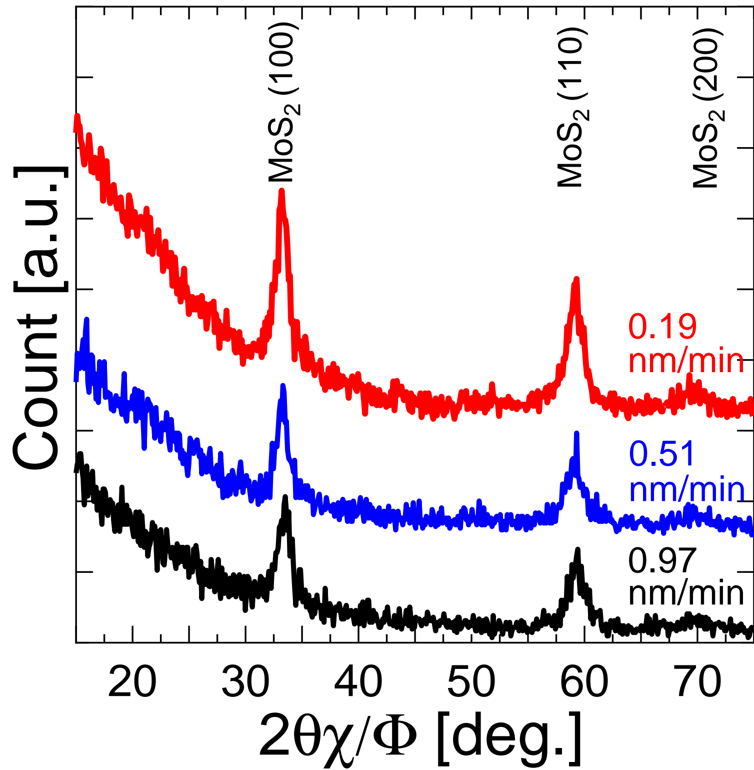


(a)

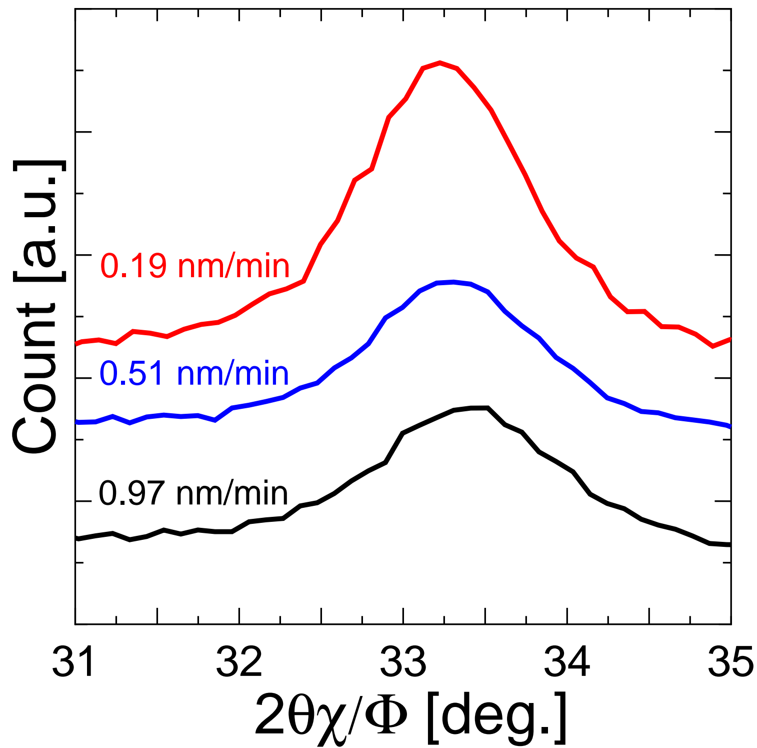


(b)

**Figure 6.8**: (a) Wide- and (b) narrow-range in-plane XRD patterns of $MoS_2$ films sputtered with different PA ratios [41].

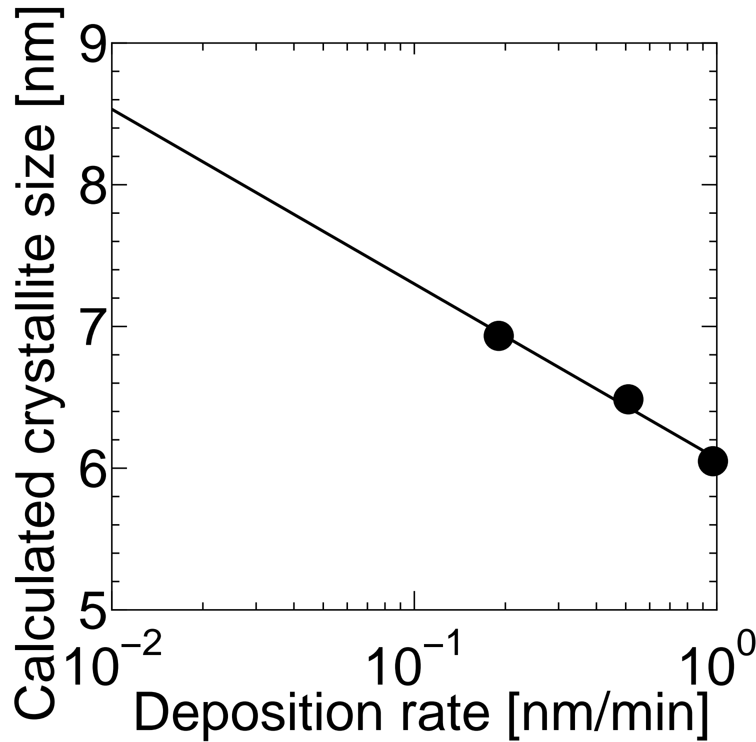


**Figure 6.9**: Calculated crystallite of $MoS_2$ films as function of deposition rate [41].

and $\mu - \sigma$ are shown in Table 6.2. Although these values are enhanced with lower particle flux, these are far from target value requiring further particle size increase in the future. Additionally, as shown in Figure 6.13, microcrystalline regions were also identified in the films, which is likely the cause of the significant variance and large standard deviation. These regions are hypothesized to act as nucleation points for forming the second layer, potentially influencing the overall film properties. Methods for removing microcrystalline regions are described in section 7.2.3. Although there are some differences in the growth processes between the 1-ML $MoS_2$ and 2.5 nm-thick $MoS_2$ films, the XRD and ACOM-TEM results are consistent with an increase in the average grain size due to the lower deposition rate. Therefore, the ACOM-TEM analyses with the 1ML-$MoS_2$ films on the TEM grids are considered effective methods for comparing the enlargement of grain size with a decrease in deposition rate, as well as the XRD measurement.

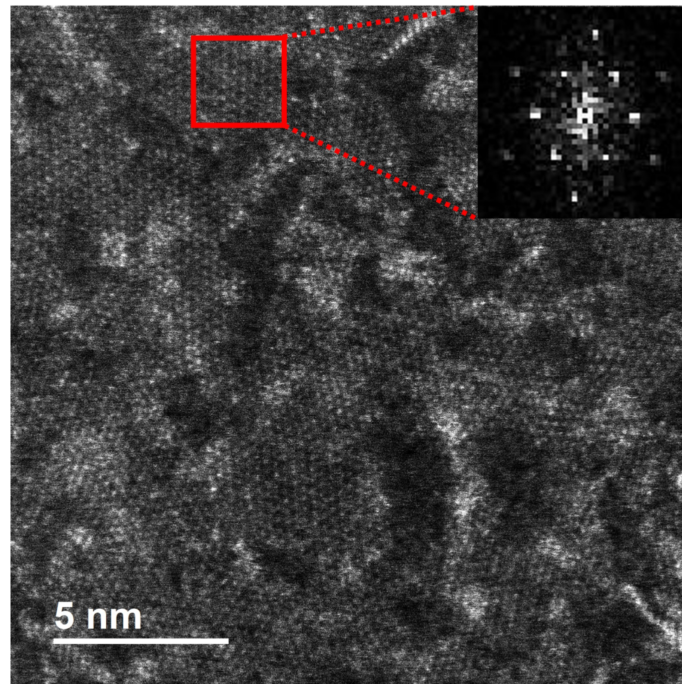


(a)

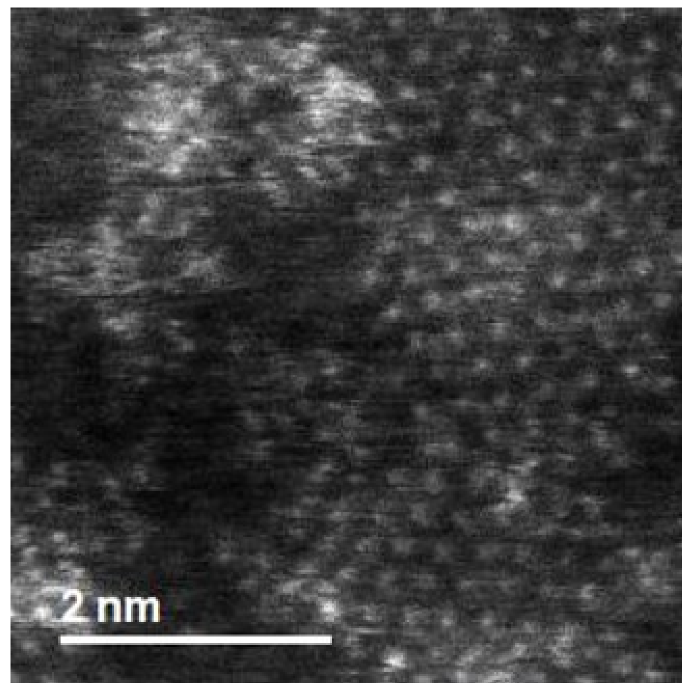


(b)

**Figure 6.10**: (a) Plan-view HAADF-STEM images of 1 monolayer (ML)-$MoS_2$ film prepared with $MoS_2$ deposition rate of 0.19 nm/min. 1ML-$MoS_2$ film was sputtered directly onto TEM grid that consisted of 20-nm-$SiO_x$ membrane. Inset in the upper right of (a) is fast Fourier transform (FFT) image of the red framed area. (b) Enlarged view of (a).

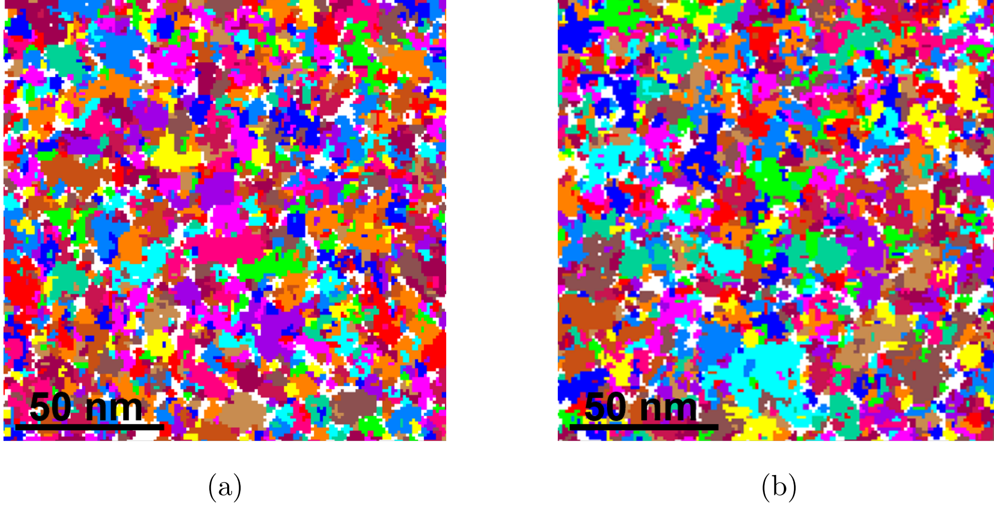


(a) (b)

**Figure 6.11**: ACOM-TEM grain orientation maps for 1-ML-$MoS_2$ films deposited at deposition rates of (a) 0.97 and (b) 0.19 nm/min, respectively.

**Table 6.2**: Comparison of average grain sizes and standard deviations with and without grid.

| | **Average value [nm]** | **Standard deviation [nm]** | $\mu - 3\sigma$ **[nm] (in real space)** | $\mu - \sigma$ **[nm] (in real space)** |
|---|---|---|---|---|
| Without grid (0.97 nm/min) | **7.9** | **7.0** | 0.6 | 2.7 |
| With grid (0.19 nm/min) | **9.1** | **7.9** | 0.7 | 3.2 |

**Target grain size: 7.9 nm**

Based on these results, we speculate that the sputtering with further suppression of the particle flux leads to a further enhancement of the $MoS_2$ grain size. Although low-power sputtering is an alternative method to achieve the low-rate deposition, the previous study reported that the sputtered particles have less energy for the formation energy of $MoS_2$ film, degrading the quality of the resultant $MoS_2$ film in chapter 5. Therefore, low-particle flux sputtering using a Mo grid is a promising method to enhance the $MoS_2$ grain size without suppressing the particle energy. Although the 9.1 nm-grain size of $MoS_2$ films with a substrate temperature of 300°C in this study is smaller than the 10 $\mu$m-grain size obtained by high-temperature CVD methods at 1000°C [124], the improved $MoS_2$ film in this study will provide a low-temperature channel deposition method with bottom-up integration for advanced VLSI and human interface devices.

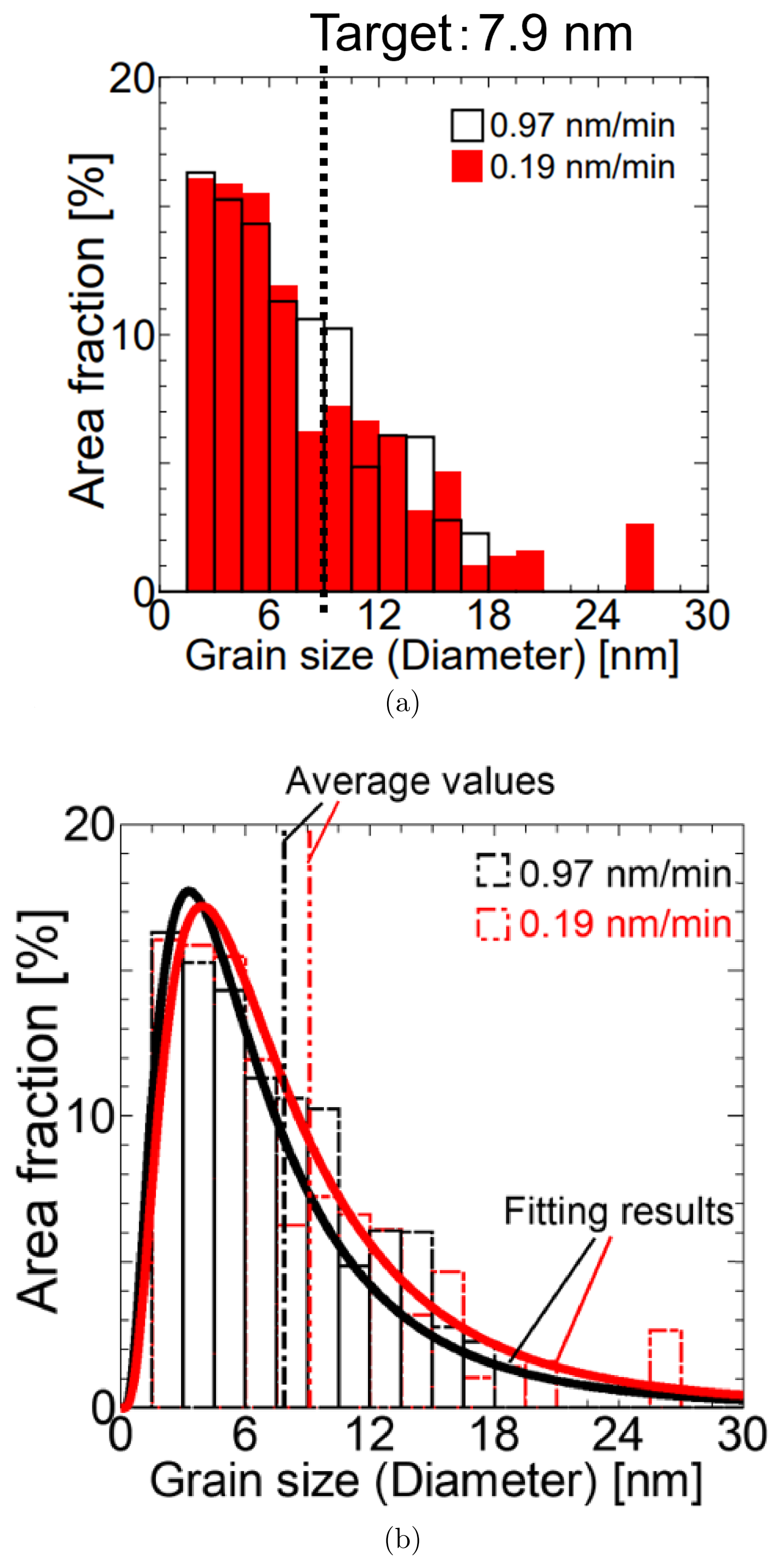


(a)

(b)

**Figure 6.12**: (a) Grain size histogram of $MoS_2$ films, as calculated from the results in Figure 6.11. (b) Fitting results using log-normal distribution function for (a).

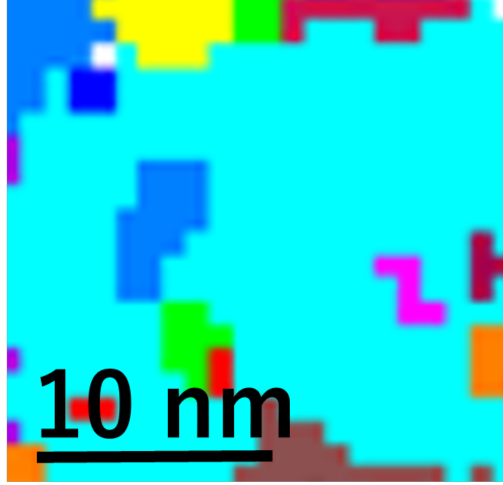


**Figure 6.13**: Enlarged grain grain orientation map for 1-ML-$MoS_2$ films deposited at deposition rates of 0.19 nm/min.

As shown in Figure 6.14 (a), the sulfur defect density of the $MoS_2$ film with the largest crystal size formed in this study was extracted from Figure 6.14 (b). Assuming that the literature value (1ML) is $V_s = 0\%$ [35], we extract the difference value $\Delta(A_{1g}\text{-}E^1_{2g})$ between the ($A_{1g}$-$E^1_{2g}$ shift) of the prepared sample (red circle) and the literature value. In the $MoS_2$ film with the largest crystals, the sulfur defect density ($V_s$) was ˜1.65%. The mobility degradation in $MoS_2$ films can be expressed as:

$$\frac{1}{\mu_{\text{MoS}_2}} = \frac{1}{\mu_{\text{imp}}} + \frac{1}{\mu_{\text{ph}}} + \frac{1}{\mu_{\text{rough}}} + \frac{1}{\mu_{\text{vacancy}}} + \frac{1}{\mu_{\text{GBs}}} + \frac{1}{\mu_{\text{anti-site}}} + \dots \tag{6.3.5}$$

where $\mu_{\text{imp}}$ is impurity scattering, $\mu_{\text{ph}}$ is phonon scattering, $\mu_{\text{rough}}$ is roughness scattering, $\mu_{\text{vacancy}}$ is scattering due to sulfur vacancies, $\mu_{\text{GBs}}$ is grain boundary scattering, and $\mu_{\text{anti-site}}$ is anti-site scattering. The primary factors contributing to mobility degradation in fabricated $MoS_2$ films are sulfur vacancy scattering and grain boundary-related scattering [98]. In future short-channel devices, grain-free regions are desirable. In this study, the mobility was calculated considering only the sulfur vacancy scattering within a single grain. Using the relationship between sulfur defect density and carrier mobility [130], as shown in Figure 6.15, the calculated mobility is approximately 26.5 $cm^2/Vs$. The crystal or grain size and mobility for various formation methods are compared from Table 6.3. Further reduction in the sulfur vacancy density is required to reach the target value of 183 $cm^2/Vs$. In addition, because the decrease in the sulfur vacancy density at 300°C was demonstrated, this low particle flux deposition is expected to be used in industrial applications in the future.

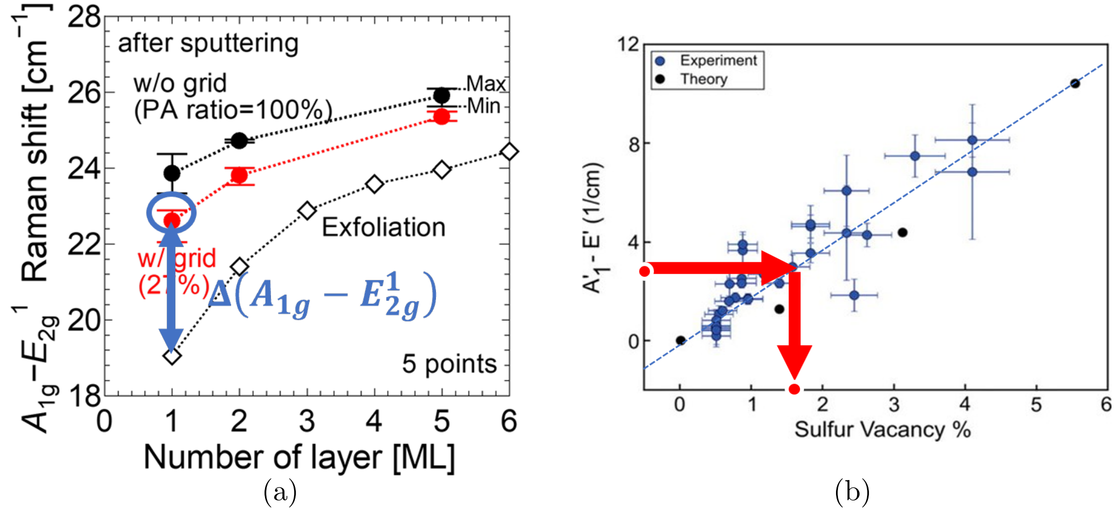

(a) (b)

**Figure 6.14**: (a) $A_{1g}$-$E^1_{2g}$ shift value of $MoS_2$ film with largest grain size deposited in this study. $\Delta(A_{1g}$-$E^1_{2g})$ is equal to the difference between ($A_{1g}$-$E^1_{2g}$) shift values of the $MoS_2$ film and that with $V_s$ of 0%. (b) Dependence of $\Delta(A_{1g}$-$E^1_{2g})$ Raman shift values on sulfur defect density ($V_s$) in $MoS_2$ film [42].

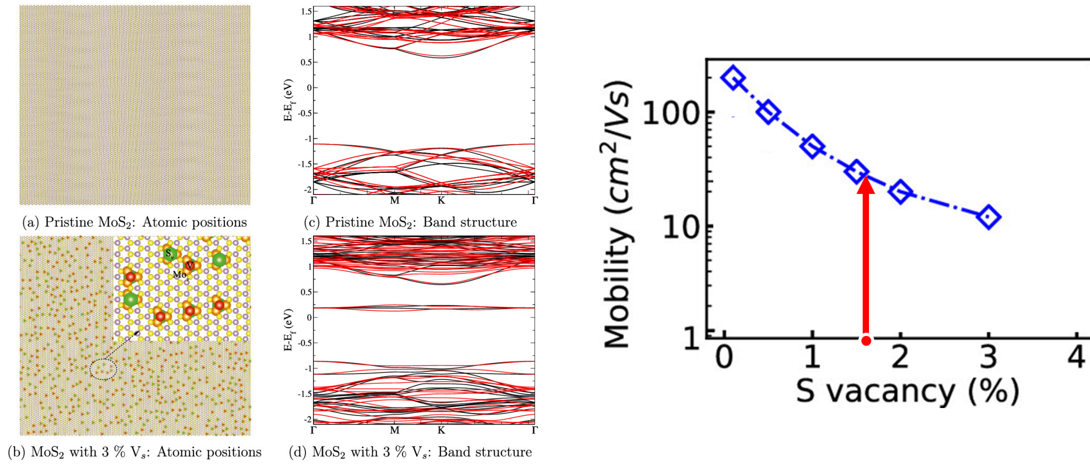


**Figure 6.15**: (a) Atomic positions of monolayer $MoS_2$ with no sulfur vacancies and with 3% sulfur vacancies. Sulfur and molybdenum atoms are magnified to represent their distribution. The band structure obtained using DFT is shown, respectively [29]. (b) Previous research of calculated carrier mobility depending on sulfur defect density [29].

**Table 6.3**: Comparison of grain size and mobility for various formation methods.

| **Formation Method** | **Grain Size** | **Mobility [$cm^2$/Vs]** | **Reference** |
|---|---|---|---|
| This work sputtering | **Max 26, AVE. 9.1 nm (Crystalline size 7.0 nm)** | **26.5 (Calculated)** | Sputtering (300°C), without GBs |
| Sputtering + S-annealing (700°C) | NA | 0.21 ($\mu_F$) | [21] |
| Exfoliation | ~30 $\mu$m | 700 | [68] |
| Exfoliation on PMMA | ~20 $\mu$m | 30–60 | [70] |
| CVD Sulfur+$MoO_3$ | ~2 $\mu$m | ~17 | [70] |
| CVD monolayer Sulfur +$MoO_3$ | ~2 $\mu$m | 24 | [71] |

## 6.4 Summary

The results demonstrated that reducing the deposition rate effectively increased the grain size of the $MoS_2$ films. The use of low particle flux during the deposition process significantly lowered the nucleation density, allowing for the growth of grains with larger dimensions. The maximum grain size achieved under these conditions was 26 nm, highlighting the potential of this method for enhancing the crystalline structure of $MoS_2$ films. However, several challenges remain to be addressed. One of the primary issues is the presence of microcrystalline $MoS_2$ regions within the films, which need to be removed to achieve uniformity. Another issue is the increase in sulfur vacancy density caused by the limited sulfur supply during the sputtering process. To overcome this, future investigations should optimize the sputtering parameters to enhance the sulfur supply, thereby mitigating sulfur deficiencies and improving film quality.

# Chapter 7

# Conclusions

## 7.1 Conclusions of this thesis

This study proposes a sputtering method to obtain high-quality $MoS_2$ films expected to be used as channel materials for next-generation 3D stacked logic.

Chapter 1 shows that low-temperature deposition of $MoS_2$ films by sputtering is possible. It also clarifies the problems of high sulfur defect density and small crystal size, which reduce the carrier mobility of $MoS_2$ films. The purpose of this study is also presented.

Chapter 2 sets target values for formation temperature, crystal size, and sulfur defect density to clarify the goal of improving the film quality of $MoS_2$ films deposited by sputtering.

Chapter 3 verified the mechanism of sputtering deposition to reach the $MoS_2$ film goal set in Chapter 2 and showed the direction of specific deposition techniques. It expressly specified how to enlarge the surface migration length on the substrate surface to increase the crystal size and enhance the amount of S supply to reduce the sulfur defect density by changing the parameters during sputtering.

Chapter 4 adjusted the substrate temperature to increase the particle surface migration length. As a result, the appropriate substrate temperature was 300°C, and by setting this temperature, a good $MoS_2$ film was obtained that suppressed the sulfur defect density while promoting particle surface migration. In addition, in this Chapter, sulfur compensation annealing at 700°C was also performed on the sputtered film, and the film's quality dependency after annealing was also clarified. In the future, improving the $MoS_2$ film quality will be essential immediately after sputtering.

In Chapter 5, varying the RF power was performed to adjust the flux temperature ($T_{\text{flux}}$), the temperature of the particles that reach the substrate, and the particle flux, which is a factor in increasing the particle surface migration length. At intermediate RF power, it was confirmed that the surface migration length of the particles on the substrate can be increased by suppressing the particle flux and providing sufficient flux temperature. Furthermore, it was shown that the increase in the amount of S flux by increasing the RF power leads to the acquisition of $MoS_2$ films with low sulfur defect density.

In Chapter 6, it was demonstrated that low particle flux film formation can be achieved

by introducing a grid between the target and substrate of the sputtering device. As a result, it was confirmed that the low particle flux reduces the nucleation density, increases the particle migration length on the substrate, and increases the crystal size of the $MoS_2$ film.

This Chapter summarizes the results of crystal size and sulfur vacancies in $MoS_2$ film. The above results and discussion conclude that the factor that increases the crystal size of $MoS_2$ films is to improve the surface migration length of particles on the substrate. There are three ways to increase this migration length: appropriate substrate temperature, sufficient flux temperature, and low particle flux. Also, to suppress the sulfur defect density, it is necessary to adjust the sputtering parameters to increase the sulfur/molybdenum flux supply ratio. Specifically, high RF power, short T-S distance, and low Ar pressure. On the other hand, this direction causes an increase in particle flux to the substrate. By reducing the particle flux by the grid under those conditions, obtaining $MoS_2$ films with low sulfur defect density and increased crystal size became possible. Moreover, Figure 7.1 shows the average grain or crystallite size versus deposition temperature for $MoS_2$ films. In FEOL, intermediate RF power adjustments increase the crystallite size, but the target value is not reached (below 7.9 nm). In BEOL, low particle flux sputtering further enhances the crystallite size, reaching the target value (above 7.9 nm). Moreover, Figure 7.2 shows the benchmark of crystal size dependence on deposition temperature. Although it is considered that there is an exponential dependence between substrate temperature and crystal size, the maximum grain size reaches 26 nm with low particle flux deposition at a formation temperature of 300°C, which applies to FEOL and BEOL. Larger crystals are obtained at lower temperatures than with other deposition techniques. Although the $MoS_2$ film deposited in this study achieved low particle flux deposition, the deposition time was approximately 1 min/layer, which is much shorter than the deposition time of 1 hour/min for $MoS_2$ films deposited by chemical vapor deposition (CVD) or atomic layer deposition (ALD) [63]. The advantages of low particle flux sputtering over other deposition techniques are demonstrated.

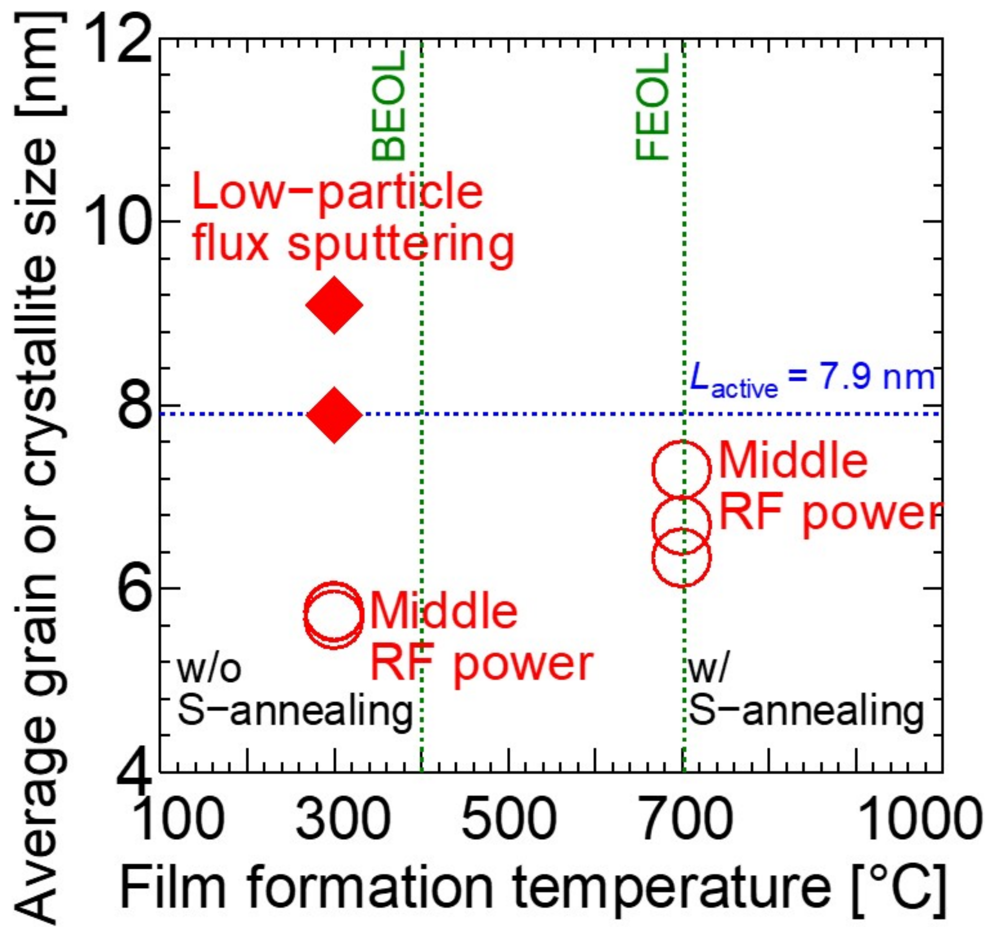


**Figure 7.1**: Average grain or crystallite size depending on formation temperature of $MoS_2$ film.

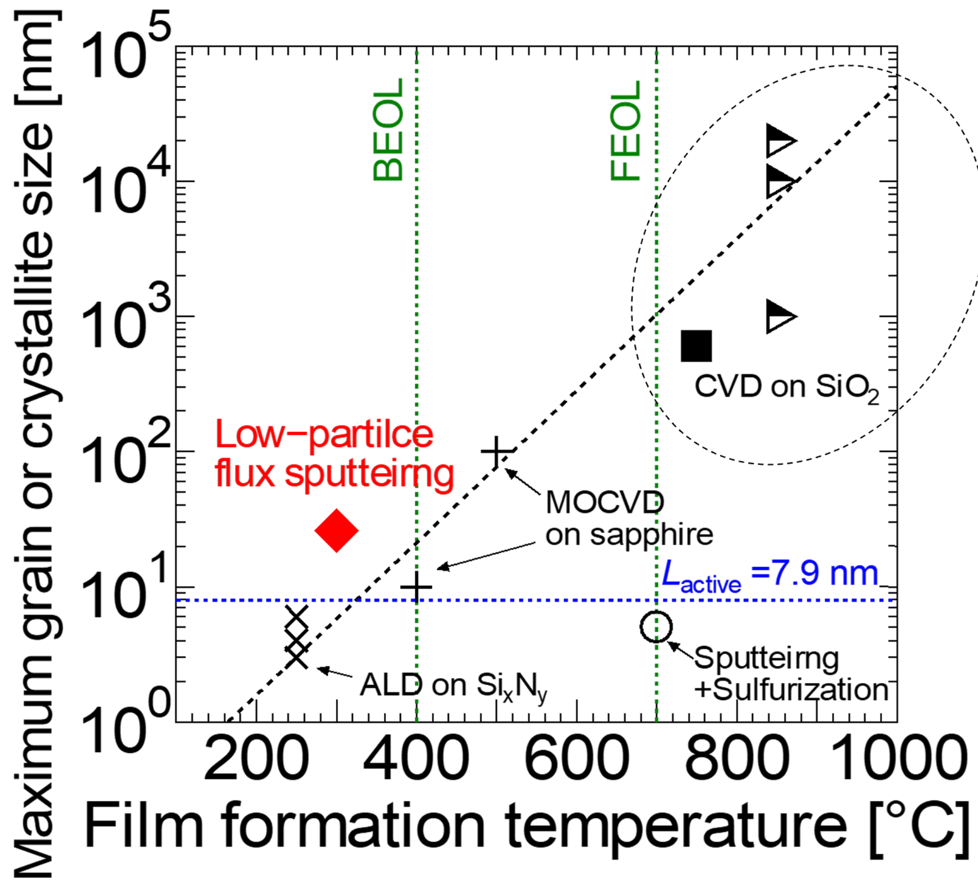


**Figure 7.2**: Benchmark: Dependence of grain or crystallite size on formation temperature of the $MoS_2$ film.

## 7.2 Future directions

### 7.2.1 Optimizing the sputtering Ar pressure

Figure 7.3 shows the Ar pressure dependence of the $A_{1g}$-$E^1_{2g}$ Raman shift of $MoS_2$ film after sputtering. In this study, as the minimum pressure (0.4 Pa) at which plasma can be generated decreased, the $A_{1g}$-$E^1_{2g}$ shift decreased and approached the ideal value, which is thought to be the effect of increasing the S/Mo supply ratio due to the low pressure. In addition, since damage to graphene films due to high-energy recoil argon at low pressure has been reported shown in Figure 7.4 [43], further reduction in pressure may damage the $MoS_2$ film itself. Therefore, it is necessary to investigate the optimal pressure value in the future, as illustrated in Figure 7.5.

**Figure 7.3**: $A_{1g}$-$E^1_{2g}$ Raman shift dependence on Ar pressure.

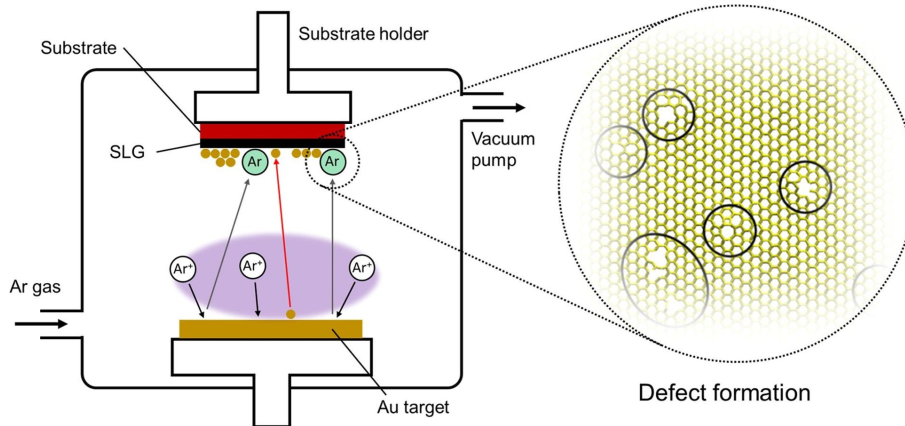


**Figure 7.4**: Model of damage formation in graphene nanosheet caused by recoil argon during low-pressure sputtering [43].

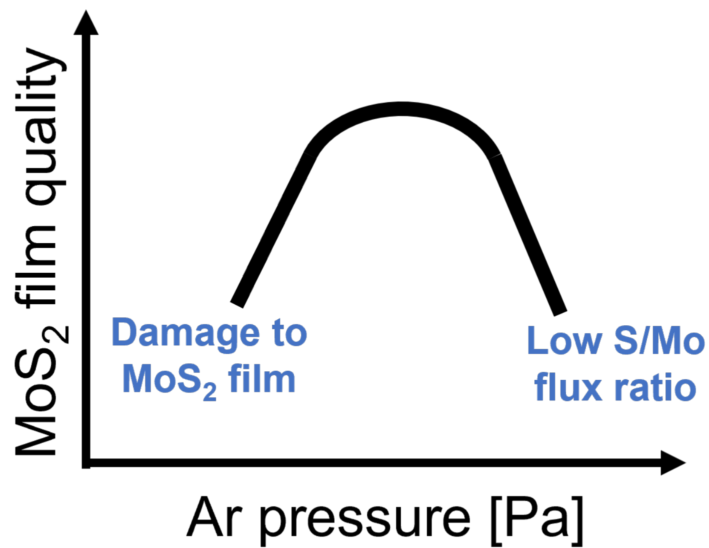


**Figure 7.5**: Schematic of improving $MoS_2$ film quality by optimizing Ar pressure during sputtering.

### 7.2.2 Removal of small $MoS_2$ crystal using area selective etching

As shown in Figure 6.13, microcrystalline regions were identified and are assumed to be the nucleation points for the second layer, which reduces the grain size in $MoS_2$ film. It has been reported that removing microcrystalline regions by atomic layer etching (ALE) treatment with $Cl_2$ gas, as shown in Figure 7.6 [44]. Therefore, this ALE method leads to removing the microcrystalline and further enhancing the grain size in $MoS_2$ film deposited by sputtering.

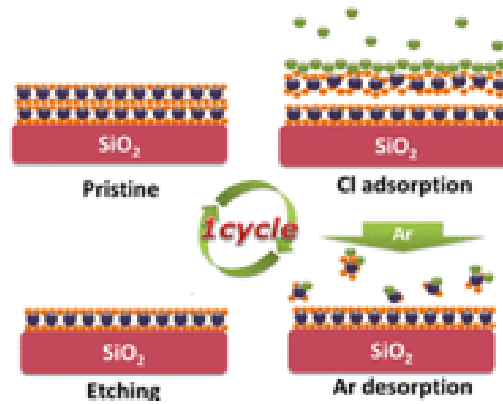


**Figure 7.6**: Schematics of atomic layer etching (ALE) for $MoS_2$ microcrystalline using $Cl_2$ gas [44].

### 7.2.3 Area selective deposition for single crystal $MoS_2$

This study explored the optimal conditions for sputtering deposition of amorphous $SiO_2$-like $MoS_2$ films. In the future, it will be necessary to aim for further improvement in grain size. Enlarging the grain size by using a lower particle flux is needed. Furthermore, by adopting an underlayer such as hexagonal boron nitride (hBN), the grain size is expected to increase from van der Waals epitaxial growth [131]. Furthermore, attention is being paid to area selective deposition (ASD) to improve yield. By growing single crystals of $MoS_2$ film only in the channel region in this way, it is expected that the electrical properties of sputtered $MoS_2$ films can be significantly improved [45, 46]. In the future, it is necessary to advance research on $MoS_2$ films by this selective growth.

### 7.2.4 Approach for further improvement of high-quality $MoS_2$ films

To achieve a large crystal size with a low sulfur vacancy density, the sputtering process must be optimized. Figure 7.8 demonstrates the relationship between crystal size and $A_{1g}$-

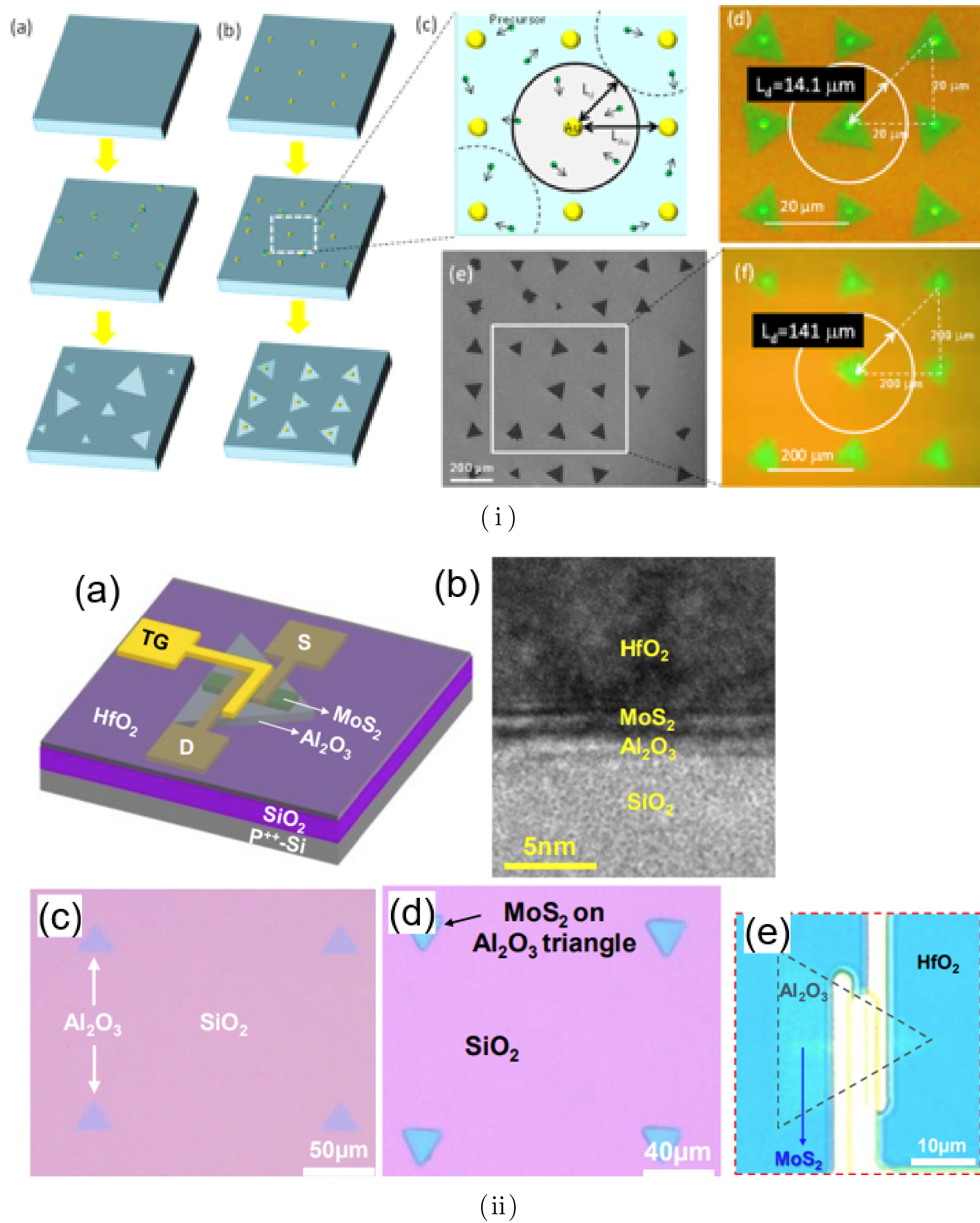


**Figure 7.7**: Previous research on selective area deposition (SAD). ( i ) Selective nucleation growth of $MoS_2$ from Au electrode edges [45]. (ii) van der Waals epitaxial growth of $MoS_2$ from sapphire substrate with selected areas [46].

$E^1_{2g}$ Raman shift under different process conditions. The graph indicates the effect of RF power, where middle-range power resulted in an optimal balance between particle flux and sulfur supply. A high sulfur flux combined with a low particle flux to the substrate surface was essential for increasing grain size while reducing the $A_{1g}$-$E^1_{2g}$ shift, which minimized sulfur vacancies.

The process conditions required for achieving this optimization are illustrated schematically in Figure 7.9. At a substrate temperature ($T_{\mathrm{sub.}}$) of 300° C, sufficient flux temperature ($T_{\mathrm{flux}}$) and low particle flux are necessary to achieve a high particle temperature ($T_{\mathrm{particle}}$) and maintain a high sulfur flux. These conditions promote the reduction of sulfur vacancy density and ensure the growth of large crystalline grains.

The conclusion drawn from this study confirms that achieving large crystalline grains requires high flux temperatures ($T_{\mathrm{flux}}$) and low particle flux during sputtering. For future work, further reduction of sulfur vacancies can be addressed by increasing the sulfur supply using alternative approaches such as $MoS_4$ target sputtering or $H_2S$ gas sputtering.

This work is expected to lead to the development of 3D-stacked FETs (3SDFETs) with the PVD-$MoS_2$ film.

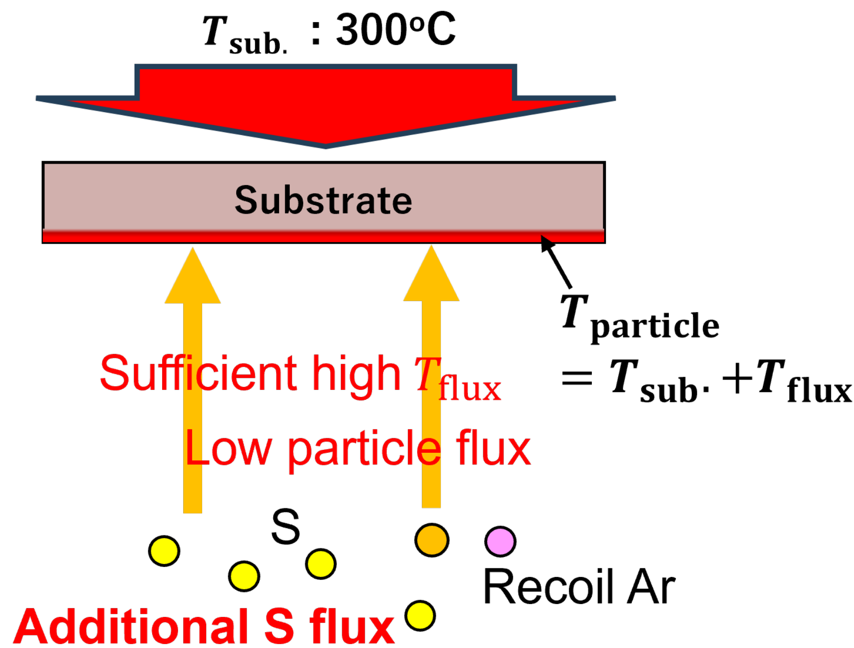


**Figure 7.9**: Approaches to achieving higher-quality $MoS_2$ films by extending the surface migration length of sputtered particles and supplying additional sulfur flux during sputtering.

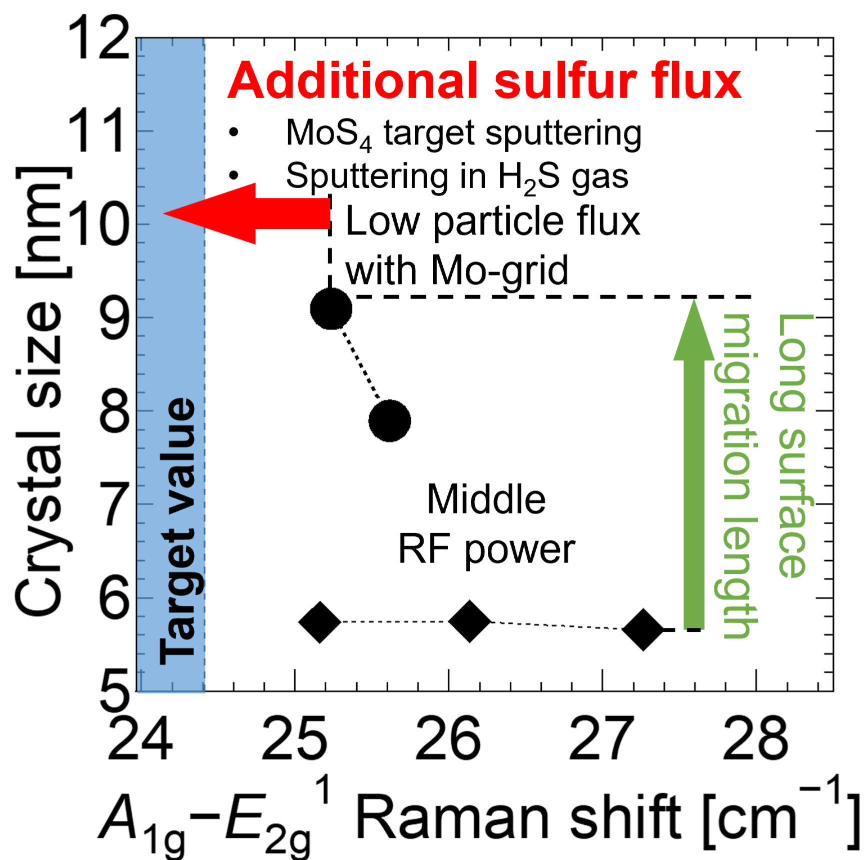


**Figure 7.8**: Summary of crystal size as function of the $A_{1g}$-$E^1_{2g}$ Raman shift in the $MoS_2$ film deposited by sputtering in this study. A small $A_{1g}$-$E^1_{2g}$ Raman shift indicates a low sulfur defect density.

# Publications and presentations

**International Journals with review (first Author);**

1. S. Imai, T. Hamada, M. Hamada, T. Shirokura, I. Muneta, K. Kakushima, T. Tatsumi, S. Tomiya, K. Tsutsui and H. Wakabayashi, “Importance of crystallinity improvement in $MoS_2$ film by compound sputtering even followed by post sulfurization,” *Japanese Journal of Applied Physics (JJAP),* vol. 60, no. SB, p. SBBH10, 2021, DOI: 10.35848/1347-4065/abdcae.

2. S. Imai, T. Tatsumi, S. Tomiya, K. Kakushima and H. Wakabayashi, “Improvement of $MoS_2$ film quality using sputtering processes controlling particle- and energy-flux followed by sulfur-vapor annealing,” *Japanese Journal of Applied Physics (JJAP),* vol. 64, no. 021001, 2025, DOI: 10.35848/1347-4065/ada9df.

3. S. Imai, R. Ono, I. Muneta, K. Kakushima, T. Tatsumi, S. Tomiya, K. Tsutsui and H. Wakabayashi, “Improvement of $MoS_2$ Film Quality by Low Flux of Sputtered Particles using a Molybdenum Grid,” *IEEE Journal of the Electron Devices Society (J-EDS),* vol. 13, pp. 15-23, 2025, DOI: 10.1109/JEDS.2024.3502922.

**International journals (co-author);**

1. R. Ono, S. Imai, Y. Kusama, T. Hamada, M. Hamada, I. Muneta, K. Kakushima, K. Tsutsui, E. Kano, N. Ikarashi and H. Wakabayashi, “Elucidation of PVD $MoS_2$ film formation process and its structure focusing on sub-monolayer region,” *Japanese Journal of Applied Physics (JJAP),* 61.SC, SC1023, 2022.

2. M. Fukawa, X. Deng, S. Imai, T. Horiguchi, R. Ono, I. Rachi, S. A, K. Shinomura, S. Niwa, T. Kudo, H. Ito, H. Wakabayashi, Y. Miyake and A. Hori, “A Novel Method for Lightning Prediction by Direct Electric Field Measurements at the Ground Using Recurrent Neural Network,” *IEICE TRANSACTIONS on Information and Systems,* vol. 105.9, pp. 1624–1628, 2022.

3. T. Kitazawa, Y. Inaba, S. Yamashita, S. Imai, K. Kurohara, T. Tatsumi, H. Wakabayashi and S. Tomiya, “Impact of crystallinity on thermal conductivity of RF magnetron sputtered $MoS_2$ thin films,” *Japanese Journal of Applied Physics,* vol. 63, no. 5 (2024): 055508.

4. K. Kurohara, S. Imai, T. Hamada, T. Tatsumi, S. Tomiya, K. Kakushima, K. Tsutsui and H. Wakabayashi, “Conductivity Enhancement of PVD-$WS_2$ Films Using $Cl_2$-Plasma Treatment Followed by Sulfur-Vapor Annealing,” *IEEE Journal of the Electron Devices Society (J-EDS),* vol. 12, pp. 390-398, 2024.

5. N. Matsunaga, S. Imai, T. Shirokura, Y. Mochizuki, K. Kuwahata, K. Tsutsui, K. Kakushima and H. Wakabayashi, “Impact of Underlying Insulators on the Crystallinity and Antisite Defect Formation in PVD-$MoS_2$ Films,” *IEEE Journal of the Electron Devices Society (J-EDS),* 2024.

6. S. Ito, K. Teraoka, S. Imai, N. Matsunaga, J. Jang, I. Muneta, K. Kakushima and H. Wakabayashi, “Crystallinity improvement of physical-vapor-deposited $WS_2$ films by controlling particle energy,” *Japanese Journal of Applied Physics (JJAP),* vol. 64, no. 02SP08, 2024.

7. K. Teraoka, S. Imai, N. Matsunaga, K. Kurohara, S. Ito, K. Kakushima and H. Wakabayashi, “$WS_2$-contact resistance reduction to nickel by $Al_2O_3$ insertion,” *Japanese Journal of Applied Physics (JJAP),* vol. 63 no. 12SP23, 2024.

**International conference;**

1. S. Imai, T. Hamada, M. Hamada, T. Shirokura, I. Muneta, K. Kakushima, T. Tatsumi, S. Tomiya, K. Tsutsui, and H. Wakabayashi, “Importance of $MoS_2$-Compound Sputtering even with Sulfur-Vapor Anneal for Chip-Size Fabrication,” *Solid State Devices and Materials (SSDM),* p. 503, H-2-03, Hokkaido, Japan (Online), Sep. 2020.

2. S. Imai, R. Ono, I. Muneta, K. Kakushima, T. Tatsumi, S. Tomiya, K. Tsutsui and H. Wakabayashi, “Grain-Size Enlargement of $MoS_2$ Film by Low-Rate Sputtering with Molybdenum Grid,” *2023 7th IEEE Electron Devices Technology and Manufacturing Conference (EDTM),* pp. 1–3, Seoul, Korea, Mar. 2023.

3. S. Imai, T. Tatsumi, S. Tomiya, K. Kurohara and H. Wakabayashi, “Improvement of $MoS_2$ Film Quality controlling High-energy Particle Flux during RF Magnetron Sputtering,” *44th International Symposium on Dry Process (DPS2023),* D-4, Nagoya, Japan, Nov. 2023.

4. S. Imai, R. Kajikawa, T. Kawanago, I. Muneta, K. Tsutsui, T. Tatsumi, S. Tomiya, K. Kakushima and H. Wakabayashi, “Reduction of contact resistance to PVD-$MoS_2$ film using aluminum–scandium alloy (AlSc) edge contact,” *2024 8th IEEE Electron Devices Technology and Manufacturing Conference (EDTM),* 4D-4, Bangalore, India, Mar. 2024.

5. (Invited) S. Imai, T. Tatsumi, S. Tomiya, K. Kakushima and H. Wakabayashi, "High Crystallinity of $MoS_2$ Film by Annealing in Sulfur Atmosphere and Plasma Control during RF Sputtering," *ECS PRiME 2024,* Hawaii, United States, Oct. 8, 2024.

**Domestic conference;**

1. S. Imai, M. Hamada, S. Igarashi, I. Muneta, K. Kakushima, K. Tsutsui and H. Wakabayashi, "Importance of Improving Sputtered-$MoS_2$ Film Quality in Sulfurization Process," *80th Japan Society of Applied Physics (JSAP),* no. 19p-E308-7, Hokkaido, Japan, Thursday 19 Sep. 2019.

2. S. Imai, R. Ono, I. Muneta, K. Kakushima, T. Tatsumi, S. Tomiya, K. Tsutsui and H. Wakabayashi, "Research on sputter deposition rate dependence of $MoS_2$ film quality," *83th Japan Society of Applied Physics (JSAP),* no. 21a-C202-11, Miyagi, Japan, Wednesday 21 Sep. 2022.

3. S. Imai, R. Kajikawa, T. Kawanago, I. Muneta, K. Kakushima, T. Tatsumi, S. Tomiya, K. Tsutsui and H. Wakabayashi, "Current-Voltage Characteristics of Edge Metal Contact for $MoS_2$ Film Formed by Sputtering,"*84th Japan Society of Applied Physics (JSAP),* no. 22a-A202-9, Kumamoto, Japan, Friday 22 Sep. 2023.

4. S. Imai, I. Muneta, T. Kawanago, K. Kakushima, T. Tatsumi, S. Tomiya and H. Wakabayashi, "Analysis of plane-view transmission electron microscopy image for $MoS_2$ film by sputtering on amorphous $SiO_2$," *71th Japan Society of Applied Physics (JSAP),* Spring meeting, Tokyo, Mar. 2024.

5. S. Imai, I. Muneta, K. Kakushima, T. Tatsumi, S. Tomiya and H. Wakabayashi, "Low-particle-flux sputtering of thin $MoS_2$ film at low temperature," *72th Japan Society of Applied Physics (JSAP),* Spring meeting, Chiba, Mar. 2024.

# References

[1] E. Masanet, A. Shehabi, N. Lei, S. Smith, and J. Koomey, "Recalibrating global data center energy-use estimates," *Science*, vol. 367, no. 6481, pp. 984–986, 2020.

[2] J. Li, Y. Liang, and L. Liu, "[retracted] research on the optimization art design of internet smart home system based on the new era," *Security and Communication Networks*, vol. 2022, no. 1, p. 1031682, 2022.

[3] A. Khan, H. J. Yoo, S. L. Shinde, and P. V. Ravindran, "Materials opportunities for low-energy computing," *MRS Bulletin*, pp. 1–5, 2021.

[4] R. H. Dennard, F. H. Gaensslen, H.-N. Yu, V. L. Rideovt, E. Bassous, and A. R. Leblanc, "Design of ion-implanted MOSFET's with very small physical dimensions," *IEEE Solid-State Circuits Society Newsletter*, vol. 12, no. 1, pp. 38–50, 2007.

[5] T. Hiramoto, "Never-Ending CMOS Innovation: The Past, Present, and Future Perspectives," in *2020 International Symposium on VLSI Technology, Systems and Applications (VLSI-TSA)*, pp. 3–4, IEEE, 2020.

[6] R. Xie, P. Montanini, K. Akarvardar, N. Tripathi, B. Haran, S. Johnson, T. Hook, B. Hamieh, D. Corliss, J. Wang, *et al.*, "A 7 nm FinFET Technology Featuring EUV Patterning and Dual Strained High Mobility Channels," in *2016 IEEE international electron devices meeting (IEDM)*, pp. 2–7, IEEE, 2016.

[7] Y. Lee, M. Na, A. Chu, A. Young, T. Hook, L. Liebmann, E. Nowak, S. Baek, R. Sengupta, H. Trombley, *et al.*, "Accurate performance evaluation for the horizontal nanosheet standard-cell design space beyond 7 nm technology," in *2017 IEEE International Electron Devices Meeting (IEDM)*, pp. 29–3, IEEE, 2017.

[8] J. Park, W. Kim, S. Park, J. Yun, K. Hwang, J. Yang, D. Kim, J. W. Jeong, C. Yun, J. Bae, *et al.*, "First demonstration of 3-dimensional stacked FET with top/bottom source-drain isolation and stacked n/p metal gate," in *2023 International Electron Devices Meeting (IEDM)*, pp. 1–4, IEEE, 2023.

[9] J. Park, J. Park, J. Park, K. Hwang, J. Yun, D. Kim, S. Park, J. Yang, J. W. Jeong, C. Yun, *et al.*, "Realization of cmos operation in 3-dimensional stacked fet with self-aligned direct backside contact," *Japanese Journal of Applied Physics*, vol. 63, no. 12, p. 120803, 2024.

[10] E. Anju, I. Muneta, K. Kakushima, K. Tsutsui, and H. Wakabayashi, "Relaxation of self-heating-effect for stacked-nanowire FET and p/n-stacked 6T-SRAM layout," *IEEE Journal of the Electron Devices Society*, vol. 6, pp. 1239–1245, 2018.

[11] H. Wakabayashi, "TMDC Channel for Low-power-density 3D-stacked FETs," in *2024 8th IEEE Electron Devices Technology and Manufacturing Conference (EDTM)*, vol. 4D-1, IEEE, 2024.

[12] B. Radisavljevic, A. Radenovic, J. Brivio, V. Giacometti, and A. Kis, "Single-layer $MoS_2$ transistors," *Nature nanotechnology*, vol. 6, no. 3, pp. 147–150, 2011.

[13] D. Akinwande, C. Huyghebaert, C.-H. Wang, M. I. Serna, S. Goossens, L.-J. Li, H.-S. P. Wong, and F. H. Koppens, "Graphene and two-dimensional materials for silicon technology," *Nature*, vol. 573, no. 7775, pp. 507–518, 2019.

[14] Y. Guo and J. Robertson, "Band engineering in transition metal dichalcogenides: Stacked versus lateral heterostructures," *Applied physics letters*, vol. 108, no. 23, 2016.

[15] Y. Liu, X. Duan, H.-J. Shin, S. Park, Y. Huang, and X. Duan, "Promises and prospects of two-dimensional transistors," *Nature*, vol. 591, no. 7848, pp. 43–53, 2021.

[16] Y.-Y. Chung, B.-J. Chou, C.-F. Hsu, W.-S. Yun, M.-Y. Li, S.-K. Su, Y.-T. Liao, M.-C. Lee, G.-W. Huang, S.-L. Liew, Y.-Y. Shen, W.-H. Chang, C.-W. Chen, C.-C. Kei, H. Wang, H.-S. P. Wong, T. Y. Lee, C.-H. Chien, C.-C. Cheng, and I. P. Radu, "First Demonstration of GAA Monolayer-$MoS_2$ Nanosheet nFET with 410 $\mu$A/$\mu$m $I_D$ at 1V $V_D$ at 40 nm gate length," in *2022 IEEE International Electron Devices Meeting (IEDM)*, pp. 823–826, 2022.

[17] Y.-H. Lee, X.-Q. Zhang, W. Zhang, M.-T. Chang, C.-T. Lin, K.-D. Chang, Y.-C. Yu, J. T.-W. Wang, C.-S. Chang, L.-J. Li, *et al.*, "Synthesis of large-area $MoS_2$ atomic layers with chemical vapor deposition," *Advanced materials*, vol. 24, no. 17, pp. 2320–2325, 2012.

[18] K. Novoselov and A. C. Neto, "Two-dimensional crystals-based heterostructures: materials with tailored properties," *Physica Scripta*, vol. 2012, no. T146, p. 014006, 2012.

[19] T. Ohashi, K. Suda, S. Ishihara, N. Sawamoto, S. Yamaguchi, K. Matsuura, K. Kakushima, N. Sugii, A. Nishiyama, Y. Kataoka, *et al.*, "Multi-layered $MoS_2$ film formed by high-temperature sputtering for enhancement-mode nMOSFETs," *Japanese Journal of Applied Physics*, vol. 54, no. 4S, p. 04DN08, 2015.

[20] K. Matsuura, T. Ohashi, I. Muneta, S. Ishihara, K. Kakushima, K. Tsutsui, A. Ogura, and H. Wakabayashi, "Low-carrier-density sputtered $MoS_2$ film by vapor-phase sulfurization," *Journal of Electronic Materials*, vol. 47, no. 7, pp. 3497–3501, 2018.

[21] K. Matsuura, M. Hamada, T. Hamada, H. Tanigawa, T. Sakamoto, A. Hori, I. Muneta, T. Kawanago, K. Kakushima, K. Tsutsui, *et al.*, "Normally-off sputtered-$MoS_2$ nMISFETs with TiN top-gate electrode all defined by optical lithography for chip-level integration," *Japanese Journal of Applied Physics*, vol. 59, no. 8, p. 080906, 2020.

[22] M. I. Alam, R. Sumichika, J. Tsuchimoto, T. Komeda, and A. Teramoto, "Interface analysis of oxide free $MoS_2$ films fabricated by solution process," *Scientific Reports*, vol. 14, no. 1, p. 26779, 2024.

[23] J. Zhu, J.-H. Park, S. A. Vitale, W. Ge, G. S. Jung, J. Wang, M. Mohamed, T. Zhang, M. Ashok, M. Xue, *et al.*, "Low-thermal-budget synthesis of monolayer molybdenum disulfide for silicon back-end-of-line integration on a 200 mm platform," *Nature Nanotechnology*, vol. 18, no. 5, pp. 456–463, 2023.

[24] J. Jiang, K. Parto, W. Cao, and K. Banerjee, "Monolithic-3D integration with 2D materials: Toward ultimate vertically-scaled 3D-ICs," in *2018 IEEE SOI-3D-Subthreshold Microelectronics Technology Unified Conference (S3S)*, pp. 1–3, IEEE, 2018.

[25] W. Li, M. Du, C. Zhao, G. Xiong, W. Gan, L. Liu, T. Li, Y. Gao, F. Hou, J. Lin, D. Fan, H. Qiu, Z. Yu, J. Xu, Y. Shi, and X. Wang, "Scaling $MoS_2$ transistors to 1 nm node," in *2024 IEEE International Electron Devices Meeting (IEDM)*, vol. 24-7, pp. 1–4, IEEE, 2024.

[26] Y. Zhao, Y. Li, and F. Ma, "Performance Upper Limit of Sub-10 nm Monolayer $MoS_2$ Transistors with $MoS_2$–Mo Electrodes," *The Journal of Physical Chemistry C*, vol. 126, no. 29, pp. 12100–12112, 2022.

[27] *IRDS™ 2023: IRDS Chairman Editorial, More Moore.*

[28] A. Agrawal, W. Chakraborty, W. Li, H. Ryu, B. Markman, S. H. Hoon, R. K. Paul, C. Y. Huang, S. M. Choi, K. Rho, A. Shu, R. Iglesias, P. Wallace, S. Ghosh, K. L. Cheong, J. L. Hockel, R. Thorman, L. Baumgartel, L. Shoer, V. Mishra, S. Berrada, A. Ashita, C. Weber, B. Obradovic, A. A. Oni, Z. Brooks, N. Franco, J. Kavalieros, and G. Dewey, "Silicon RibbonFET CMOS at 6 nm Gate Length," in *2024 IEEE International Electron Devices Meeting (IEDM)*, pp. 2–2, IEEE, 2024.

[29] S. M. Gali, A. Pershin, A. Lherbier, J.-C. Charlier, and D. Beljonne, "Electronic and transport properties in defective $MoS_2$: impact of sulfur vacancies," *The Journal of Physical Chemistry C*, vol. 124, no. 28, pp. 15076–15084, 2020.

[30] W. Li, J. Li, J. Shen, Y. Xu, Z. Wang, X. Jia, Q. Pang, and H. Guo, "Crystal structure, Raman spectra, and microwave dielectric properties of high-Q $Li_2ZnTi_3O_8$ systems with $Nb_2O_5$ addition," *Ceramics International*, vol. 47, no. 6, pp. 8601–8609, 2021.

[31] Z. Kou, A. Hashemi, M. J. Puska, A. V. Krasheninnikov, and H.-P. Komsa, "Simulating raman spectra by combining first-principles and empirical potential approaches with application to defective $MoS_2$," *npj Computational Materials*, vol. 6, no. 1, p. 59, 2020.

[32] H. Adachi and K. Wasa, "Thin films and nanomaterials," *Handbook of Sputter Deposition Technology: Fundamentals and Applications for Functional Thin Films, Nano-Materials and MEMS:*, pp. 3–39, 2012.

[33] M. Donarelli, F. Bisti, F. Perrozzi, and L. Ottaviano, "Tunable sulfur desorption in exfoliated $MoS_2$ by means of thermal annealing in ultra-high vacuum," *Chemical Physics Letters*, vol. 588, pp. 198–202, 2013.

[34] S. Zhu and Q. Wang, "A simple method for understanding the triangular growth patterns of transition metal dichalcogenide sheets," *AIP Advances*, vol. 5, no. 10, 2015.

[35] X. Luo, Y. Zhao, J. Zhang, Q. Xiong, and S. Y. Quek, "Anomalous frequency trends in $MoS_2$ thin films attributed to surface effects," *Physical Review B—Condensed Matter and Materials Physics*, vol. 88, no. 7, p. 075320, 2013.

[36] D. Wang, H. Li, N. Du, and W. Hou, "Amorphous molybdenum sulfide monolayer nanosheets for highly efficient electrocatalytic hydrogen evolution," *Chemical Engineering Journal*, vol. 398, p. 125685, 2020.

[37] L. R. L. Ting, Y. Deng, L. Ma, Y.-J. Zhang, A. A. Peterson, and B. S. Yeo, "Catalytic activities of sulfur atoms in amorphous molybdenum sulfide for the electrochemical hydrogen evolution reaction," *Acs Catalysis*, vol. 6, no. 2, pp. 861–867, 2016.

[38] Y. Shang, X. Xu, B. Gao, and Z. Ren, "Thiomolybdate [$Mo_3S_13$] 2–nanoclusters anchored on reduced graphene oxide-carbon nanotube aerogels for efficient electrocatalytic hydrogen evolution," *ACS Sustainable Chemistry and Engineering*, vol. 5, no. 10, pp. 8908–8917, 2017.

[39] S. Imai, T. Tatsumi, S. Tomiya, K. Kakushima, and H. Wakabayashi, "High Crystallinity of $MoS_2$ by Film Annealing in Sulfur Atmosphere and Plasma Control dur-

ing RF Sputtering," in *Electrochemical Society Meeting Abstracts prime2024*, no. 20, pp. 1791–1791, The Electrochemical Society, Inc., 2024.

[40] T. Hussain, J. L. Llácer, B. T. Wimberly, J. S. Kieft, and V. Ramakrishnan, "Large-scale movements of IF3 and tRNA during bacterial translation initiation," *Cell*, vol. 167, no. 1, pp. 133–144, 2016.

[41] S. Imai, T. Hamada, M. Hamada, T. Shirokura, I. Muneta, K. Kakushima, T. Tatsumi, S. Tomiya, K. Tsutsui, and H. Wakabayashi, "Importance of crystallinity improvement in $MoS_2$ film by compound sputtering even followed by post sulfurization," *Japanese Journal of Applied Physics*, vol. 60, no. SB, p. SBBH10, 2021.

[42] W. M. Parkin, A. Balan, L. Liang, P. M. Das, M. Lamparski, C. H. Naylor, J. A. Rodríguez-Manzo, A. C. Johnson, V. Meunier, and M. Drndic, "Raman shifts in electron-irradiated monolayer $MoS_2$," *ACS nano*, vol. 10, no. 4, pp. 4134–4142, 2016.

[43] N. Pliatsikas, O. Karabinaki, M. Zarshenas, G. Almyras, I. Shtepliuk, R. Yakimova, J. Arvanitidis, D. Christofilos, and K. Sarakinos, "Energetic bombardment and defect generation during magnetron-sputter-deposition of metal layers on graphene," *Applied Surface Science*, vol. 566, p. 150661, 2021.

[44] T. Lin, B. Kang, M. Jeon, C. Huffman, J. Jeon, S. Lee, W. Han, J. Lee, S. Lee, G. Yeom, *et al.*, "Controlled layer-by-layer etching of $MoS_2$," *ACS applied materials and interfaces*, vol. 7, no. 29, pp. 15892–15897, 2015.

[45] B. Ryu, Y. Liu, H. Pu, Y. Wang, X. Shi, S. S. Lee, and J. Chen, "A facile approach for site-selective and large-area growth of $MoS_2$ through heterogeneous nucleation," *Applied Surface Science*, vol. 607, p. 155066, 2023.

[46] G. Zhu, X. Zhang, H. Fang, D. Sun, L. Wang, Z. Dai, L. Wei, Q. Lin, A. Li, Y. Min, *et al.*, "Single-Crystalline Monolayer $MoS_2$ Arrays Based High-Performance Transistors via Selective-Area CVD Growth Directly on Silicon Wafers," in *2024 IEEE Symposium on VLSI Technology and Circuits (VLSI Technology and Circuits)*, pp. 1–2, IEEE, 2024.

[47] E. Kusano and S. Jinbo, "Suppression of $F^-$ ion incidence to growing film surface by using a double-grid retarding electrode in sputter deposition of $MgF_2$ thin films," in *15th International Conference on Plasma Surface Engineering*, vol. 4, 2016.

[48] H. Wakabayashi, T. Ezaki, T. Sakamoto, H. Kawaura, N. Ikarashi, N. Ikezawa, M. Narihiro, Y. Ochiai, T. Ikezawa, K. Takeuchi, *et al.*, "Characteristics and Modeling of Sub-10-nm Planar Bulk CMOS Devices Fabricated by Lateral Source/Drain Junction Control," *IEEE transactions on electron devices*, vol. 53, no. 9, pp. 1961–1970, 2006.

[49] G. Yeap, S. Lin, Y. Chen, H. Shang, P. Wang, H. Lin, Y. Peng, J. Sheu, M. Wang, X. Chen, *et al.*, "5nm CMOS production technology platform featuring full-fledged euv, and high mobility channel finfets with densest 0.021 $\mu$m$^2$ sram cells for mobile soc and high performance computing applications," in *2019 IEEE International Electron Devices Meeting (IEDM)*, pp. 36–7, IEEE, 2019.

[50] M. T. Bohr and I. A. Young, "CMOS scaling trends and beyond," *IEEE Micro*, vol. 37, no. 6, pp. 20–29, 2017.

[51] G. E. Moore *et al.*, "Cramming more components onto integrated circuits," 1965.

[52] J. Kilby, "US Patent No. 3, 138, 743," 1959.

[53] J. Bardeen and W. H. Brattain, "The transistor, a semi-conductor triode," *Physical Review*, vol. 74, no. 2, p. 230, 1948.

[54] S. Samavedam, J. Ryckaert, E. Beyne, K. Ronse, N. Horiguchi, Z. Tokei, I. Radu, M. Bardon, M. Na, A. Spessot, *et al.*, "Future logic scaling: Towards atomic channels and deconstructed chips," in *2020 IEEE International Electron Devices Meeting (IEDM)*, pp. 1–1, IEEE, 2020.

[55] C.-J. Park, H. J. Park, J. Y. Kim, S.-H. Lee, Y. Lee, J. Kim, and J. Joo, "Photo-responsive $MoS_2$/organic-rubrene heterojunction field-effect-transistor: Application to photo-triggered ternary inverter," *Semiconductor Science and Technology*, vol. 35, no. 6, p. 065020, 2020.

[56] M. I. Alam, T. Takaoka, H. Waizumi, Y. Tanaka, M. S. Al Mamun, A. Ando, and T. Komeda, "Sensor behavior of $MoS_2$ field-effect transistor with light injection toward chemical recognition," *RSC advances*, vol. 11, no. 43, pp. 26509–26515, 2021.

[57] X. Wang, S. Yang, Q. Yue, F. Wu, and J. Li, "Response of $MoS_2$ nanosheet field effect transistor under different gas environments and its long wavelength photoresponse characteristics," *Journal of alloys and compounds*, vol. 615, pp. 989–993, 2014.

[58] P.-C. Shen, C. Su, Y. Lin, A.-S. Chou, C.-C. Cheng, J.-H. Park, M.-H. Chiu, A.-Y. Lu, H.-L. Tang, M. M. Tavakoli, *et al.*, "Ultralow contact resistance between semimetal and monolayer semiconductors," *Nature*, vol. 593, no. 7858, pp. 211–217, 2021.

[59] Y. Shen, Z. Dong, Y. Sun, H. Guo, F. Wu, X. Li, J. Tang, J. Liu, X. Wu, H. Tian, *et al.*, "The Trend of 2D Transistors toward Integrated Circuits: Scaling Down and New Mechanisms (Adv. Mater. 48/2022)," *Advanced Materials*, vol. 34, no. 48, p. 2270329, 2022.

[60] X. Duan, C. Wang, A. Pan, R. Yu, and X. Duan, "Two-dimensional transition metal dichalcogenides as atomically thin semiconductors: opportunities and challenges," *Chemical Society Reviews*, vol. 44, no. 24, pp. 8859–8876, 2015.

[61] R. Sundaram, M. Engel, A. Lombardo, R. Krupke, A. Ferrari, P. Avouris, and M. Steiner, "Electroluminescence in single layer $MoS_2$," *Nano letters*, vol. 13, no. 4, pp. 1416–1421, 2013.

[62] A. Kuc, N. Zibouche, and T. Heine, "Influence of quantum confinement on the electronic structure of the transition metal sulfide $TS_2$," *Physical Review B*, vol. 83, no. 24, p. 245213, 2011.

[63] H. Wang, L. Yu, Y.-H. Lee, W. Fang, A. Hsu, P. Herring, M. Chin, M. Dubey, L.-J. Li, J. Kong, *et al.*, "Large-scale 2D electronics based on single-layer $MoS_2$ grown by chemical vapor deposition," in *2012 International Electron Devices Meeting*, pp. 4–6, IEEE, 2012.

[64] K. Dolui, I. Rungger, C. D. Pemmaraju, and S. Sanvito, "Possible doping strategies for $MoS_2$ monolayers: An ab initio study," *Physical Review B*, vol. 88, no. 7, p. 075420, 2013.

[65] K.-K. Liu, W. Zhang, Y.-H. Lee, Y.-C. Lin, M.-T. Chang, C.-Y. Su, C.-S. Chang, H. Li, Y. Shi, H. Zhang, *et al.*, "Growth of large-area and highly crystalline $MoS_2$ thin layers on insulating substrates," *Nano letters*, vol. 12, no. 3, pp. 1538–1544, 2012.

[66] S. Hirano, J. Shimizu, K. Matsuura, T. Ohashi, I. Muneta, K. Kakushima, K. Tsutsui, and H. Wakabayashi, "Crystallinity improvement using migration-enhancement methods for sputtered-$MoS_2$ films," in *2017 IEEE Electron Devices Technology and Manufacturing Conference (EDTM)*, pp. 234–235, IEEE, 2017.

[67] T. Sakamoto, T. Ohashi, K. Matsuura, I. Muneta, K. Kakushima, K. Tsutsui, Y. Suzuki, N. Ikarashi, and H. Wakabayashi, "Mechanism for High Hall-Effect Mobility in Sputtered-$MoS_2$ Film Controlling Particle Energy," in *2018 IEEE SOI-3D-Subthreshold Microelectronics Technology Unified Conference (S3S)*, pp. 1–2, IEEE, 2018.

[68] S. Das, H.-Y. Chen, A. V. Penumatcha, and J. Appenzeller, "High performance multilayer $MoS_2$ transistors with scandium contacts," *Nano letters*, vol. 13, no. 1, pp. 100–105, 2013.

[69] W. Bao, X. Cai, D. Kim, K. Sridhara, and M. S. Fuhrer, "High mobility ambipolar $MoS_2$ field-effect transistors: Substrate and dielectric effects," *Applied Physics Letters*, vol. 102, no. 4, 2013.

[70] W. Wu, D. De, S.-C. Chang, Y. Wang, H. Peng, J. Bao, and S.-S. Pei, “High mobility and high on/off ratio field-effect transistors based on chemical vapor deposited single-crystal $MoS_2$ grains,” *Applied Physics Letters*, vol. 102, no. 14, 2013.

[71] S. Zhang, J. Zhang, Q. Zhang, C. Barton, V. Neu, Y. Zhao, Z. Hou, Y. Wen, C. Gong, O. Kazakova, *et al.*, “Direct writing of room temperature and zero field skyrmion lattices by a scanning local magnetic field,” *Applied Physics Letters*, vol. 112, no. 13, 2018.

[72] W. Li, M. Du, C. Zhao, G. Xiong, W. Gan, L. Liu, T. Li, Y. Gao, F. Hou, J. Lin, D. Fan, H. Qiu, Z. Yu, J. Xu, Y. Shi, and X. Wang *Nature Nanotechnology*, vol. 19, no. 7, pp. 895–906, 2024.

[73] L. Deng, L. Zhou, H. Lu, L. Yang, Q. Yu, M. Zhang, M. Wu, B. Hou, X. Ma, and Y. Hao, “Comprehensive Comparison of MOCVD-and LPCVD-SiNx Surface Passivation for AlGaN/GaN HEMTs for 5G RF Applications,” *Micromachines*, vol. 14, no. 11, p. 2104, 2023.

[74] S. Katsuda and Y. Kawanishi, “Stability on sin thin films prepared by reactive sputtering,” *Journal of the Ceramic Society of Japan*, vol. 100, no. 1158, pp. 134–137, 1992.

[75] M. Badaroglu, “Outlook of device and assembly technologies enabling high-performance mobile computing: IRDS view,” in *Proceedings of the Workshop on System-Level Interconnect: Problems and Pathfinding Workshop*, pp. 1–7, 2020.

[76] H. Casey, “Jr., mb panish, heterostructure lasers,” 1978.

[77] M. Giesen, “Step and island dynamics at solid/vacuum and solid/liquid interfaces,” *Progress in Surface Science*, vol. 68, no. 1-3, pp. 1–154, 2001.

[78] R. Yue, Y. Nie, L. A. Walsh, R. Addou, C. Liang, N. Lu, A. T. Barton, H. Zhu, Z. Che, D. Barrera, *et al.*, “Nucleation and growth of $WSe_2$: enabling large grain transition metal dichalcogenides,” *2D Materials*, vol. 4, no. 4, p. 045019, 2017.

[79] Z. Zhang, P. Chen, X. Yang, Y. Liu, H. Ma, J. Li, B. Zhao, J. Luo, X. Duan, and X. Duan, “Ultrafast growth of large single crystals of monolayer $WS_2$ and $WSe_2$,” *National Science Review*, vol. 7, no. 4, pp. 737–744, 2020.

[80] L. Wu, W. Yang, and G. Wang, “Mechanism of substrate-induced anisotropic growth of monolayer $WS_2$ by kinetic Monte Carlo simulations,” *npj 2D Materials and Applications*, vol. 3, no. 1, p. 6, 2019.

[81] M. W. Thompson, “II. The energy spectrum of ejected atoms during the high energy sputtering of gold,” *Philosophical Magazine*, vol. 18, no. 152, pp. 377–414, 1968.

[82] Y. Kudriavtsev, A. Villegas, A. Godines, and R. Asomoza, "Calculation of the surface binding energy for ion sputtered particles," *Applied surface science*, vol. 239, no. 3-4, pp. 273–278, 2005.

[83] A. Gras-Marti and J. Valles-Abarca, "Slowing down and thermalization of sputtered particle fluxes: Energy distributions," *Journal of applied physics*, vol. 54, no. 2, pp. 1071–1075, 1983.

[84] K. Meyer, I. K. Schuller, and C. M. Falco, "Thermalization of sputtered atoms," *Journal of Applied Physics*, vol. 52, no. 9, pp. 5803–5805, 1981.

[85] J. F. Ziegler, "SRIM-2003," *Nuclear instruments and methods in physics research section B: Beam interactions with materials and atoms*, vol. 219, pp. 1027–1036, 2004.

[86] J. F. Ziegler and J. P. Biersack, "SRIM-2008, stopping power and range of ions in matter," 2008.

[87] W. J. Weber and Y. Zhang, "Predicting damage production in monoatomic and multi-elemental targets using stopping and range of ions in matter code: Challenges and recommendations," *Current Opinion in Solid State and Materials Science*, vol. 23, no. 4, p. 100757, 2019.

[88] S. Damache, D. Moussa, and S. Ouichaoui, "Stopping of {approx} 0.2-3.4 mev/amu {sup 1} h {sup+} and {sup 4} he {sup+} ions in polyvinyl formal," *Nuclear Instruments and Methods in Physics Research. Section B, Beam Interactions with Materials and Atoms*, vol. 268, 2010.

[89] M. QH and M. HA, "Alpha-particle stopping powers in air and argon," *Res Rev J Pure Appl Phys*, vol. 5, no. 4, pp. 22–8, 2017.

[90] R. Bimbot, C. Cabot, D. Gardes, H. Gauvin, R. Hingmann, I. Orliange, L. De Reilhac, and F. Hubert, "Stopping power of gases for heavy ions: Gas-solid effect: I. 2–13 mev/u ne and ar projectiles," *Nuclear Instruments and Methods in Physics Research Section B: Beam Interactions with Materials and Atoms*, vol. 44, no. 1, pp. 1–18, 1989.

[91] "The Stopping and Range of Ions in Matter." `http://www.srim.org/PlotCit.htm`.

[92] S. Mahieu, K. Van Aeken, D. Depla, D. Smeets, and A. Vantomme, "Dependence of the sticking coefficient of sputtered atoms on the target–substrate distance," *Journal of Physics D: Applied Physics*, vol. 41, no. 15, p. 152005, 2008.

[93] C. Li and J.-H. Hsieh, "Effects of variable sticking coefficients on the stability of reactive sputtering process," *Journal of Physics D: Applied Physics*, vol. 37, no. 7, p. 1065, 2004.

[94] X. Zhou and H. Wadley, "Hyperthermal vapor deposition of copper: reflection and resputtering effects," *Surface science*, vol. 431, no. 1-3, pp. 58–73, 1999.

[95] P. Redhead, "Thermal desorption of gases," *vacuum*, vol. 12, no. 4, pp. 203–211, 1962.

[96] T. Yamamoto, H. Miura, and O. M. Shalabiea, "Thermal desorption induced by chemical reaction on dust surface," *Monthly Notices of the Royal Astronomical Society*, vol. 490, no. 1, pp. 709–717, 2019.

[97] NIST Chemistry WebBook, "NIST Chemistry WebBook, SRD 69." `https://webbook.nist.gov/`, 2025. Accessed: 2025-02-19.

[98] Z. G. Yu, Y.-W. Zhang, and B. I. Yakobson, "An anomalous formation pathway for dislocation-sulfur vacancy complexes in polycrystalline monolayer $MoS_2$," *Nano letters*, vol. 15.

[99] S. Baik, Y. Koo, and W. Choi, "Decreased n-type behavior of monolayer $MoS_2$ crystals annealed in sulfur atmosphere," *Current Applied Physics*, vol. 42, pp. 38–42, 2022.

[100] M. Li, J. Yao, X. Wu, S. Zhang, B. Xing, X. Niu, X. Yan, Y. Yu, Y. Liu, and Y. Wang, "P-type doping in large-area monolayer $MoS_2$ by chemical vapor deposition," *ACS applied materials and interfaces*, vol. 12, no. 5, pp. 6276–6282, 2020.

[101] S. Zhang, H. M. Hill, K. Moudgil, C. A. Richter, A. R. Hight Walker, S. Barlow, S. R. Marder, C. A. Hacker, and S. J. Pookpanratana, "Controllable, wide-ranging n-doping and p-doping of monolayer group 6 transition-metal disulfides and diselenides," *Advanced Materials*, vol. 30, no. 36, p. 1802991, 2018.

[102] D. Viladot, M. Véron, M. Gemmi, F. Peiró, J. Portillo, S. Estradé, J. Mendoza, N. LLORCA-ISERN, and S. Nicolopoulos, "Orientation and phase mapping in the transmission electron microscope using precession-assisted diffraction spot recognition: state-of-the-art results," *Journal of microscopy*, vol. 252, no. 1, pp. 23–34, 2013.

[103] J.-J. Fundenberger, A. Morawiec, E. Bouzy, and J.-S. Lecomte, "Polycrystal orientation maps from TEM," *Ultramicroscopy*, vol. 96, no. 2, pp. 127–137, 2003.

[104] J. Jeon, S. K. Jang, S. M. Jeon, G. Yoo, Y. H. Jang, J.-H. Park, and S. Lee, "Layer-controlled CVD growth of large-area two-dimensional $MoS_2$ films," *Nanoscale*, vol. 7, no. 5, pp. 1688–1695, 2015.

[105] D.-H. Cho, W.-J. Lee, J.-H. Wi, W. S. Han, S. J. Yun, B. Shin, and Y.-D. Chung, "Enhanced sulfurization reaction of molybdenum using a thermal cracker for forming

two-dimensional $MoS_2$ layers," *Physical Chemistry Chemical Physics*, vol. 20, no. 23, pp. 16193–16201, 2018.

[106] R. Kaindl, B. C. Bayer, R. Resel, T. Müller, V. Skakalova, G. Habler, R. Abart, A. S. Cherevan, D. Eder, M. Blatter, *et al.*, "Growth, structure and stability of sputter-deposited $MoS_2$ thin films," *Beilstein journal of nanotechnology*, vol. 8, no. 1, pp. 1115–1126, 2017.

[107] D. Gahan, B. Dolinaj, and M. Hopkins, "Retarding field analyzer for ion energy distribution measurements at a radio-frequency biased electrode," *Review of Scientific Instruments*, vol. 79, no. 3, 2008.

[108] Y. Yuan, J. Bansky, J. Engemann, and A. Brockhaus, "Ion energy determination for rf plasma and ion beam using a multigrid retarding field analyser," *Surface and Coatings Technology*, vol. 74, pp. 534–538, 1995.

[109] D. Marinov, Z. El Otell, M. Bowden, and N. S. J. Braithwaite, "Extraction and neutralization of positive and negative ions from a pulsed electronegative inductively coupled plasma," *Plasma Sources Science and Technology*, vol. 24, no. 6, p. 065008, 2015.

[110] C. Corbella, M. Rubio-Roy, E. Bertran, S. Portal, E. Pascual, M. Polo, and J. Andújar, "Ion energy distributions in bipolar pulsed-dc discharges of methane measured at the biased cathode," *Plasma Sources Science and Technology*, vol. 20, no. 1, p. 015006, 2011.

[111] Y. Matsuda, K. Watanabe, S. Uzunoe, and T. Furusato, "Energy distribution function of substrate incident negative ions in magnetron sputtering of metal-doped ZnO target measured by magnetized retarding field energy analyzer," *Japanese Journal of Applied Physics*, vol. 62, no. SL, p. SL1021, 2023.

[112] L. Yang, X. Cui, J. Zhang, K. Wang, M. Shen, S. Zeng, S. A. Dayeh, L. Feng, and B. Xiang, "Lattice strain effects on the optical properties of $MoS_2$ nanosheets," *Scientific reports*, vol. 4, no. 1, p. 5649, 2014.

[113] S. Wang, Z. Wang, J. Qin, W. Wang, W. Li, and D. He, "Nanocrystalline $MoS_2$ through directional growth along the (0 0 2) crystal plane under high pressure," *Materials Chemistry and Physics*, vol. 130, no. 1-2, pp. 170–174, 2011.

[114] D. Rafalskyi, L. Popelier, and A. Aanesland, "Experimental validation of the dual positive and negative ion beam acceleration in the plasma propulsion with electronegative gases thruster," *Journal of Applied Physics*, vol. 115, no. 5, 2014.

[115] M. Moravej, X. Yang, G. Nowling, J. Chang, R. Hicks, and S. Babayan, "Physics of high-pressure helium and argon radio-frequency plasmas," *Journal of applied physics*, vol. 96, no. 12, pp. 7011–7017, 2004.

[116] J. Held, P. Maaß, V. Schulz-Von Der Gathen, and A. von Keudell, "Electron density, temperature and the potential structure of spokes in HiPIMS," *Plasma Sources Science and Technology*, vol. 29, no. 2, p. 025006, 2020.

[117] C. Guo, Y. Li, C. Qi, H. Sun, D. Zhang, and Y. Wan, "Effect of solvent acids on the microstructure and corrosion resistance of chitosan films on MAO-treated AZ31B magnesium alloy," *International Journal of Biological Macromolecules*, vol. 277, p. 134349, 2024.

[118] N. Mahne, M. Čekada, and M. Panjan, "Energy Distribution of Sputtered Atoms Explored by SRIM Simulations," *Coatings*, vol. 13, no. 8, p. 1448, 2023.

[119] A. Naumovets and Y. S. Vedula, "Surface diffusion of adsorbates," *Surface Science Reports*, vol. 4, no. 7-8, pp. 365–434, 1985.

[120] J. A. Thornton, "Influence of substrate temperature and deposition rate on structure of thick sputtered Cu coatings," *Journal of Vacuum Science and Technology*, vol. 12, no. 4, pp. 830–835, 1975.

[121] K. K. Smithe, S. V. Suryavanshi, M. Muñoz Rojo, A. D. Tedjarati, and E. Pop, "Low variability in synthetic monolayer $MoS_2$ devices," *ACS nano*, vol. 11, no. 8, pp. 8456–8463, 2017.

[122] P. Yan, J. Wang, G. Yang, N. Lu, G. Chu, X. Zhang, and X. Shen, "Chemical vapor deposition of monolayer $MoS_2$ on sapphire, si and gan substrates," *Superlattices and Microstructures*, vol. 120, pp. 235–240, 2018.

[123] S. Imai, R. Ono, I. Muneta, K. Kakushima, and T. Tatsumi, "Grain-Size Enlargement of $MoS_2$ Film by Low-Rate Sputtering with Molybdenum Grid," in *2023 7th IEEE Electron Devices Technology and Manufacturing Conference (EDTM)*, pp. 1–3, IEEE, 2023.

[124] S. Qian, R. Yang, F. Lan, Y. Xu, K. Sun, S. Zhang, Y. Zhang, and Z. Dong, "Growth of continuous $MoS_2$ film with large grain size by chemical vapor deposition," *Materials Science in Semiconductor Processing*, vol. 93, pp. 317–323, 2019.

[125] D. Rauch, "Automated NLO calculations with Massive Quarks in Herwig++," *Master's thesis, KIT*, 2014.

[126] L. Latu-Romain, Y. Parsa, S. Mathieu, M. Vilasi, A. Galerie, and Y. Wouters, "Towards the growth of stoichiometric chromia on pure chromium by the control of temperature and oxygen partial pressure," *Corrosion Science*, vol. 126, pp. 238–246, 2017.

[127] H. Ogawa, *Study on the properties of tin oxide ultrafine particle films and their application to gas sensors, in Japanese*. PhD thesis, Osaka University, 1982.

[128] M. Vopsaroiu, G. V. Fernandez, M. Thwaites, J. Anguita, P. Grundy, and K. O'grady, "Deposition of polycrystalline thin films with controlled grain size," *Journal of Physics D: Applied Physics*, vol. 38, no. 3, p. 490, 2005.

[129] F. Ruffino, M. Grimaldi, C. Bongiorno, F. Giannazzo, F. Roccaforte, V. Raineri, and C. Spinella, "Normal and abnormal grain growth in nanostructured gold film," *Journal of Applied Physics*, vol. 105, no. 5, 2009.

[130] S. Bertolazzi, S. Bonacchi, G. Nan, A. Pershin, D. Beljonne, and P. Samorì, "Engineering chemically active defects in monolayer $MoS_2$ transistors via ion-beam irradiation and their healing via vapor deposition of alkanethiols," *Advanced materials*, vol. 29, no. 18, p. 1606760, 2017.

[131] A. Koma, "Van der waals epitaxy—a new epitaxial growth method for a highly lattice-mismatched system," *Thin Solid Films*, vol. 216, no. 1, pp. 72–76, 1992.

[132] K. S. Kim, D. Lee, C. S. Chang, S. Seo, Y. Hu, S. Cha, H. Kim, J. Shin, J.-H. Lee, S. Lee, *et al.*, "Non-epitaxial single-crystal 2D material growth by geometric confinement," *Nature*, vol. 614, no. 7946, pp. 88–94, 2023.

[133] M. S. Yoo, A. Jung, S. Yang, J. E. Yoo, E.-K. Lee, K.-E. Byun, J. Baik, D.-J. Yun, J. Park, J. Kim, and M. Seol, "Direct growth and manufacturing of single-crystalline 2D FETs on 8-inch Si wafers," in *2024 IEEE International Electron Devices Meeting (IEDM)*, vol. 24-1, pp. 1–4, IEEE, 2024.

[134] D. Lin, X. Wu, D. Cott, D. Verreck, B. Groven, S. Sergeant, Q. Smets, S. Sutar, I. Asselberghs, and I. Radu, "Dual gate synthetic $WS_2$ MOSFETs with 120 $\mu$S/$\mu$m Gm 2.7 $\mu F/cm^2$ capacitance and ambipolar channel," in *2020 IEEE International Electron Devices Meeting (IEDM)*, pp. 3–6, IEEE, 2020.

[135] X. Xiong, A. Tong, X. Wang, S. Liu, X. Li, R. Huang, and Y. Wu, "Demonstration of Vertically-stacked CVD Monolayer Channels: $MoS_2$ Nanosheets GAA-FET with $I_{on} > 700$ $\mu$A/$\mu$m and $MoS_2/WSe_2$ CFET," in *2021 IEEE International Electron Devices Meeting (IEDM)*, pp. 7–5, IEEE, 2021.

[136] Q. Smets, D. Verreck, Y. Shi, G. Arutchelvan, B. Groven, X. Wu, S. Sutar, S. Banerjee, A. N. Mehta, D. Lin, *et al.*, "Sources of variability in scaled $MoS_2$ FETs," in *2020 IEEE International Electron Devices Meeting (IEDM)*, pp. 3–1, IEEE, 2020.

[137] Z. Zhang, X. Xu, J. Song, Q. Gao, S. Li, Q. Hu, X. Li, and Y. Wu, "High-performance transistors based on monolayer cvd $MoS_2$ grown on molten glass," *Applied Physics Letters*, vol. 113, no. 20, 2018.

# Appendix A

# Benchmark of $MoS_2$ film properties in recent researches

Currently, the highest mobility achieved using a single crystal (SC) $MoS_2$ channel is 62 $cm^2/Vs$, as shown in Table A.1.

**Table A.1**: Benchmark of large-area $MoS_2$ films. SC: Single crystal, PC: Polycrystal.

| **Research group** | **Place of issue** | **Formation method** | **Formation temperature** | **Mobility [$cm^2/Vs$]** | **$I_{on}/I_{off}$ ratio** | Reference |
|---|---|---|---|---|---|---|
| Massachusetts Institute of Technology | Nature 2023 | CVD SC-$MoS_2$ on $HfO_2$ | 750°C | 62.2 | $> 10^8$ | [132] |
| Science and Technology of China and IMEC | VLSI Symposium 2024 | CVD SC-$MoS_2$ on $Al_2O_3$ | N/A | 62.8 | $2.5 \times 10^8$ | [46] |
| Samsung | IEDM 2024 | CVD SC-$MoS_2$ on $HfO_2$ | N/A | 34.4 | $10^4$ | [133] |
| IMEC | IEDM 2020 | CVD PC-$MoS_2$ transferred from sapphire | 1000°C | 20 | $> 10^8$ | [134] |
| Peking University | IEDM 2021 | CVD PC-$MoS_2$ transferred from sapphire | N/A | 25 | N/A | [135] |
| IMEC | IEDM 2020 | CVD SC-$MoS_2$ transferred from sapphire | N/A | 4–23 | N/A | [136] |
| University of Houston | Appl. Phys. Lett. 2013 | CVD SC-$MoS_2$ on $SiO_2$ | 1100°C | $\sim 17.3$ | $\sim 10^8$ | [70] |
| University of Houston | Appl. Phys. Lett. 2018 | CVD SC-$MoS_2$ transferred from glass | 850°C | 24 | $10^6$ | [137] |
| Institute of Science Tokyo | JJAP 2020 | Sputtering S-annealing PC-$MoS_2$ on $SiO_2$ | 400°C + 700°C | 0.21 | $\sim 10^2$ | [21] |

# Appendix B

# Control of $MoS_2$ film quality by accelerating the ionized particles to the substrate using molybdenum-grid electrodes

## B.1 Background

This section describes a previous study of $MgF_2$ sputtering using mesh electrodes. This is an example of research in which sputtering was performed by introducing two mesh electrodes that can apply voltage near the substrate in the sputtering system. The negative ions of F sputtered from the $MgF_2$ target are accelerated by the sheath, causing F defects in the deposited film [47]. By applying a retarding voltage to the mesh grids electrodes in the direction to decelerate the negative ions, the negative ions accelerated in the sheath are suppressed, which obtained films with few defects, as shown in Figures B.1 (a) and (b).

It is thought that the quality of $MoS_2$ film can be improved by introducing this mesh electrode to $MoS_2$ sputtering.

## B.2 Experimental methods

RF magnetron sputtering was also adopted in this study. By applying RF power, Ar plasma is generated, and the accelerated Ar ions collide with the target, sputtering the target particles. Figure B.2 shows RF magnetron sputtering using Mo-mesh electrodes. The two Mo-meshes were placed directly below the substrate. A variable voltage can be applied to the two meshes, and the current flowing into each mesh can be measured. In this study, the voltages of each mesh electrode are applied one minute after the plasma is generated. Three minutes later, the shutter is opened, and $MoS_2$ is deposited. The sputtering parameters were set at 40 W RF power, 300 °C substrate temperature, 0.55 Pa Ar pressure, 7 sccm Ar flow rate, and 150 mm target-substrate distance. $MoS_2$ is deposited

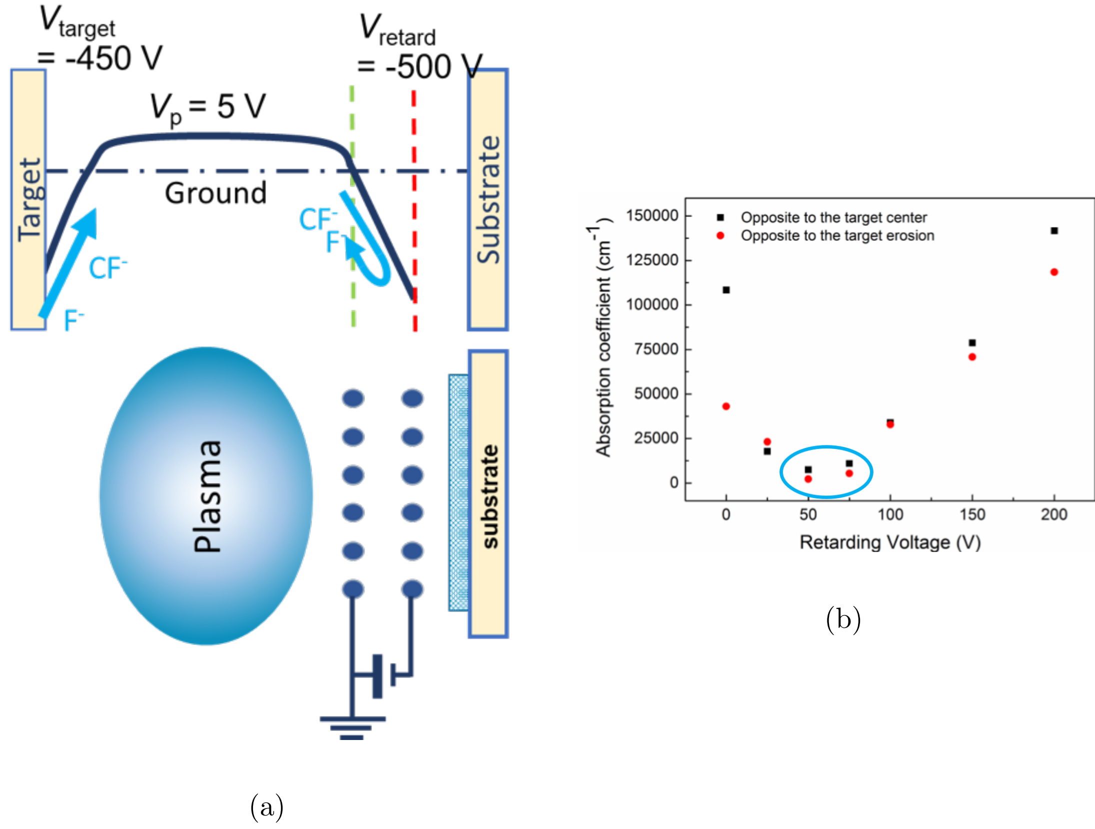


**Figure B.1**: (a) Mechanism of $MgF_2$ sputtering using Mesh electrodes and potential distribution during retarding voltage application. (b) Absorption coefficient from photoluminescence (PL) measurement varying mesh retarding voltage. In blue circles, absorption coefficient decreased, and $MgF_2$ film quality was improved [47].

under different sputtering conditions by varying the mesh voltages. The conditions of applying the mesh electrodes are detailed in Table B.1.

**Table B.1**: Conditions of applying the mesh electrodes.

| **1$^{st}$ mesh voltage [V]** | 0 | 0 | 0 |
|---|---|---|---|
| **2$^{nd}$ mesh voltage X [V]** | 0 | -20 | -40 |

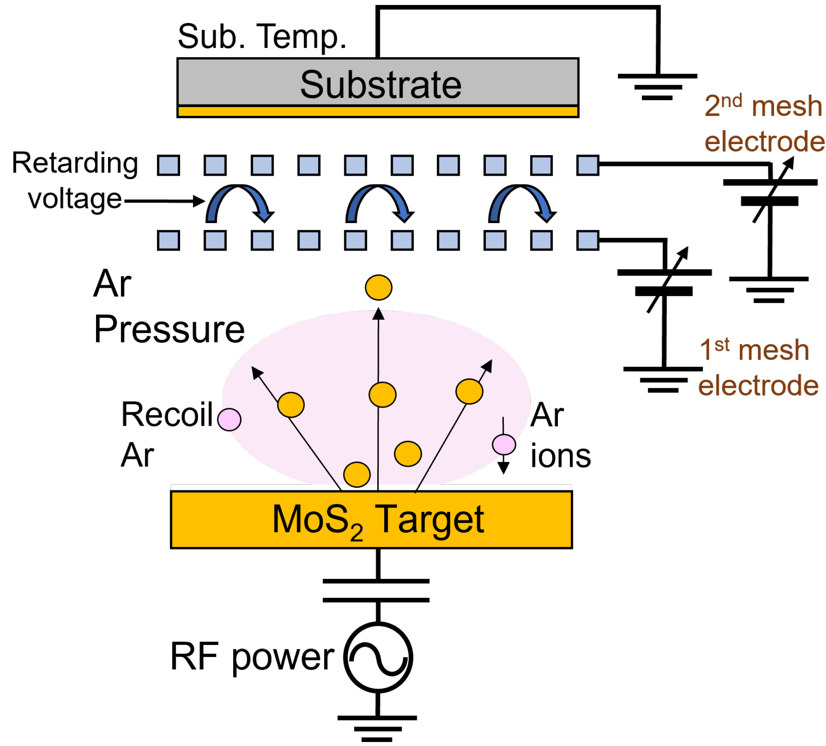


**Figure B.2**: RF magentron sputter using Mo-mesh electrodes.

## B.3 Results and discussion

Figure B.3 shows the peak shift values of $A_{1g}$-$E^1_{2g}$ at five points on $MoS_2$ films after sputtering by varying the $2^{nd}$ mesh electrode. The peak shift values decrease with the decrease in the $2^{nd}$ mesh voltage, which reduces the sulfur defect vacancies by applying the negative voltages. Figure B.4 shows the model potential distribution in sputtering apparatus applying a negative voltage to the $2^{nd}$ mesh electrode. $1^{st}$ mesh voltage was set to 0 V. In chapter 4, positive ions ($Ar^+$) are observed. Therefore, it is considered that when a negative voltage is applied to the $2^{nd}$ mesh, more Ar+ ions in the plasma flow into the substrate, which increases the flux temperature ($T_{\mathrm{flux}}$) and concentrates the particles in an increased surface diffusion length, improving the film quality. Further improvement in film quality is expected from applying greater mesh voltage.

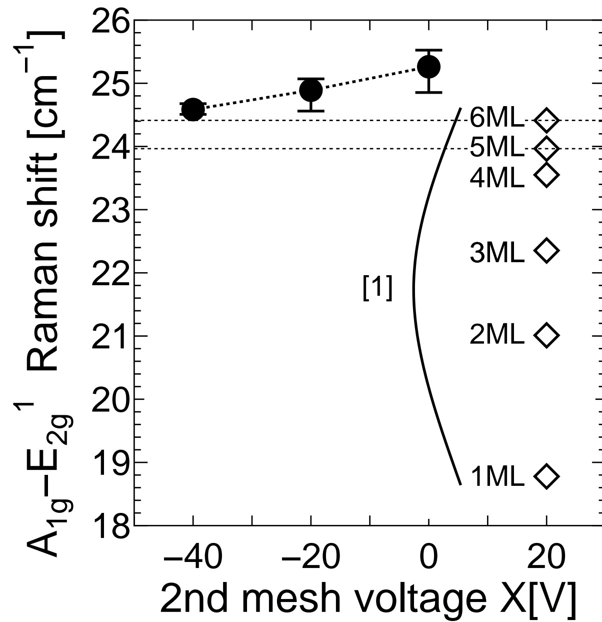


**Figure B.3**: Raman peak shift values of $MoS_2$ film deposited by sputtering applied with different $2^{nd}$ mesh electrode.

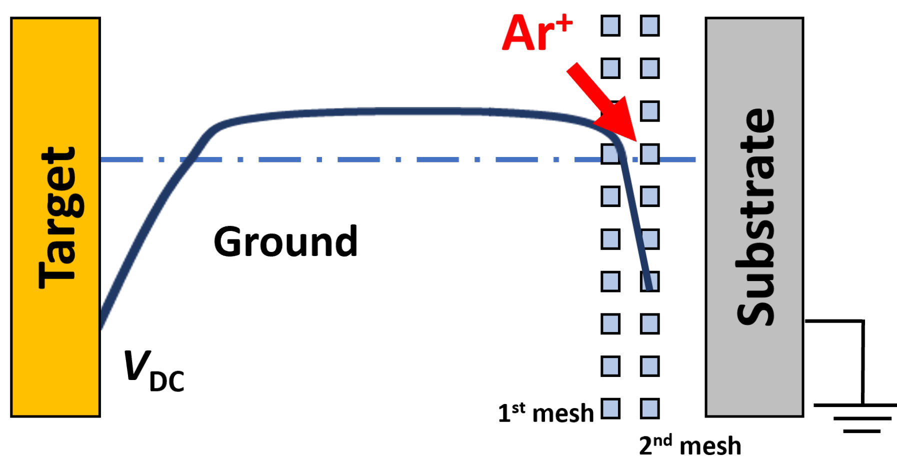


**Figure B.4**: Model of potential distribution in sputtering apparatus applying negative voltage to $2^{nd}$ mesh electrode. $1^{st}$ mesh voltage was set to 0 V.